Università degli Studi di Padova

Sede amministrativa: Università degli Studi di Padova

Dipartimento di Tecnica e Gestione dei Sistemi Industriali

Scuola di dottorato in ingegneria meccatronica e dell'innovazione del prodotto

Ciclo XXXIV

Towards more autonomous and intelligent industrial AC drives for Mechatronics

Direttore della scuola: Ch.ma Prof.ssa prof. Daria Battini

Relatore: Ch.mo Prof. prof. Mauro Zigliotto

Dottorando: Dario Pasqualotto

Dario Pasqualotto:
Towards more autonomous and intelligent industrial AC drives for Mechatronics

This work has been composed with LaTeX and the Ivan Valbusa's class suftesi. The font is the Linux Libertine serif by Libertine Open Fonts Project.

To my nearly wife, Sofia.

As she colours my days
like no one else can.

ABSTRACT

The modern industrial world calls for efficient, reliable and safe systems. A contribution to the solution to all these problems is the predictive maintenance.

According to this trend and tailoring the analysis to the electric drives field, this thesis performs a step forward for the realization of more reliable drives through their condition monitoring. Different AC motors have been considered in the dissertation: Permanent Magnet Synchronous Motors, Induction Motors and Synchronous Reluctance Motors, covering the actual and also the next future industrial drives scenario.

Some of the more relevant faults that can occur on these machines have been taken into account: interturn short circuits, demagnetization and damage at the rotor bars. The development of adequate observation indexes for the recognition of these failures has been researched deeply in the past. Nowadays, the prompt recognition of the incoming failure condition is the issue that modern research in this field has to face. In the following chapters, some innovative Artificial Intelligence-based tools will be applied for the condition monitoring of electric motors. Artificial Neural Networks and Convolutional Neural Networks are used here in different ways: for an effective modelling of the machine behaviour and for the knowledge-based recognition of the motor state of health.

The main bottleneck in developing Neural Networks is the availability of a proper training dataset for the efficient tuning of their weights. In case of electric motors, the problem is even more relevant. A huge amount of healthy and damaged motors are needed, an unaffordable condition for this industry-oriented context. As an innovative and never-used-before approach, very precise models of the motors have been used in the thesis to generate artificially the training dataset. When these models were not available, the Data Augmentation theory was used instead as a keen and innovative approach for the artificial enhancing of the available training datasets.

Very relevant results have been obtained and the principal and more significant ones are reported in this dissertation. Three different Convolutional Neural Network designs are reported. The first, trained only on a simulative accurate model of the motor, was able to efficiently recognize demagnetization and the interturn fault on Permanent Magnet Synchronous Motors. The second one, oriented to Induction Motors, the model was not available and so Data Augmentation was used to train the network that recognizes broken bars in the rotor. The third network was used again for Induction Motors but it made use of a model which definition was still based on a built-in Neural Network. Finally, this same Artificial Intelligence-based modelling methodology was used for the effective implementation of the Extended Kalman Filter for the sensorless control of Synchronous Reluctance Motors, thus

further enhancing the reliability of the drive, since the position sensor is avoided. The motor non linearities have been managed through a custom Artificial Neural Network and new approaches to the original Extended Kalman Filter implementations have been studied.

As common root of all the treated topics, Neural Networks applicability on the electric drives field has been investigated. In the development of these tools, a special and careful eye was taken to maintain the solution feasible and attractive from an industrial point of view. Therefore, each of the arguments was fully validated through an intensive simulation and experimental stages, as reported in the thesis.

PUBLICATIONS

[1] I.D. De Martin, D. Pasqualotto, F. Tinazzi, and M. Zigliotto. "Model-free Predictive Current Control of Synchronous Reluctance Motor Drives for Pump Applications". In: *MDPI Machines* (2021, in Press).

[2] L. Ortombina, D. Pasqualotto, F. Tinazzi, and M. Zigliotto. "Automatic Tuning Procedure at Standstill for Extended Kalman Filter in Sensorless Control of Permanent Magnet Synchronous Motors". In: *2019 IEEE 10th International Symposium on Sensorless Control for Electrical Drives (SLED)*. 2019, pp. 1–6. DOI: 10.1109/SLED.2019.8896350.

[3] L. Ortombina, D. Pasqualotto, F. Tinazzi, and M. Zigliotto. "Comprehensive Analysis and Design of a Pulsating Signal Injection-based Position Observer for Sensorless Synchronous Motor Drives". In: *IEEE Journal of Emerging and Selected Topics in Power Electronics* (2021), pp. 1–1. DOI: 10.1109/JESTPE.2021.3053467.

[4] L. Ortombina, D. Pasqualotto, F. Tinazzi, and M. Zigliotto. "Magnetic Model Identification for Synchronous Reluctance Motors Including Transients". In: *2019 IEEE Energy Conversion Congress and Exposition (ECCE)*. 2019, pp. 3196–3202. DOI: 10.1109/ECCE.2019.8913164.

[5] Ludovico Ortombina, Dario Pasqualotto, Fabio Tinazzi, and Mauro Zigliotto. "Magnetic Model Identification of Synchronous Motors Considering Speed and Load Transients". In: *IEEE Transactions on Industry Applications* 56.5 (2020), pp. 4945–4954. DOI: 10.1109/TIA.2020.3003555.

[6] D. Pasqualotto, A. Navarro Navarro, M. Zigliotto, and J. A. Antonino-Daviu. "Automatic Detection of Rotor Faults in Induction Motors by Convolutional Neural Networks applied to Stray Flux Signals". In: *2021 22nd IEEE International Conference on Industrial Technology (ICIT)*. Vol. 1. 2021, pp. 148–153. DOI: 10.1109/ICIT46573.2021.9453624.

[7] D. Pasqualotto, A. Navarro Navarro, M. Zigliotto, J.A Antonino-Daviu, and V. Biot-Monterde. "Fault Detection in Soft-started Induction Motors using Convolutional Neural Network Enhanced by Data Augmentation Techniques". In: *IECON 2021 The 47th Annual Conference of the IEEE Industrial Electronics Society*. IEEE, 2021, in Press.

[8] D. Pasqualotto and M. Zigliotto. "A comprehensive approach to convolutional neural networks-based condition monitoring of permanent magnet synchronous motor drives". In: *IET Electric Power Applications* 15.7 (2021), pp. 1–16.

[9] D. Pasqualotto and M. Zigliotto. "Increasing Feasibility of Neural Network Based Early Fault Detection in Induction Motor Drives". In: *IEEE Journal of Emerging and Selected Topics in Power Electronics* (2021, in Press).

[10] Dario Pasqualotto, Fabio Tinazzi, and Mauro Zigliotto. "Enhanced solar water-pumping system driven by a synchronous reluctance motor". In: *2021 22nd IEEE International Conference on Industrial Technology (ICIT)*. Vol. 1. 2021, pp. 365–370. DOI: 10.1109/ICIT46573.2021.9453546.

[11] Dario Pasqualotto, Fabio Tinazzi, and Mauro Zigliotto. "Model-Free Current Loop Autotuning for Synchronous Reluctance Motor Drives". In: *Automation* 1.1 (2020), pp. 33–47. ISSN: 2673-4052. DOI: 10.3390/automation1010003. URL: https://www.mdpi.com/2673-4052/1/1/3.

"«Che c'entra la parola devono? Qui non ci sono né permessi,
né divieti. Soffrano pure, se hanno pietà della vittima...
La sofferenza e il dolore sono sempre inevitabili
per una coscienza sensibile e per un cuore profondo.
Gli uomini veramente grandi, secondo me, devono
provare una gran tristezza su questa terra,» aggiunse
in un tono meditabondo che mal s'accordava
con quello della conversazione."

— Fëdor Dostoevskij, *Delitto e Castigo*

ACKNOWLEDGEMENTS

Another great brick has been lied in the wall of my life with the end of my PhD. I have to be proud of my work but it certainly wouldn't have been the case if my family, friends and colleagues were not on my hip. So, a sincere thank to all of them is a pleasant duty.

I would like to thank my supervisor, prof. Mauro Zigliotto. In these years, his suggestions and patience have supported and helped me from both the technical and life choices point of view. A great help came also from my predecessors in the EDLabVI: Dr. Fabio Tinazzi and Dr. Ludovico Ortombina. After three years, my knowledge has changed but I still see them as two lighthouses when I'm confused in the electric drives sea. Thank to them and all the past and more recent colleagues in the laboratory, I spent very enjoyable time within and outside the workplace, especially in this last year.

A special thank goes to my family: my father and mother, whose characters I identify myself more and more, and to my brother and sisters who are always ready to help me and have a good laugh with me.

I'm really thankful of friends, as I always felt them as a cornerstone of my life. I spent with Andrea, Davide, Manuele, Fabio, Stefano and Alberto countless and unforgettable moments. They are as brothers for me. The remaining components of our company complete the picture of my funniest and beloved memories. I think that I spent an enviable childhood and, in spite of the fast pace of life, every evening with them is like being sixteen years old again.

My true pillar of strength is my girlfriend, and nearly wife, Sofia. She gives meaning to everything around me and I would not be here without her. Never more than now, when I often feel as I got ahead of myself, I recognize her tireless ability to keep me going. I will never cease to be grateful for her existence.

CONTENTS

LIST OF TABLES

LIST OF FIGURES

ACRONYMS

PMSM	Permanent Magnet Synchronous Motor
IM	Induction Motor
PM	Permanent Magnet
CNN	Convolutional Neural Network
MCSA	Motor Current Signature Analysis
MTPA	Maximum Torque Per Ampere
FEA	Finite Element Analysis
ANN	Artificial Neural Network
AI	Artificial Intelligence
EMF	Electro-Motive Force
STFT	Short Time Fourier Transform
FFT	Fast Fourier Transform
CWT	Continuous Wavelet Transform
ReLU	Rectifier Linear Unit
LUT	Look-Up Tables
b-EMF	back-Electro Motive Force
FC	Fully Connected
SGD	Stochastic Gradient Descendent
DM	Dragging Motor
SVM	Space Vector Modulation
VSC	Voltage Source Converter
FCP	Fast Control Prototype
ADC	Analog to Digital Converter
RC	Random Cropping
BR	Change in Brightness
TT	Time Translation
FT	Frequency Translation
GN	Addition of Gaussian Noise

DA Data Augmentation

H Healthy

1BB One Broken Bar

2BB Two Broken Bars

KF Kalman Filter

EKF Extended Kalman Filter

UNFCCC United Nations Framework Convention on Climate Change

COP Conference of the Parties

SynRM Synchronous Reluctance Motor

RBF Radial Basis Function

Lin Linear

Hy Hybrid

NL Non Linear

HVAC Heating Ventilation and Air-Conditioning

IPM Interior Permanent Magnet

EEMF Extended Electromagnetic Force

DFO Direct Flux Observer

PLL Phase Locked Loop

NARMAX Nonlinear AutoRegressive Moving Average with eXogeneous inputs

1

INTRODUCTION

Once only a remote concern, climate change is now an existential threat and the greatest challenge facing the present and future generations. Human activities have been emitting greenhouse gases and CO_2 since the industrial revolution, heavily modifying the global environmental conditions. Even now, the footprint that humanity is leaving leads to an always warmer world. It is sufficient to observe how the greenhouse gas emissions are still growing year by year in the world and in the top-emitter countries (Figure 1.1).

The phenomena is inherently global and it afflicts the whole planet surface, no matter where or by whom they are emitted. The world today is 1.1 °C warmer than in pre-industrial times. The consequences of this warming are dramatic, as seen in the increase in intense floods and fires and extreme weather events of the past decade. Rapid, deep and transformative change is needed throughout society, not only to reduce emissions and stabilize global temperatures, but also to build a safer, healthier and more prosperous future for all.

The progressive efforts made by the United Nations Framework Convention on Climate Change (UNFCCC) are gradually defining the global guidelines and limits which should stabilize the greenhouse gas concentration to an acceptable level [12]. According to the Intergovernmental Panel on Climate Change report of 2018 "Human activities are estimated to have caused approximately 1 °C of global warming above pre-industrial levels... Global warming is likely to reach 1.5 °C between 2030 and 2052 if it continues to increase at the current rate". It also specifies the feasibility of the 1.5 °C target provided that deep emissions reductions are applied throughout the world. Moreover, the report finds that the 2 °C temperature increase limit specified during Conference of the Parties (COP) 21 is no more sufficient to avoid catastrophic anthropogenic interferences on the earth's climate system.

In order to avoid the 1.5 °C of global warming limit a reduction of the CO_2 emission levels by about 45 % by 2030 (compared to 2010 values) is advisable [24]. According to this guidelines, the international pollution constrains and governmental policies for the next years should have been defined during COP 25. Actually, these agreements have not been reached yet, although a growing number of ambitious Countries have committed to reduce their carbon emissions to net zero by 2050.

An example is the european union which with the european green deal wants to reduce the greenhouse gas emissions by at least 55 % below 1990 levels by 2030 and to become climate neutral by 2050. On 14 July 2021, the european commission adopted a series of 55 legislative proposals covering a wide range of policy areas including climate, energy, transport and taxation to achieve the posed target.

In the world, several activities have been identified as main responsible for green-

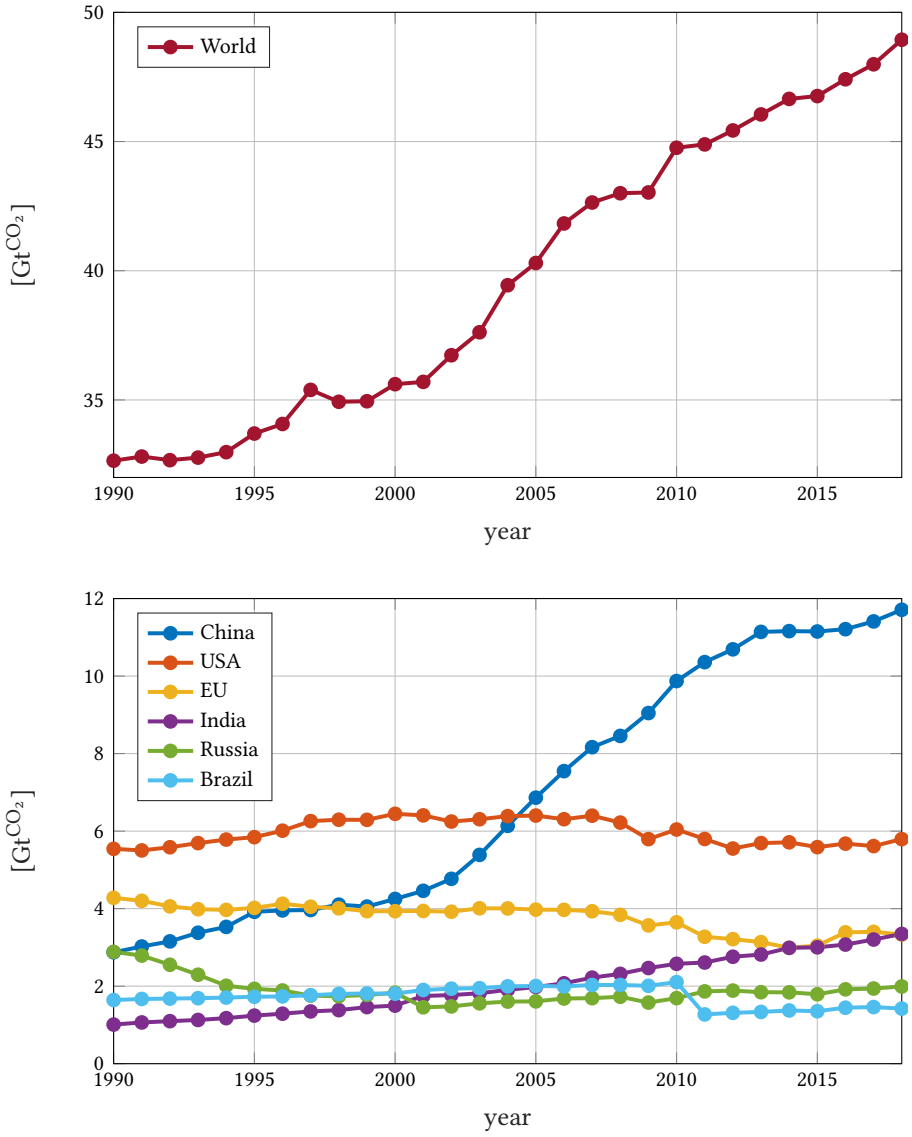

Figure 1.1. Total amount of greenhouse gas emissions of the world and top emitters [50].

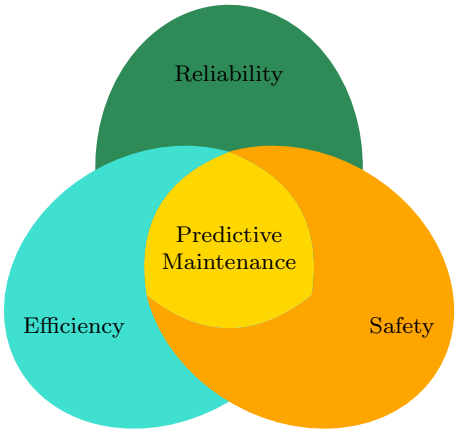

Figure 1.2. The frame of my predictive maintenance project.

house gas emissions. The actual main CO_2 sources can be framed into 5 sectors, namely (in decreasing order of emissions): energy, agriculture, industrial processes, waste and land-use change and forestry. It is worth noticing that the energy sector is responsible for more than 75 % of the actual world emissions [50], while agriculture (the second source) generates the 12 % of emissions.

It is evident how operating and improving the energy production and management assumes a paramount importance for the next generation sustainability. The majority of this energy is used by the industry and for transportations in the form of driving energy. For what concerns electrical energy the International Energy Agency stands that electric motor driven systems are responsible for 53 % of global electricity use [2]. Electric motors and drives therefore represent a focal point for an optimization of the actual energy employment.

1.1 *The frame of predictive maintenance*

The aforementioned optimization process passes surely through the usage of more efficient motors and a better design of the whole drive. Nonetheless, also an improved maintenance and recycle of the electrical machine can heavily affect the achievement of the desired goals of efficiency. The damage of a motor can easily cause a cascade interruption of different parts of the production plant, thus causing surely an increase of costs but also a waste of energy. Another waste is in term of components and devices that must be substituted when a fault occurs. In this case, if the fault incoming condition is properly recognized in advance, it could be possible to repair the machine or avoid the damage of other plant components before making them unusable. Therefore, an additional improvement in terms of avoiding squandering can be achieved.

In addition to the efficiency concept, there are other two topics that cannot be forgotten during the development of an adequate condition monitoring of modern systems. They are the reliability and safety issue (Figure 1.2).

In order to contextualize them within the actual industrial scenario, it is worth noticing that from the industrial point of view, the traditional maintenance approaches as the run to failure methods or preventive maintenance are often no more suitable and admissible from the reliability point of view. The modern complexity and cost of industrial systems leave less room for malfunctions and performance degradation. While the scheduling of not-necessary, preventive upkeeps is ever more demanding and time-consuming. Therefore the prompt recognition of abnormal conditions and incoming failures is gaining uppermost relevance.

From the safety point of view, it is also easy to understand how the continuous condition monitoring of the plant can be very useful to prevent potential dangerous conditions for human operators.

As a meaningful example, the growing electrification of transportations will likely benefit from an improved maintenance policy. The huge amount of energy required by modern mobility gives to the electrical machines a primary relevance in the paradigm of smart cities. It is sufficient to know that according to [5], in 2019 less than 2 % of light vehicle production was accounted for by battery electric vehicles models. But the forthcoming forecasts estimate that the 40 % of all cars sold across the globe in 2027 will be electrified, rising to over 95 % by 2050. It is easy to understand that the realization of a system able to alarm the driver if the car will soon need some maintenance would be very useful from all the efficiency, reliability and safety points of view.

1.2 *The predictive maintenance in the electric drives field*

In the electric drives field, there is a growing need to detect and identify any incoming failure as soon as possible [32] in order to improve the system reliability. The research is increasingly focusing on techniques and methodologies able to give an augmented autonomy to modern industrial drives. This capability allows a more intelligent and efficient scheduling of the interventions on the plant according to the predictive maintenance paradigm.

The solution of the condition monitoring problem is composed by three steps, namely the fault detection, isolation and identification. In other words, understand that a fault has occurred, detecting where and finally comprehend how much severe is the fault degree [32]. The complexity of the problem and the many contributing factors make the solution not trivial.

Several technical papers have dealt with the fault detection issue in electric motors and they have been collected and summarised in different reviews on condition monitoring for Induction Motors (IMs) [61, 81, 118] or for Permanent Magnet Synchronous Motors (PMSMs) [110]. According to most of them, failure conditions on an electric motor can be classified into three categories which are electrical, mechanical or magnetic faults.

1.2.1 Electrical faults

The electrical faults are related to the health conditions of the stator winding and they can mainly involve interturn shorts, open circuit faults or grounding [15, 100,

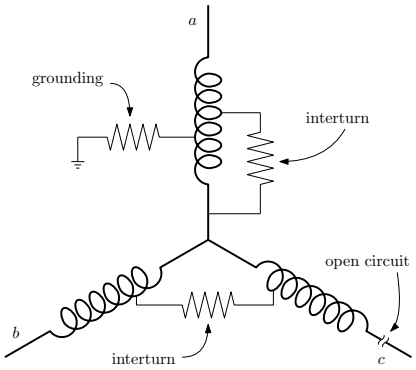

Figure 1.3. Possible electrical faults in three-phase motor windings.

110]. Whatever motor is considered, it is composed by an electrical winding, these failure conditions can occur on each type of motor. In three-phase AC systems, the mentioned three types of electrical faults can be represented as in Figure 1.3.

Since the nature of these faults, the electrical variables as voltages or currents are particularly sensitive to these fault conditions. The major part of the winding condition monitoring works are based on the analysis of these signals [10, 40, 45, 108].

1.2.2 Mechanical faults

Mechanical faults are mainly related to the rotor that being the part in movement it is the most prone to this type of failure. Faults can be classified into eccentricities, ball-bearing defects or damages on the rotor bars, for IMs [55, 95].

Let's identify as O_s and O_r the barycentres of cross-sections of stator and rotor respectively. When some eccentricity e is present they will not coincide. In function of the position of the rotation centre C on which the rotor rotates, three different types of eccentricities can be defined:

- No eccentricity: if $C \equiv O_s \equiv O_r$
- Static eccentricity: if $C \equiv O_r \not\equiv O_s$
- Dynamic eccentricity: if $C \not\equiv O_s$ and $C \equiv O_r$
- Mixed eccentricity: otherwise

The faults that can occur on ball bearings are subdivided in function of their position. The bearing is composed of 4 different elements which can be damaged: the outer and the inner races, the balls and the protective cage.

A rough schematic of a ball bearing with its components can be observed in Figure 1.5. Some additional features can be recognized: the balls diameter D_B, the pitch diameter D_P and the balls contact angle γ. According to [62], some principal fault-related vibration frequencies can be derived as main effect of the damage of ball bearings.

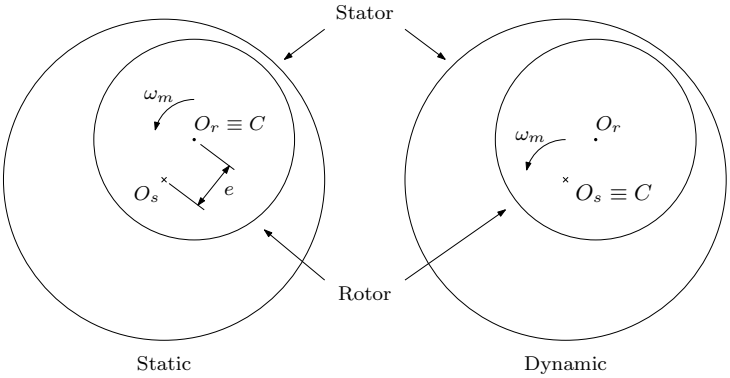

Figure 1.4. Static and dynamic eccentricity models.

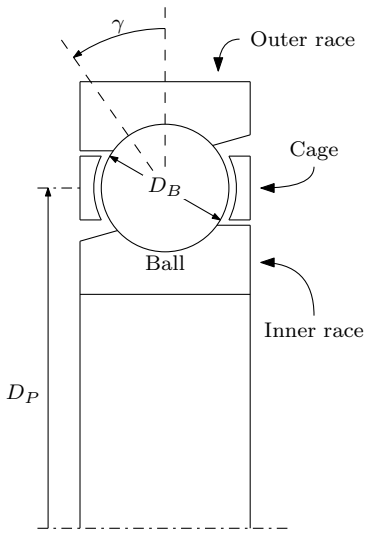

Figure 1.5. Ball bearing components.

$$\begin{aligned}
\omega_C &= \frac{1}{2}\omega_m \left(1 - \frac{D_B \cos(\gamma)}{D_P}\right) \\
\omega_{OR} &= \frac{N_B}{2}\omega_m \left(1 - \frac{D_B \cos(\gamma)}{D_P}\right) \\
\omega_{IR} &= \frac{N_B}{2}\omega_m \left(1 + \frac{D_B \cos(\gamma)}{D_P}\right) \\
\omega_B &= \frac{D_P}{2D_B}\omega_m \left(1 - \frac{D_B^2 \cos^2(\gamma)}{D_P^2}\right)
\end{aligned} \tag{1.1}$$

Ball-bearing defects and eccentricities are very common and they can afflict any type of motor. Their main effect is a radial displacement of the rotational axis due to the creation of tangential forces and so the more direct method for a fast recognition of this condition is through the measurement of this vibrations. Different sensors can be used. The most obvious and historically used are the accelerometers. This has been one of the first approaches to the condition monitoring of electric motors. Even though modern accelerometers are very cheap, the usage of this sensor can be problematic in all the cases in which there is not enough space for sensor positioning or in very noisy environments from vibrations point of view as it is typical in industry.

A quite modern approach is also the usage of thermographic cameras [68]. This tool features a very low invasive nature, since a simple photo of the plant can give useful information on it. As a matter of fact, the vibrations generated by the faults cause some heat dispersion, with a local increase of the temperature of the motor. In turn, this enables to estimate the conditions of the bearings. Nonetheless, it is easy to understand that although it is a very interesting and pioneering approach, it is quite difficult to automatize.

The third mechanical damage refers to the broken bars of the rotor in an IM, and it consists in the interruption of the bar conductivity into the rotor squirrel cage. Since IMs earned a wide diffusion, the broken bar damage was studied in literature, making available several works in which the behaviour of the faulty IM is examined and analysed [38, 80].

Differently from the previous cases, this fault features an imbalance in the three-phase system represented by the squirrel cage. Its main effect is a change of rotor linking circuit, an imbalance in the rotor currents and so in the flux linkage. So even if the fault has a typical mechanical nature, its effects are prevalently magnetic and electric. The observation of the stray flux around the motor is eligible as a very good fault index for the prompt recognition of this incoming failure. Its analysis through external sensor coils has drawn an increasing attention due to the low cost, simplicity and non-invasive nature [53].

As another distinctive approach, different versions of the Kalman Filter (KF) have been applied in literature for the estimation of the rotor resistance [96, 117]. A broken bar fault leads to an increase of this value and comparing its estimate with the nominal value it is possible to understand the health conditions of the rotor. Nonetheless, for overcoming the tuning and estimation errors of the filter very complex structures are needed, that still lack of experimental verifications [117].

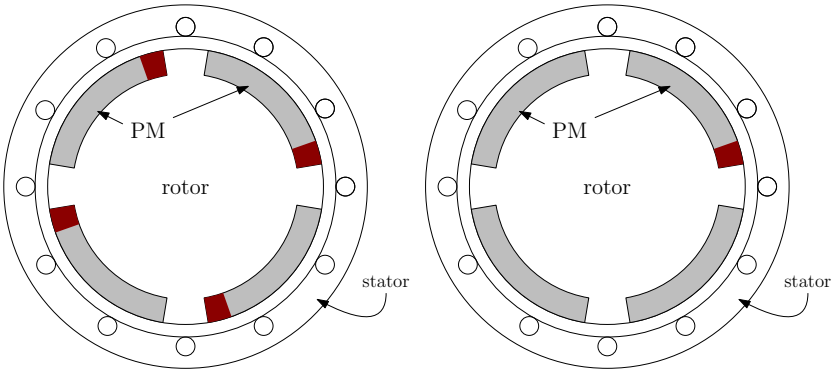

(a) Global demagnetization. (b) Partial demagnetization.

Figure 1.6. Different types of demagnetization.

1.2.3 Magnetic faults

Finally, magnetic faults concern the demagnetization of permanent magnets, which is the partial loss of the residual flux density [27]. This loss can affect all the rotor Permanent Magnets (PMs), and so it is referred as global demagnetization, or only some PMs, giving rise to partial demagnetization. A scheme of the types of demagnetization that can occur on a motor with PMs is reported in Figure 1.6.

Given the damaged component considered, in this case the analysis of the flux with external or built-in sensors is surely the more effective countermeasure.

1.3 *The approach of this thesis*

Different key concepts have been used as cornerstones in the development of this thesis. They are reported and explained in the following sections.

On the wave of the recent wide diffusion of innovative Artificial Intelligence (AI)-based techniques, the development of neural networks tailored for the electric drives field is surely one of the main innovative contributes of this thesis. Convolutional Neural Networks (CNNs) have been used for the condition monitoring of the motors. This type of network, particularly suitable for image classification tasks, allowed to automatically extract the useful features of the current signature and recognize the health of the motor.

Another type of network, the Artificial Neural Network (ANN), was instead efficiently used for the accurate modelling of the motor magnetic behaviour. As a matter of fact, the capability of this network to learn and fit complicated multiple input, multiple output static functions, elects it as effective tool for the motor magnetic non linearities modelling.

1.3.1 No additional sensors

As observed from the previous exploratory analysis, each fault can be assessed more simply if a characteristic belonging to its own class is observed. Nonetheless, this approach is surely quite expensive considering all the possible damages that can occur on an electric motor. Moreover, the implementation of several methods based on difference sensor measurements gives itself a worsening of the reliability issue.

Recalling the above-mentioned faults some considerations on their detectability observing the motor currents can be drawn. As they are directly related to the stator windings, all the electrical faults are very prone to be recognized observing motor currents. Eccentricities and ball-bearing defects give a variable airgap length to the magnetic flux. The flux linkage on the stator windings is affected by this variation and a change in motor currents can be observed. Similar observations can be derived considering the broken bar fault and the demagnetization of PMs. As an example, Faiz et. al. in [28] proposed a revision and comparison of several current-based fault detection indexes for the demagnetization fault with some extensions also to eccentricities.

Therefore, as a more effective approach one can consider that all failures somehow affect the airgap flow distribution and consequently the magnetic path of the motor from which the currents are dependent. In principle, any abnormal operating condition can be detected through the analysis of motor currents. This approach is not new. It is called Motor Current Signature Analysis (MCSA) [104] and it has great potentiality since it does not require any additional hardware with respect to a standard industrial drive, maintaining cost-effectiveness and reliability.

In the development of this thesis, I adopted this approach as a comprehensive tool potentially able to recognize different faults with the same architecture. The motor currents were chosen as common fault index to all faults, obtaining a reduction of required sensors, enhancing the reliability and the cheapness of the solution.

Not all the described faults have been analysed in this dissertation. The interturn short circuit and the demagnetization faults have been studied for PMSMs and the broken bars for IMs.

1.3.2 Automatization of the fault index classification through CNNs

A great effort has been made in the past to identify possible fault indexes, highlighting their drawbacks and potentialities. The nowadays great question is to develop a procedure for the automatic recognition of the failure. As a first challenge, this thesis wants to do a step forward in this direction taking advantage of a keen approach to AI and in particular with the use of CNNs.

Given the recent growing trends of Internet of Things and Industry 4.0 and essentially thanks to the modern availability and possibility to manage a huge amount of data and information, the knowledge-based or data-driven techniques are acquiring an increasing importance [36]. The basic idea is always to develop an expert classifier, based on the elaboration of a proper fault index, and trained on a big volume of historical data, that automatically detects an incoming failure. ANNs can be chosen as suitable tools for this kind of problem as Nandi et al. report in [81]. They are gaining popularity because of their physical model-free solutions.

One of the first applications is the ANN technique applied by Chow et al. in [62] to detect incoming failures on ball bearings of an electric motor. In that study, the vibrations, measured through specific accelerometers, were used as index to understand the bearing health level and the classification was performed by an AI-based algorithm. The study was soon followed by many others, always using the ANN as enabling technology for the condition monitoring problem [23].

Nevertheless, a recent research [35] has shown how a CNN performs better than the traditional multi-perceptron ANN, thanks to some inherent features that will be highlighted later on in chapter 3.

Promising results were reported in [77] and [111], in which a CNN was applied on induction motors in order to identify different types of fault. The main focus was on the transformation of a current sequence into a 2D image, in order to use a traditional 2D CNN as it is usually applied to image recognition. The former illustrates the preliminary findings using a specially designed CNN and a time/frequency-domain bearing vibration analysis, in order to detect ball bearing, rotor bar and winding insulation faults. The latter used an already trained LeNet-5 network, presenting a new signal-to-image conversion method aimed at eliminating the experts' experiences as much as possible.

One step beyond was performed by Ince in [49], demonstrating that 2D transformation is not necessary and a simple 1D convolution can be applied reaching a good level of accuracy in the dichotomic choice between healthy and faulty induction motors. Finally, an application of a 1D CNN on PMSM monitoring was considered in [57], where all the main faults which can occur on a PMSM were successfully recognized.

The problem remains the CNN training, which requires a large batch of training data from the field. Without them, any technique is destined to remain almost a pure academic exercise.

1.3.3 Affordable realization of the training dataset

At least two main points for the realization of the training dataset are addressed in the present thesis. The first is that in all the aforementioned AI-based works the dataset was generated by damaging a real motor for each fault and fault level. The set was then realized acquiring current records at different levels of speed and current. This methodology is very expensive, unpractical and scarcely affordable from an industrial point of view. A second aspect that requires attention is that so far a totally black box approach has been applied. Useful information on motor behaviour, features of the phase current patterns and network characteristics were neglected. The lack was compensated by the CNN capabilities, at the cost of increasing enormously and uselessly the complexity of the network and the related training problems. In the electric drives world, this may be not a successful direction.

The principal aim of this thesis is the development of proper solutions to the generation of the training dataset which should be effective and efficient from both economical and industrial points of view. As a completely new challenge in the electric drives field, the solution is composed by different innovative techniques which can be collected under the class of Data Augmentation (DA) methods. In fact, even though the modern concepts of Big Data and Data Mining are helping in providing these training

datasets, a simpler and more immediate step forward is allowed by this approach. These techniques were born as artificial (geometrical, mathematical) transformations for the increase of the available training dataset, but nowadays they assume a more wide and general meaning [74, 112].

In the following, the first step was the realization of very accurate models, able to generate artificially the training samples. It is easy to understand the great impact of the development of this model-based DA technique. Only a reduced number of prototypes are necessary with the only aim to fine tune the model, that in future will provide results similar to a real motor, including also the spurious harmonics overlapped to the fundamental behaviour of the motor. Since this is the main source for the realization of the training dataset, its precise design assumed great importance during the thesis work. In particular, the extensive usage of Finite Element Analysis (FEA) and the implementation of custom ANNs allowed to accurately model the magnetic behaviour of the motors. The modelling of the fault behaviour and its effects on the stator currents are accurate. Finally, for a proper and wide training dataset generation, some additional DA techniques have been selected and applied to the elaboration of signals coming from electric drives. Their use represents a completely innovative approach in the electric drives field, and the study of their effects on the final condition monitoring system accuracy is another distinctive contribution.

1.3.4 Magnetic model identification through ANNs

In addition to the resolution of classification problems, neural networks can be used to manage regression tasks [39, 41]. The availability of a training set of input-output points of the function that has to be fitted allows to back-propagate the estimation error and to tune the network weights in order to optimally fit the available training points.

In particular, the usage of different non linear activation functions and the powerful given by the inter-connection of a great number of neurons elect ANNs as ideal candidates to fit complex multi-variate functions. This tool is especially suitable for "black-box" approaches in which no particular knowledge on the function that has to be fitted is required or available. As a matter of fact, the fitting through an interpolating function requires to specify its architecture which should be brought in line with the complexity of the problem, thus involving some additional knowledge on the issue. Surely this requirement is still present for the definition of the network structure (number of neurons and layers), but provided that a good training dataset is available, this strict relationship becomes lighter. ANNs are a powerful tool for mapping unknown non linear relationships in different applications. As an example an ANN has been used in [113] to compensate observer estimation errors in the sensorless control of an IM. Another one is reported in [105], in which the ANN has been exploited to identify a Nonlinear AutoRegressive Moving Average with eXogeneous inputs (NARMAX) model of DC motors.

The interpolation of the inherently complex interactions between motor structure, currents, and magnetic fluxes can be considered as ideal application of an ANN. Therefore, also in this case paving the way to more intelligent drives, ANNs have been extensively used in this thesis to fit the magnetic model of IMs (chapter 5) and

Synchronous Reluctance Motors (SynRMs) (chapter 6).

1.4 *Dissertation outline*

First of all, in chapter 2 a brief recall of the motors considered throughout the dissertation is reported. This part surely does not represent a complete and deep treatise of the motor features and behaviours. It is aimed only to recall the main theoretical background needed for a straightforward understanding of the following chapters.

Chapter 3 considers the predictive maintenance of PMSMs. These motors are widely used in modern applications, such as electrical vehicles, wind energy, home, and industrial appliances. Their popularity is due to the simple and compact structure, easy manufacturing, and high power density, more precise control compared with other electrical motors, and high power factor over constant torque region [28]. The stator currents in steady-state conditions are elaborated by a CNN. A proper training dataset is generated artificially through an accurate model of the PMSM and the implementation of different data augmentation techniques.

IMs are considered in chapters 4 and 5. The robustness and cheapness make them the most widespread electric motors in many industrial contexts. Although the well-known reliability even in harsh environments, damages are still possible, and a quite common fault is related to the interruption of one or more bars in the rotor of a squirrel cage IM.

Chapter 4 is the result of an international collaboration with professor Daviu of the Universitat Politecnica de Valencia in Spain. He is an expert in the development and study of informative indexes for the recognition of failures in IMs. Exploiting one of these indexes, the measurement and analysis of the stray flux, my efforts were devoted to the design and training of the CNN.

The stray flux measurements are used as fault index during the start-up of the motor. This signal claims a time vs frequency tool and the elaboration of data in form of matrix needing a complete redesign of the CNN structure and data augmentation methods. In this case a model able to accurately describe the stray flux of the motor is quite impossible to achieve. Therefore, a small experimental dataset was used, enlarging it properly through an intense application of data augmentation.

Conversely, in chapter 5 the stator currents of the IM are considered for the recognition of broken bars during the start-up, thus avoiding the requirement of additional stray flux sensors used in the previous chapter. In the proposed implementation, the classification is performed through a CNN on the image of the Continuous Wavelet Transform (CWT) elaborated on the start-up current. A model was used for the artificial generation of the whole training dataset. The use of simulation-based data augmentation technique was the exploration of both different start-up situations and fault conditions (more broken bars, for example). The result was an exhaustive training, to which is added the ease of including new situations, without resorting to experimental measurements, more complex to set up.

According to the archetype of a more efficient energy consumption, chapter 6 deals with SynRMs as an optimal trade-off between costs and efficiency, which are the main problem of PMSMs and IMs respectively. During the past years, SynRMs have collected

an increasing interest from the research world and, recently, they are also spreading into the industrial one. This wide diffusion is principally caused by their inherent efficiency combined with the absence of expensive PM materials. These properties, compared respect to the low efficient IM and costly PMSM, elect the SynRM as valid alternative for the reduction of the human environmental footprint, in particular for all the low-medium performance variable speed drive applications.

Nonetheless, the present motor energy consumption is still majorly driven by IMs. To speed-up their replacement to more efficient SynRMs, work is still needed. A part of this task is surely the enhancing of sensorless operating capabilities of the SynRM, gaining an increase in cheapness, robustness and compactness of the system. Moreover, as common thread among the chapters, the reliability of the drive is augmented in this manner. The avoidance of expensive and fault-prone sensors, as the position encoders are, surely helps in limiting undesired failures and unexpected shutdowns.

Due to their robustness and adaptability, position estimators based on the extended Extended Kalman Filter (EKF) have been used in all PMSMs for decades. The time has come to extend their use to reluctance motors as well and chapter 6 focuses on the elements that hinder the transition. It is shown that all passes through the availability of an accurate motor magnetic model, which can be obtained by AI tools. The chapter uses a Radial Basis Function (RBF)-ANN to derive an analytical form of the highly non linear magnetic model of a SynRM. Improvements in the state estimation function make the EKF not only feasible, but applicable over an extended range of speeds. The experimental session will compare different implementation possibilities, concluding with a new hybrid algorithm as the best compromise between accuracy and computational load.

2

AC MOTOR MODELS

Since their invention, electric motors have gathered increasing interest all around the world and they are the modern largest driving solution in the globe. Different structures and torque generation principles have been introduced but the modern industrial applications are based principally on radial flux AC machines. The motors considered in this thesis are the Permanent Magnet Synchronous Motor, the Synchronous Reluctance Motor and the Induction Motor.

2.1 *Permanent Magnet Synchronous Motors*

In PMSMs the electrodynamic principle is exploited for the generation of the torque as interaction between a rotor and a stator flux. As the other AC machines considered in this thesis, the stator flux is produced by a three-phase winding system located within the slots of a series of metal sheets stacked together. The rotor flux is instead permanently generated by some PMs superficially mounted on the rotor. This architecture leads to an isotropic structure of the rotor. A graphical sketch of the cross-sectional structure of this motor is reported in Figure 2.1. In red are indicated the north pole of PMs while in blue the south pole.

As principal feature of this motor, the presence of PMs avoids the necessity to magnetize the rotor through currents. This, together with the isotropic characteristic, brings a series of advantages: the avoidance of fault-prone elements as the brushes, the absence of rotor Joule losses that reduce the maximum achievable torque. This motor exhibits a extremely linear magnetic behaviour that simplifies the control. Among the main drawbacks are the cost and heavy environment impact caused by the extraction of the rare earth needed for the production of PMs.

The voltage balance equations of the three-phase stator windings are:

$$\begin{aligned} u_a &= Ri_a + \frac{d\lambda_a}{dt} \\ u_b &= Ri_b + \frac{d\lambda_b}{dt} \\ u_c &= Ri_c + \frac{d\lambda_c}{dt} \end{aligned} \tag{2.1}$$

in which $u_{a,b,c}$, $i_{a,b,c}$ and $\lambda_{a,b,c}$ are respectively the stator voltages, currents and flux linkages. R represents the phase stator resistance. The flux linkage is composed of two components: one is due to the flux generated by stator currents while the other is due to PMs in the rotor. As an example, for phase a:

$$\lambda_a = L_a i_a + M_{ab} i_b + M_{ac} i_c + \lambda_a^{mg} \tag{2.2}$$

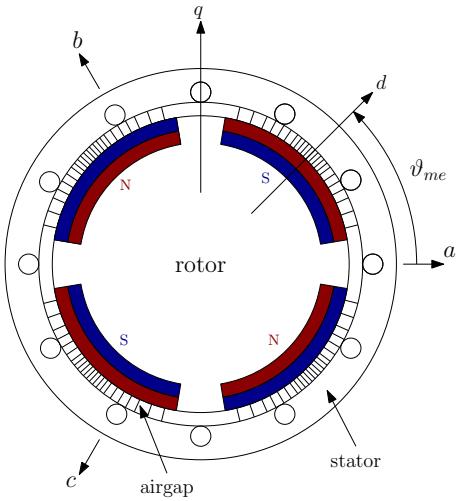

Figure 2.1. Graphical sketch of the structure of a PMSM.

with L_a as self inductance, M_{ab} and M_{ac} as mutual inductances with axes b and c, λ_a^{mg} as the portion of permanent magnet flux linked with phase a. If a fault occurs M_{ab} can be in general different from M_{ac}. This is the case when the interturn fault is studied as observed in section 3.1.3. In case of healthy motor $M_{ab} = M_{ac} = M$ and under the hypothesis $i_a + i_b + i_c = 0$, equation (2.2) can be rearranged:

$$\lambda_a = L_a i_a - M i_a + \lambda_a^{mg} = L i_a + \lambda_a^{mg} \tag{2.3}$$

in which $L = L_a - M$ is defined as synchronous phase inductance.

From this notation it is possible to move on to space vector notations which are simpler to manage. These can be defined either in a stationary reference frame $\alpha\beta$ or synchronous with the rotor dq.

A particular transformation to the stationary reference frame is used in the dissertation for the modelling of the interturn fault and it is properly described in section 3.1.3.

The dq reference frame is defined fixing the d axis along the direction of north poles of PMs in the rotor and it is assumed that the rotor position ϑ_{me} is equal to zero when the d axis is aligned with phase a. The relative model equations can be achieved applying the Park transformation

$$T_P = \frac{3}{2}\begin{bmatrix} \cos(\vartheta_{me}) & \cos\left(\vartheta_{me} - \frac{2\pi}{3}\right) & \cos\left(\vartheta_{me} - \frac{4\pi}{3}\right) \\ -\sin(\vartheta_{me}) & -\sin\left(\vartheta_{me} - \frac{2\pi}{3}\right) & -\sin\left(\vartheta_{me} - \frac{4\pi}{3}\right) \\ 1/\sqrt{2} & 1/\sqrt{2} & 1/\sqrt{2} \end{bmatrix} \tag{2.4}$$

to equation (2.1). The PMSM electrical dynamic voltage balance equations in dq refer-

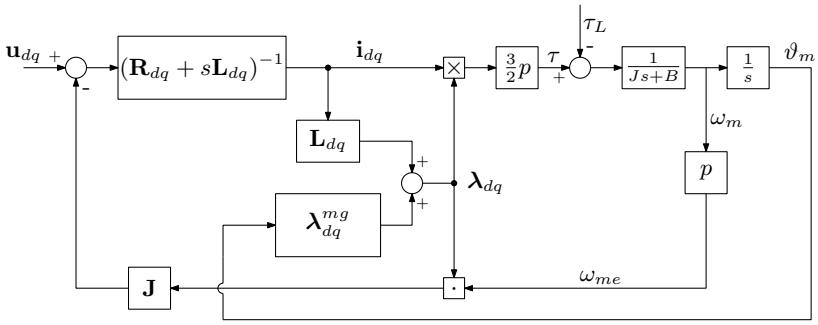

Figure 2.2. Block diagram of a PMSM model.

ence frame are:

$$\mathbf{u}_{dq} = \mathbf{R}\mathbf{i}_{dq} + \frac{d\boldsymbol{\lambda}_{dq}}{dt} + \mathbf{J}\omega_{me}\boldsymbol{\lambda}_{dq} \quad \text{with} \quad \mathbf{J} = \begin{bmatrix} 0 & -1 \\ 1 & 0 \end{bmatrix} \tag{2.5}$$

where $\mathbf{u}_{dq} = \left[u_d, u_q\right]^T$, $\mathbf{i}_{dq} = \left[i_d, i_q\right]^T$ and $\boldsymbol{\lambda}_{dq} = \left[\lambda_d, \lambda_q\right]^T$ are the stator voltage, current and flux linkage vectors, respectively. $\mathbf{R} = diag\{R, R\}$, while $\omega_{me} = p\omega_m$ is the electromechanical speed, that is the pole pairs p times the mechanical speed ω_m. Making explicit the two contributes of the flux linkage the following equation is obtained.

$$\mathbf{u}_{dq} = \mathbf{R}\mathbf{i}_{dq} + \mathbf{L}_{dq}\frac{d\mathbf{i}_{dq}}{dt} + \mathbf{J}\omega_{me}\left(\mathbf{L}_{dq}\mathbf{i}_{dq} + \boldsymbol{\lambda}_{dq}^{mg}\right) \tag{2.6}$$

The PMSM model can be completed by considering the electromechanical torque:

$$\tau = \frac{3}{2}p\left(\lambda_d i_q - \lambda_q i_d\right) \tag{2.7}$$

and by describing the mechanical dynamics by a first-order system

$$\tau = B\omega_m + J\frac{d\omega_m}{dt} + \tau_L \tag{2.8}$$

with J and B as rotor inertia and viscous friction, respectively, and τ_L as load torque.

A block diagram of the complete dq mathematical model of a PMSM is reported in Figure 2.2. As it will be clear in section 3.1.1, it can be easily adjusted to take into consideration the position-related harmonics for the healthy and demagnetized cases. In the figure, the symbol $\cdot$ represents the scalar product, while $\times$ indicates the difference of the cross-products in (2.7).

2.2 *Synchronous Reluctance Motor Model*

While the stator is the same of a PMSM, in the rotor of a SynRM there is not any active element. It is designed to produce a variable reluctance path for the magnetic flux. Exploiting the variable reluctance torque generation principle, the preferential rotor position is the one which guarantees the minimum reluctance path. Also in this case

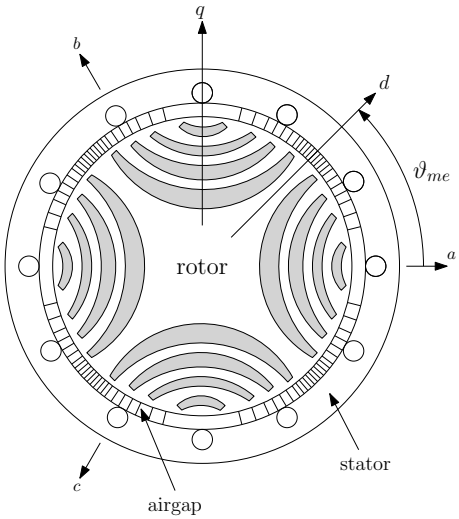

Figure 2.3. Graphical sketch of the structure of a SynRM.

there are not rotor currents and therefore the SynRM, as the PMSM, is characterized by high efficiency. While the absence of PMs gives an increasing importance to this motor in terms of costs, the variable reluctance structure is very prone to magnetic saturation and cross-coupling phenomena. Thus, the SynRM is more complex from the regulation point of view, requiring modern and innovative control techniques. A sketch of the cross-section of this motor is reported in Figure 2.3.

The mathematical model of a SynRM can be outlined in different reference frames. The analysis can start from the same voltage equations (2.1), in which, due to the absence of PMs the a flux linkage is only generated by the stator currents. Considering for example the phase a:

$$\lambda_a = L_a(\vartheta_{me})i_a \tag{2.9}$$

in which, it has been highlighted that for this motor a variable reluctance path its generated by the rotation of the rotor and so the phase self-inductance is variable with the rotor position.

In order to avoid the ϑ_{me} dependence of the inductive terms, the dq reference frame, synchronous with the rotor, is very common. The traditional coordinate system for the development of the EKF on synchronous motors is the stationary one ($\alpha\beta$), fixed with the stator. Therefore, a model of the SynRM in the $\alpha\beta$ framework is derived from the dq one.

The voltage balance of the stator circuit is expressed by the following matrix equation.

$$\mathbf{u}_{dq} = \mathbf{R}\mathbf{i}_{dq} + \mathbf{L}_{dq}(\mathbf{i}_{dq})\frac{d\mathbf{i}_{dq}}{dt} + \omega_{me}\mathbf{J}\boldsymbol{\lambda}_{dq}(\mathbf{i_{dq}}) \tag{2.10}$$

The variable names are the same used for the PMSM model described in section 2.1. Since this motor is subjected to saturation and cross-coupling effects of the magnetic

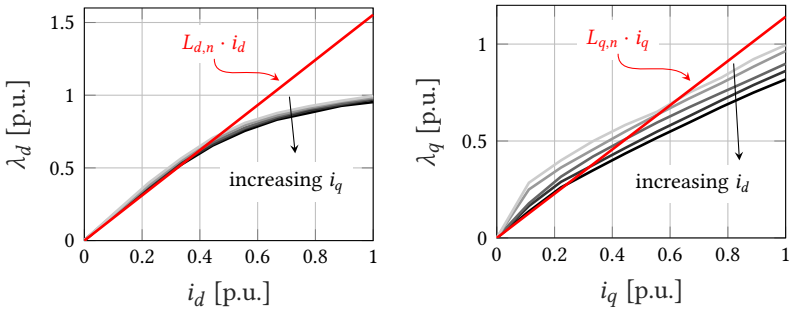

(a) Direct axis flux λ_d.

(b) Quadrature axis flux λ_q.

Figure 2.4. Fluxes to currents characteristics of the SynRM.

path even within the nominal current range, the inductance matrix

$$\mathbf{L}_{dq}(\mathbf{i}_{dq}) = \begin{bmatrix} L_d(\mathbf{i}_{dq}) & L_{dq}(\mathbf{i}_{dq}) \\ L_{dq}(\mathbf{i}_{dq}) & L_q(\mathbf{i}_{dq}) \end{bmatrix} \tag{2.11}$$

is defined as Jacobian of the fluxes $\boldsymbol{\lambda}_{dq}$ respect to the state variable $\mathbf{i}_{dq}$. The electromechanical speed is indicated with the symbol ω_{me} and it is equal to the pole pairs p times the rotor mechanical speed ω_m.

With this model, the non linear dependence of the fluxes and their derivatives on the motor currents are included in the definition of $\boldsymbol{\lambda}_{dq}$ and $\mathbf{L}_{dq}$.

In Figure 2.4 the fluxes to currents relations of the SynRM used in this thesis (Table 6.1) are reported as an example of typical magnetic behaviour of SynRMs. The curves are normalized in p.u. dividing the fluxes for their maximum values, which were respectively $\lambda_d^{max} = 0.978$ V s and $\lambda_q^{max} = 0.298$ V s. As it can be appreciated in the figure, the curves are strongly non linear and a non-negligible level of cross-coupling is also present. In the figures is also reported in red the magnetic behaviour if a nominal, linear, with no cross-coupling model is assumed. This is to highlight that even if the red model is surely less complex, some big differences between the model and the real behaviour of the motor are expected when the motor is heavy loaded. That feature will assume a critical importance during the implementation of the EKF in chapter 6.

The model can be completed with the same torque generation equation (2.7) and mechanical dynamics (2.8). Nonetheless, as it will be clear in chapter 6, the model of the mechanical dynamics will be simplified for the realization of the sensorless control algorithm. Therefore, it is here reported for the sake of completeness only but it is henceforth neglected.

In order to obtain a model particularly suitable for implementing the EKF, as required in chapter 6, a synchronous to stationary frame transformation is applied according to the following rotation matrix

$$T = \begin{bmatrix} \cos(\vartheta_{me}) & -\sin(\vartheta_{me}) \\ \sin(\vartheta_{me}) & \cos(\vartheta_{me}) \end{bmatrix} \tag{2.12}$$

deriving the $\alpha\beta$ notation:

$$\mathbf{u}_{\alpha\beta} = \mathbf{R}\mathbf{i}_{\alpha\beta} + \mathbf{A}\frac{d\mathbf{i}_{\alpha\beta}}{dt} + \omega_{me}\left(\mathbf{B}\mathbf{i}_{\alpha\beta} + \mathbf{C}\right) \tag{2.13}$$

Rearranged in state-space form, it becomes:

$$\frac{d\mathbf{i}_{\alpha\beta}}{dt} = \mathbf{A}^{-1}\left[\mathbf{u}_{\alpha\beta} - \mathbf{R}\mathbf{i}_{\alpha\beta} - \omega_{me}\left(\mathbf{B}\mathbf{i}_{\alpha\beta} + \mathbf{C}\right)\right] \tag{2.14}$$

Matrices **A**, **B** and **C** are defined by:

$$\begin{aligned}
\mathbf{A} &= \begin{bmatrix} L_\Sigma + L_\Delta\cos(2\vartheta_{me}) - L_{dq}\sin(2\vartheta_{me}) & L_\Delta\sin(2\vartheta_{me}) + L_{dq}\cos(2\vartheta_{me}) \\ L_\Delta\sin(2\vartheta_{me}) + L_{dq}\cos(2\vartheta_{me}) & L_\Sigma - L_\Delta\cos(2\vartheta_{me}) + L_{dq}\sin(2\vartheta_{me}) \end{bmatrix} \\
\mathbf{B} &= \begin{bmatrix} -L_\Delta\sin(2\vartheta_{me}) - L_{dq}\cos(2\vartheta_{me}) & L_\Sigma + L_\Delta\cos(2\vartheta_{me}) - L_{dq}\sin(2\vartheta_{me}) \\ -L_\Sigma + L_\Delta\cos(2\vartheta_{me}) - L_{dq}\sin(2\vartheta_{me}) & L_\Delta\sin(2\vartheta_{me}) + L_{dq}\cos(2\vartheta_{me}) \end{bmatrix} \\
\mathbf{C} &= \begin{bmatrix} -\lambda_d\sin(\vartheta_{me}) - \lambda_q\cos(\vartheta_{me}) \\ \lambda_d\cos(\vartheta_{me}) - \lambda_q\sin(\vartheta_{me}) \end{bmatrix}, \qquad L_\Sigma = \frac{L_d + L_q}{2}, \qquad L_\Delta = \frac{L_d - L_q}{2}
\end{aligned} \tag{2.15}$$

In order to simplify the treatise, some additional coefficients able to synthesize these matrices are defined:

$$\begin{aligned}
\mathbf{A} &= \begin{bmatrix} a_{11} & a_{12} \\ a_{21} & a_{22} \end{bmatrix} \\
\mathbf{B} &= \begin{bmatrix} b_{11} & b_{12} \\ b_{21} & b_{22} \end{bmatrix} \\
\mathbf{C} &= \begin{bmatrix} c_1 \\ c_2 \end{bmatrix} \\
\mathbf{A}^{-1} &= \frac{1}{L_d L_q - L_{dq}^2}\begin{bmatrix} a_{22} & a_{21} \\ a_{12} & a_{11} \end{bmatrix} = \begin{bmatrix} \gamma_{11} & \gamma_{12} \\ \gamma_{21} & \gamma_{22} \end{bmatrix}
\end{aligned} \tag{2.16}$$

2.3 *Induction Motors*

IMs are based on the induction torque generation principle, thus some slip between rotor and stator flux vector is required for the generation of the torque. Defining as ω_0 and ω_m the angular speed of the stator rotating field caused by the three-phase voltages given to the windings and the rotor speed, respectively, the slip s is defined as:

$$s = \frac{\omega_0 - \omega_m}{\omega_0} \tag{2.17}$$

The slip frequency between the rotational speed of the stator flux vector and the rotor, some currents are induced in the rotor bars. These in turn generate a rotor flux

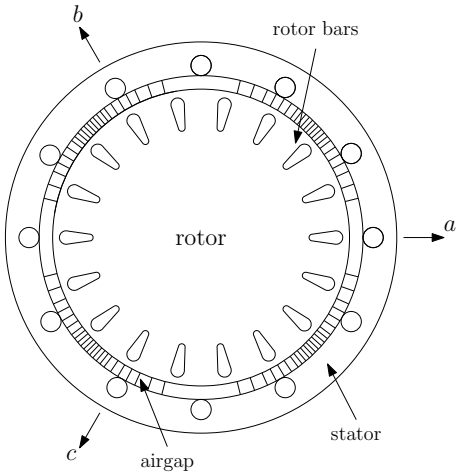

Figure 2.5. Graphical sketch of the structure of a IM.

whose interaction with the stator generates the torque. The necessary presence of the slip brings to classify the IM as an asynchronous motor.

The most diffused rotor structure, and the one considered in this dissertation, is the squirrel cage. In the past, this motor has dominated the electric drives market and only recently is slightly being substituted by its more efficient synchronous counterparts. Its historical large diffusion is due to its robust structure and simple controllability which elect it still the most diffused motor. Nonetheless, due to the fact that some energy is spent to magnetize the rotor, this motor is usually less efficient. A graphical sketch of the cross-section of also this motor is reported in Figure2.5.

The electrical dynamic behaviour of the IM can be described in different coordinate systems. In this thesis the space vector notation is considered also for this motor and a stationary reference frame $\alpha\beta$ fixed to the stator winding is preferred. As a matter of fact, the implementation on a synchronous reference frame would need the knowledge of the rotor flux position. This approach fits for the standard control based on the fundamental synchronous. In the present case, in which the key point is the behaviour of the fault-related harmonics, the synchronous reference frame is useless.

The voltage balance equations for the stator and rotor are the following:

$$\begin{aligned} \mathbf{u}_s &= \mathbf{R}_s \mathbf{i}_s + \frac{d\boldsymbol{\lambda}_s}{dt} \\ \mathbf{0} &= \mathbf{R}_r \mathbf{i}_r + \frac{d\boldsymbol{\lambda}_r}{dt} + \omega_{me} \mathbf{J} \boldsymbol{\lambda}_r \end{aligned} \quad , \quad \mathbf{J} = \begin{bmatrix} 0 & 1 \\ -1 & 0 \end{bmatrix} \tag{2.18}$$

where $\mathbf{u}_s = \left[u_{s\alpha}, u_{s\beta}\right]^T$, $\mathbf{i}_s = \left[i_{s\alpha}, i_{s\beta}\right]^T$, $\boldsymbol{\lambda}_s = \left[\lambda_{s\alpha}, \lambda_{s\beta}\right]^T$ and $\mathbf{R}_s = \text{diag}(R_s)$ are the stator voltages, currents, flux linkages and constant resistance matrix, respectively. The same quantities for the rotor are indicated with symbols $\mathbf{u}_r = \left[u_{r\alpha}, u_{r\beta}\right]^T$, $\mathbf{i}_r = \left[i_{r\alpha}, i_{r\beta}\right]^T$, $\boldsymbol{\lambda}_r = \left[\lambda_{r\alpha}, \lambda_{r\beta}\right]^T$ and $\mathbf{R}_r = \text{diag}(R_r)$, in which the rotor voltages are equal to zero, due to the squirrel cage structure. Also in this case, the electromechanical speed and

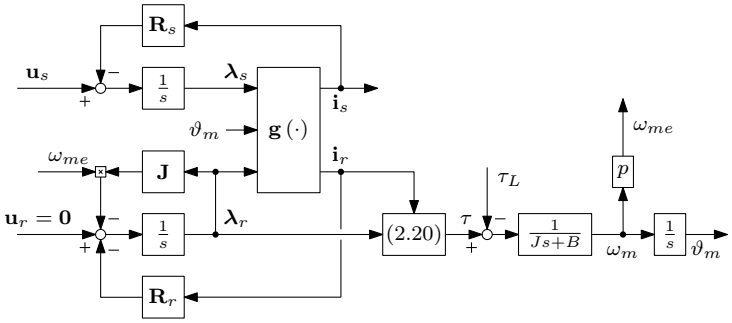

Figure 2.6. Block schematic of the model of an IM in the $\alpha\beta$ reference frame.

position are respectively $\omega_{me} = p\omega_m$ and $\vartheta_{me} = p\vartheta_m$, with p the number of pole pairs of the motor.

The saturation of the iron core is the main cause of non linearity, that becomes even more pronounced in the case of failure, due to the intrinsic asymmetry involved. Therefore, to keep the model as general as possible, the flux linkage vectors $\boldsymbol{\lambda}_s$, $\boldsymbol{\lambda}_r$ are expressed as non linear functions of both current vectors $\mathbf{i}_s$, $\mathbf{i}_r$. Moreover, due to the stationary reference frame, they depend also on the mechanical position.

$$\begin{aligned} &\boldsymbol{\lambda}_s\left(\mathbf{i}_s, \mathbf{i}_r, \vartheta_m\right) \\ &\boldsymbol{\lambda}_r\left(\mathbf{i}_s, \mathbf{i}_r, \vartheta_m\right) \end{aligned} \tag{2.19}$$

To take all that dependencies into account, a general function $\mathbf{g}$ is used:

$$\begin{bmatrix} \boldsymbol{\lambda}_s \\ \boldsymbol{\lambda}_r \end{bmatrix} = \mathbf{g}\left(\begin{bmatrix} \mathbf{i}_s \\ \mathbf{i}_r \\ \vartheta_m \end{bmatrix}\right) \tag{2.20}$$

The electromechanical torque τ generated by the motor can be expressed as

$$\tau = \frac{3}{2} p \left(\lambda_{r\beta} i_{r\alpha} - \lambda_{r\alpha} i_{r\beta}\right) \tag{2.21}$$

while the same mechanical dynamic already used for the PMSM model can be used (2.8). Equations (2.18), (2.21) and (2.8) lead to the graphical representation of the IM model shown in Figure 2.6.

3

PMSM FAULT DETECTION USING STATOR CURRENTS

This chapter is focused on the automatic fault detection of PMSMs. In particular, the aim is the realization of a CNN trained to recognize the health conditions of a PMSM through the elaboration of its steady-state motor currents.

In this context, the algorithm also takes advantages of some improvements typical of the so-called data augmentation techniques, as detailed in Section 3.4.2. Actually, in CNN-based image processing, DA is a mean to increase the available training dataset [74] or to improve the accuracy and robustness of the classifier [30]. DA is an hot and open issue in the industrial predictive maintenance field as the recent literature reports [46, 54, 73]. Its use is commented in Section 3.4.2 in this chapter.

The present thesis includes the condition monitoring of fractional PMSM motors, that is, motors with non-integer number of slots per pole per phase. This is uncommon in the scientific literature, opposite to the use of fractional-slot motors which is an increasing trend in the industrial world due to their specific advantages in both torque ripple minimisation and coils length [21]. Of course, the proposed approach is valid also for integer slot per pole per phase motors.

The chapter also develops a useful "frequency normalization" technique in order to make current patterns less variant with the motor speed. Thanks to this, a very simple network structure is already capable to correctly classify the conditions of a PMSM into the following three categories: healthy, demagnetization fault and interturn fault. Detected faults have a broad degree of seriousness, yielding enhanced prediction capability.

The chapter is organized as follows. Section 3.1 presents the models used for the generation of the training dataset. Each model is explained with particular care on the mathematical formulation and founding hypotheses. The expected current pattern during each fault condition is analysed at steady state, that is the condition in which the proposed condition monitoring operates. Section 3.2 reports the main properties and features of the CNN tool used for the condition monitoring process. The design steps of the network are also reported, for the sake of algorithm repeatability. Section 3.3 illustrates the design of experiments, along with the features of the selected CNN and the highlights on the training dataset.

Experimental results are finally shown and commented in section 3.4, that is split in two parts. The first one reports the validation of the PMSM models, by comparing the simulated output with the experimental one. The models are then used to generate the phase current data patterns for the CNN training. The second part analyses the classification ability of the trained CNN, on real experimental patterns obtained from different PMSM motors, either healthy or with some degree of failure. Conclusive remarks and implementation hints are included.

3.1 *Motor models*

Each motor condition is characterized by a certain current signature. An accurate predictive algorithm is able to early detect a particular fault by recognising its relative signature. This concept may be easily extended to any motor fault. In particular, mechanical defects cause characteristic oscillations in the phase current [81]. By increasing the network complexity and setting new motor models for the generation of the training dataset, the signatures relative to any mechanical fault can be included.

Hereafter, the analysis has been limited to the investigation of some of the possible faults, less prone to be detected by the commonly available techniques (i.e. accelerometers).

In order to generate the dataset of examples for the convolutional neural network training a proper model of each fault is necessary. Since not only the fundamental harmonic of current is of interest but also some spurious ones, the model of the healthy motor should include proper finite element simulations [86]. The same concept is valid for demagnetized motor, while for interturn fault the model proposed in [108] is here adjusted to fit for the fractional-slot PMSM under test.

The choice of the reference frame for the motor models is worth a little deepening. The alternative is between a stationary frame, fixed to the stator, and a synchronous one, fixed to the rotor flux. As regards the healthy and demagnetised motors, the two frames are equivalent, since multiple harmonics of the fundamental have to be considered, so that both models become position-dependent. In case of different motor types, the choice of a synchronous reference frame may help in including magnetic nonlinearity. As regards the interturn fault, the choice of a stationary reference frame yields a constant inductance matrix with respect to the rotor position, opposite to the synchronous frame case. The analysis of different fault severity or locations also comes easily. Anyway, in case of different motors that suffer of saturation, a shift to a synchronous frame would be advantageous for a better matching with FEA methods.

The models selected for the present work are illustrated in detail below.

3.1.1 Healthy motor

For the realization of the healthy motor model equation 2.5 and Figure 2.2 can be used as starting point.

Due to the surface mounted permanent magnet structure, the effect of saturation in motor fluxes is almost negligible. Therefore a linear behaviour of the magnetic paths is assumed and it is described through the (constant) synchronous inductance matrix $\mathbf{L} = diag\{L, L\}$. Conversely, PM flux linkage $\boldsymbol{\lambda}_{dq}^{mg}$ can be affected by local and partial demagnetisation, which creates flux spatial harmonics that finally modify the current harmonic content. A suitable model for the flux linkages spatial distribution can be the following:

$$\boldsymbol{\lambda}_{dq}(\vartheta_m) = \mathbf{L}\mathbf{i}_{dq} + \boldsymbol{\lambda}_{dq}^{mg}(\vartheta_m) \tag{3.1}$$

where ϑ_m is the mechanical rotor position. It is worth noting that the space flux harmonics different from the fundamental one affect both axes.

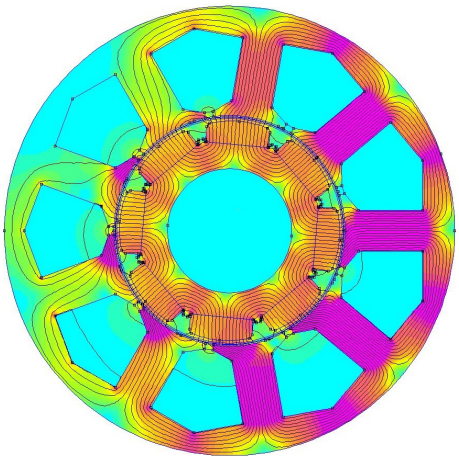

Figure 3.1. Finite element analysis of the healthy PMSM of Table 3.1, when $\vartheta_m = 0^\circ$ and $i_q = 0$ A.

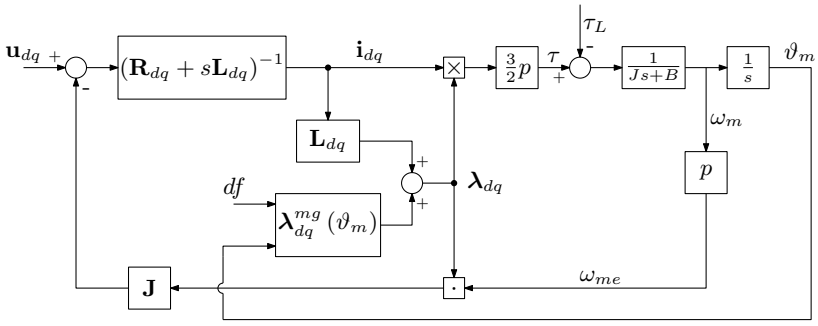

Figure 3.2. Motor model for both healthy and demagnetised cases.

The position-dependent distribution of (3.1) has been derived through a proper FEA, at null stator currents. An example of the flux density across the PMSM under test (Table 3.1) at $\vartheta_m = 0^\circ$ is reported in Figure 3.1.

Since PMs have the same permeability as the air, the FEA model was also used to derive the current-dependent flux linkage, and thus the inductance L, after removing the magnets from the drawing. Several simulations at different current levels have confirmed the linearity hypothesis with respect to the phase current, as stated above.

The complete model of Figure2.2 can be tailored to take into account of position harmonics. It is obtained from equations (2.5)-(3.1) and it is shown in Figure 3.2. The PM flux linkage model obtained by FEA incorporates the dependence on the rotor geometry and it is embedded in the Look-Up Tables (LUT) block $\boldsymbol{\lambda}_{dq}^{mg}(\vartheta_m)$. The same model will also be used for the motor under demagnetisation fault, as explained in the next section. Therefore, inside the block $\boldsymbol{\lambda}_{dq}^{mg}(\vartheta_m)$ there are various LUTs, which differ in the demagnetisation factor df.

In the healthy case, the main component in both the flux linkage and the stator

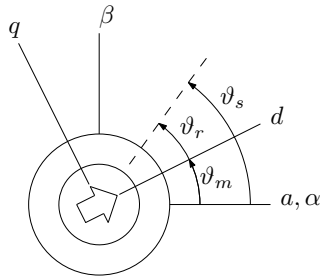

Figure 3.3. Reference frames and angular displacements definition.

current is clearly the fundamental one. But in a real motor, also the 5-th and 7-th flux linkage harmonics have not a negligible effect on the currents [101]. Hence the need to consider those contributions in the current patterns used for the training.

The simulation model of Figure 3.2 was used to run the AC drive in several different working points. For each of them, the q current was stored for future use in the CNN training.

3.1.2 Motor with demagnetisation fault

Overtemperature and exposition to intense external fields can induce either a partial or global irreversible decrease of magnetisation in the PMSM rotor magnets [60]. The macroscopic effect is different in the two cases.

In case of homogeneous demagnetisation, all rotor poles are equally affected, so that the airgap flux density distribution maintains a very similar profile as in the healthy motor. In particular, the electrical behaviour of the motor is still represented by a three-phase balanced system and there is not the evidence of new harmonics eligible as indexes for the fault recognition. In that case the torque per ampere ratio decreases, and a comparison with the brand-new product may help in the fault detection.

More challenging is the case of partial demagnetisation, in which the flux density distribution is no more periodic in the electromechanical angle, that is, it depends on the considered pole pair. The distribution along the airgap is a function of the angular displacement, which can be expressed with respect to either the stationary (ϑ_s) or the synchronous (ϑ_r) reference frame, as depicted with the dashed line in Figure 3.3.

In all generality, the number p of pole pairs of the PMs in the rotor can be different from the number p_w of pole pairs in the windings.

An example with $p = 4$ and $p_w = 2$ is represented in Figure 3.4. The upper graph reports the airgap flux density distribution due to PMs referred to ϑ_r (Figure 3.3). This reference frame with the whole waveform is shifted of ϑ_m with respect to the stationary reference frame fixed to the axis of the winding a.

The lower graph shows the flux linkage of winding a due to the PM. In place of the distributed winding, its equivalent concentrated one is displayed. According to the electric machines theory, the magnetic behaviour is preserved by changing the number of turns according to a winding distribution factor k_w that depends on the constructive features of the winding.

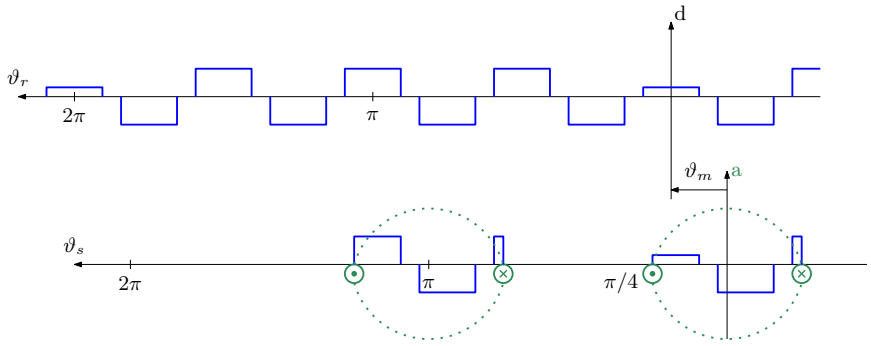

Figure 3.4. An example of the airgap flux density distribution in a PMSM.

The aim of the next passages is to qualitatively obtain the flux linkage harmonics of the phase *a*, in the specific case of partial demagnetisation of the rotor.

If a healthy motor is considered, the airgap flux density is space-periodical, with period 2π in the angular coordinate $p\vartheta_r$. In general, the airgap flux density can be expressed according to the Fourier series expansion.

$$B_g(\vartheta_r) = \sum_{n=1}^{\infty} \left[\hat{B}^c_{g_n} \cos(np\vartheta_r) + \hat{B}^s_{g_n} \sin(np\vartheta_r) \right] \tag{3.2}$$

Due to the symmetrical distribution respect to axis *d*, the coefficients $\hat{B}^s_{g_n}$ are equal to zero and therefore, the second term of the sum can be neglected for each harmonic *n*. According to this, the superscript ^{c} in $\hat{B}^c_{g_n}$ is hereafter removed.

When a partial demagnetization occurs, the distribution (3.2) is modulated by a signal which is space-periodical in the coordinate ϑ_r, becoming:

$$\begin{aligned} B_g(\vartheta_r) &= \left[\sum_{n=1}^{\infty} \hat{B}_{g_n} \cos(np\vartheta_r) \right] \left[\sum_{k=0}^{\infty} \alpha_k \cos(k\vartheta_r) \right] \\ &= \sum_{n=1}^{\infty} \sum_{k=0}^{\infty} \hat{B}_{g_n} \alpha_k \frac{1}{2} \Big[\cos\big((np-k)\vartheta_r\big) - \\ &\cos\big((np+k)\vartheta_r\big) \Big] \end{aligned} \tag{3.3}$$

where α_k is the coefficient that, for each harmonic *k*, represents the impact of demagnetization on the healthy waveform.

The flux linked by a single turn of a coil can be estimated as the integral of the flux density within the area enclosed by the current loop. A sketch of this area in the case of $p_w = 1$ is reported in Figure 3.5. According to that figure the flux linked by one single turn of a coil can be estimated according to the following integral.

$$\lambda_1 = \int_{-\frac{\pi}{2p_w}}^{\frac{\pi}{2p_w}} B_g(\vartheta_s) \frac{DL}{2} d\vartheta_s \tag{3.4}$$

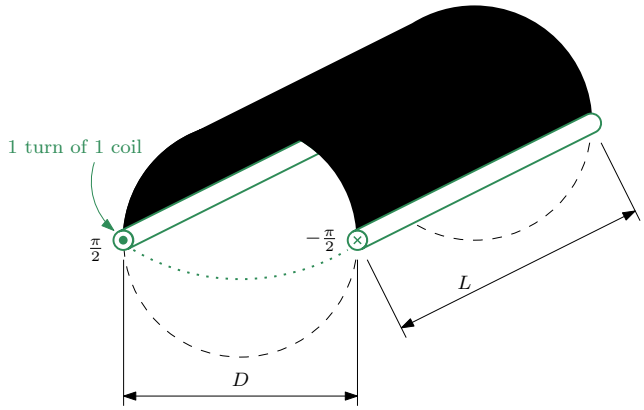

Figure 3.5. A sketch example of the area enclosed by one turn in an electric motor with $p_w = 1$. The area is the grey-coloured one.

Extending the equation to more coils (specifically, p_w coils), and taking into account of the equivalent number of turns for each coil according to the winding factor k_w, the total flux linked by winding a can be expressed as:

$$\lambda_a^{mg} = k_w \sum_{i=0}^{p_w-1} \int_{-\frac{\pi}{2p_w}+\frac{2\pi i}{p_w}}^{\frac{\pi}{2p_w}+\frac{2\pi i}{p_w}} B_g(\vartheta_s)\frac{DL}{2}d\vartheta_s \tag{3.5}$$

with D and L as diameter at the airgap and stack length of the motor, respectively. It is worth noting that the sum with index i is general and makes equation (3.5) applicable for any value that p_w can assume.

Replacing (3.3) and $\vartheta_r = \vartheta_s - \vartheta_m$ into (3.5) gives the following:

$$\begin{aligned}\lambda_a^{mg}(\vartheta_m) = \sum_{i=0}^{p_w-1}\sum_{n=1}^{\infty}\sum_{k=0}^{\infty}\Bigg\{ & k_w\hat{B}_{g_n}\alpha_k\frac{DL}{4}\cdot \\ & \int_{-\frac{\pi}{2p_w}+\frac{2\pi i}{p_w}}^{\frac{\pi}{2p_w}+\frac{2\pi i}{p_w}} \cos\left[(np-k)(\vartheta_s-\vartheta_m)\right] - \\ & \cos\left[(np+k)(\vartheta_s-\vartheta_m)\right]d\vartheta_s\Bigg\}\end{aligned} \tag{3.6}$$

Solving the integrals in (3.6) in the integration variable ϑ_s and repeatedly applying the sum and difference identities gives (see appendix A for a more detailed description

of the mathematical steps):

$$\lambda_a^{mg}(\vartheta_m) = \sum_{i=0}^{p_w-1}\sum_{n=1}^{\infty}\sum_{k=0}^{\infty} k_w \hat{B}_{g_n}\alpha_k \frac{DL}{2}\Bigg\{ \beta_{-k}\left[\cos\left(\frac{2\pi i}{p_w}(np-k)\right)\cos\Big((np-k)\vartheta_m\Big)+ \sin\left(\frac{2\pi i}{p_w}(np-k)\right)\sin\Big((np-k)\vartheta_m\Big)\right]- \beta_{+k}\left[\cos\left(\frac{2\pi i}{p_w}(np+k)\right)\cos\Big((np+k)\vartheta_m\Big)+ \sin\left(\frac{2\pi i}{p_w}(np+k)\right)\sin\Big((np+k)\vartheta_m\Big)\right]\Bigg\} \tag{3.7}$$

where symbols $\beta_{\pm k}$ are defined as

$$\beta_{\pm k} = \frac{1}{np \pm k}\sin\left(\frac{(np \pm k)}{p_w}\frac{\pi}{2}\right). \tag{3.8}$$

First of all, it can be observed that due to the periodicity of the sine function and due to the fact that $np \pm k$ is always an integer, the following term is equal to zero for each choice of the parameters p, p_w, n and k:

$$\sum_{i=0}^{p_w-1}\sin\left(\frac{2\pi i}{p_w}(np \pm k)\right) = 0 \tag{3.9}$$

As a matter of fact this sum is composed by a series of opposing addends. Then, (3.7) can be simplified as

$$\lambda_a^{mg}(\vartheta_m) = \sum_{i=0}^{p_w-1}\sum_{n=1}^{\infty}\sum_{k=0}^{\infty} k_w \hat{B}_{g_n}\alpha_k \frac{DL}{2}\Bigg\{ \beta_{-k}\left[\cos\left(\frac{2\pi i}{p_w}(np-k)\right)\cos\Big((np-k)\vartheta_m\Big)\right]- \beta_{+k}\left[\cos\left(\frac{2\pi i}{p_w}(np+k)\right)\cos\Big((np+k)\vartheta_m\Big)\right]\Bigg\} \tag{3.10}$$

Expression (3.10) is involved. The evaluation of the coefficients that multiply the harmonics is difficult and the uncertainties on the parameters knowledge make useless their estimation. Nonetheless, it is worth appreciating that its particular form makes it possible to infer that for a given couple p, p_w (that is, for each specific motor geometry) only certain harmonics are present in the flux linkage.

Thus, a simplified expression can be taken into account.

$$\lambda_a^{mg}(\vartheta_m) = \sum_{n=1}^{\infty}\sum_{k=0}^{\infty}\lambda_{n,\pm k}^{dm}\cos\left[(np \pm k)\,\vartheta_m\right] \tag{3.11}$$

The flux linkage is so expressed as sum of harmonics at $(np \pm k)\vartheta_m$ scaled by a generic coefficient $\lambda_{n,\pm k}^{dm}$ which should take into account of all the multiplying coefficients in equation (3.10). As mentioned their analytical evaluation is pointless and a numerical estimation is recommended.

The present chapter is relative to the fractional-slot PMSM whose data are reported in Table 3.1. An accurate FEA and the mathematical analysis just described and applied to the considered motor, allows to identify the coefficients of the harmonics present in the stator flux linkage. Among them, the main ones are the fundamental derived from (3.11) by posing $n = 1$, $k = 0$ and the fault-related harmonic, given by $n = 1$, $k = +1$. The amplitude of the main fault-related harmonic, which from now on will be indicated by λ_a^{dm}, is eligible as significant index of the PM health. Due to the winding distribution of the motor with winding pole pairs $p_w = 1$, λ_b^{dm} and λ_c^{dm} have the same distribution but shifted respect to ϑ_m by $2\pi/3$ and $4\pi/3$ respectively.

$$\lambda_a^{dm}(\vartheta_m) = \lambda_{1,1}^{dm} \cos\left[(p+1)\vartheta_m\right] \tag{3.12}$$

Remembering that $p = 4$, one can easily argue that the three-phase system represented by the previous equation leads to a reverse phasor sequence rotating at $-5\vartheta_m$. With respect to a dq synchronous reference frame, the sequence rotates at $-5\vartheta_m - \vartheta_{me} = -9\vartheta_m$. As a result, under demagnetisation fault and at steady-state conditions a i_q current harmonic at $9\omega_m$ is expected.

$$i_q^{dm}(t) = i_{1,1}^{dm} \cos(9\,\omega_m t) \tag{3.13}$$

In case of demagnetisation fault, the model is still described by the equation (2.5) and Figure 3.2. Time by time, the model was updated for different partial demagnetisation levels, by changing the $\boldsymbol{\lambda}_{dq}^{mg}(\vartheta_m)$ LUTs through customised FEA sessions. The modelling of the mechanical part remains unchanged. As in the healthy case, the generation of the CNN training datasets was obtained by changing the motor working points, storing at the same time the i_q current patterns.

3.1.3 Motor with interturn fault

Due to its peculiar mathematical description, the most effective dynamic state-space model of the motor with interturn fault is obtained in the $\alpha\beta$ stationary reference frame. In principle, the present work adopts the modelling technique described by Vaseghi *et al.* in [108]. That method was suited for permanent magnet motors with an integer number of slots per pole and per phase. Here, the method is re-elaborated and extended also to fractional-slot PMSM motors.

The interturn fault is highlighted in Figure 3.6. Each phase is composed by N coils.

For example here it is considered a loss of insulation in the first coil of phase b. The severity of the damage can be graduated by changing the value of the resistance r_f. The fault divides the coil into two parts 1_f and 1_h, characterised by the ratio between the faulty turns and total coil turns $\mu = N_f/N_s$.

The damage causes the phase current to split into two paths. The new path (i_f, Figure 3.6) drains part of the flux-producing current, with a consequent flux linkage reduction.

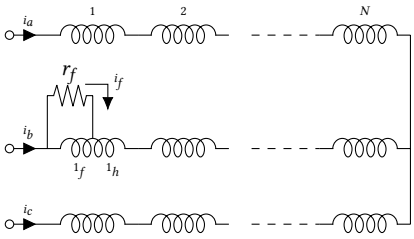

Figure 3.6. Model of N-coil windings with an interturn fault on phase b..

Let R_{coil} be the total coil resistance and $R_f = \mu R_{coil}$ and $R_h = (1-\mu)R_{coil}$ the resistances of the two portions 1_f and 1_h, with currents $i_b - i_f$ and i_b flowing through them, respectively.

Treating the current in each coil (including the two sub-coils generated by the fault) as an independent state variable it is possible to obtain a system of $(3 \cdot N) + 1$ equations that describes the electrical behaviour of the circuit. Then, substituting each current with the correspondent i_a, i_b, or i_c current, adding the voltage Kirchoff law on the closed loop created by r_f and reshuffling the equations, it is possible to obtain a 4-dimensional voltage balance system:

$$\begin{bmatrix} u_a \\ u_b \\ u_c \\ 0 \end{bmatrix} = \mathbf{R}_{abcf} \begin{bmatrix} i_a \\ i_b \\ i_c \\ i_f \end{bmatrix} + \mathbf{L}_{abcf} \frac{d}{dt} \begin{bmatrix} i_a \\ i_b \\ i_c \\ i_f \end{bmatrix} + \begin{bmatrix} e_a \\ e_b \\ e_c \\ -e_f \end{bmatrix} \tag{3.14}$$

where

$$\begin{aligned} \mathbf{R}_{abcf} &= \begin{bmatrix} R & 0 & 0 & 0 \\ 0 & R & 0 & -R_f \\ 0 & 0 & R & 0 \\ 0 & -R_f & 0 & R_f + r_f \end{bmatrix} \\ \mathbf{L}_{abcf} &= \begin{bmatrix} L & M & M & M_{af} \\ M & L & M & M_{bf} \\ M & M & L & M_{cf} \\ M_{af} & M_{bf} & M_{cf} & L_f \end{bmatrix} \end{aligned} \tag{3.15}$$

Symbols u_a, u_b, u_c represent the phase voltages while e_a, e_b, e_c are the back-Electro Motive Forces (b-EMFs). It is worth to note that only a portion $e_f = \mu e_{coil}$ of the total b-EMF e_{coil} is induced in the faulty part $1f$ of the coil itself.

The knowledge of the inductance matrix $\mathbf{L}_{abcf}$ comes from the availability of an accurate FEA, which is an essential requirement of the proposed technique. Inductances L and M are the usual phase stator mutual and self-inductances. The fourth row (or column) contains the mutual and self-inductance between phases and the coil 1_f.

While L and M are easily obtainable, the self- and mutual inductances related to the 1_f coil need to include effect of μ. In details, M_{af} is the mutual inductance between coil 1_f and the entire winding a. Through a FEA it is possible to easily estimate the value of the mutual inductance M_{1a} between coil 1 of the faulty phase (b in this case)

and phase a. This is performed imposing a constant current into the winding a and evaluating the flux linkage on the coil 1 of phase b. Then, knowing that the mutual inductance is proportional with the number of coil turns, M_{af} can be obtained scaling M_{1a} by the factor μ. With the same approach the self-inductance L_f is equal to the self-inductance of coil 1 of phase b weighted by μ^2.

Once the model in the natural $abcf$ coordinates is achieved, the augmented space-vector model in the stationary reference frame $\alpha\beta 0f$ is obtained by an extended version of Park transformation that makes use of the following transformation matrix:

$$\mathbf{T} = \frac{2}{3}\begin{bmatrix} 1 & -\frac{1}{2} & -\frac{1}{2} & 0 \\ 0 & \frac{\sqrt{3}}{2} & -\frac{\sqrt{3}}{2} & 0 \\ \frac{1}{\sqrt{2}} & \frac{1}{\sqrt{2}} & \frac{1}{\sqrt{2}} & 0 \\ 0 & 0 & 0 & \sqrt{\frac{3}{2}} \end{bmatrix} \tag{3.16}$$

where the last element of the matrix is chosen in order to have: $p_{abcf} = 3/2 \cdot p_{\alpha\beta 0f}$. That is the electrical power in $abcf$ reference frame is 3/2 times the power in $\alpha\beta 0f$.

The homopolar component of the current i_0 can be neglected, as it does not contributes to the torque production. The resulting three-dimensional model for the interturn fault is:

$$\mathbf{u}_{\alpha\beta f} = \mathbf{R}_{\alpha\beta f}\mathbf{i}_{\alpha\beta f} + \mathbf{L}_{\alpha\beta f}\frac{d\mathbf{i}_{\alpha\beta f}}{dt} + \mathbf{e}_{\alpha\beta f} \tag{3.17}$$

and it is shown in Figure 3.7. The effect of spatial harmonics is included in the model thanks to a LUT block ($\mathbf{e}^N_{abcf}$) obtained experimentally. In particular, the three phase induced voltages are measured as function of the rotor position ϑ_m and normalized with respect to ω_{me}. The fourth dimension of vector $\mathbf{e}^N_{abcf}$ is estimated as a portion (μ) of the voltage induced in the faulty phase e_b.

The electromagnetic torque is estimated by an energy balance of the augmented motor model (3.17):

$$\tau = \frac{3}{2}\frac{e_\alpha i_\alpha + e_\beta i_\beta - e_f i_f}{\omega_m} \tag{3.18}$$

in which the sign minus in $e_f i_f$ is due to the particular definition of e_f in the model, according to equation (3.14).

Finally, it is appropriate a consideration about the expected current patterns in case of interturn fault. In normal conditions the spectrum of the current vector is formed by the fundamental signal rotating at $p\omega_m$ and its multiple harmonics. Considering the Fourier Series in amplitude and phase form one can express the currents as follows.

$$i_a(p\omega_m) = \sum_{n=1}^{\infty} i_n \cos(np\,\omega_m + \cancel{\varphi_n}) \tag{3.19}$$

As for the healthy and demagnetized cases, the phase of each harmonic is present but neglected in the analysis since it has no significance in this context.

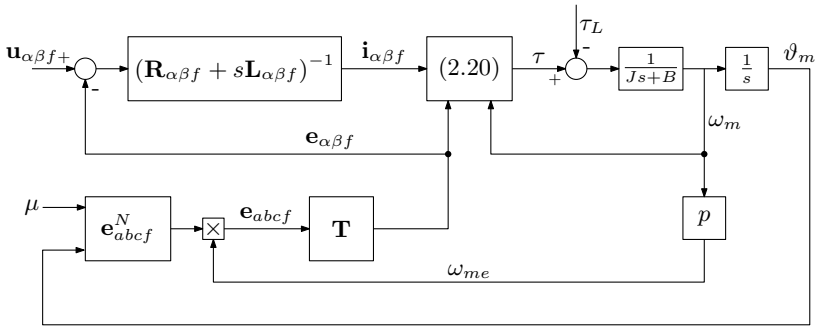

Figure 3.7. Motor model for the interturn fault case.

Multiples of the third harmonic are null due to the hypothesis of a three-phase balanced system. Clearly, when an interturn fault occurs the system balance is lost and the third harmonic and its multiples may appear in the current signal. This was also verified by simulation, from which it has been deduced that the major fault-related contribution is actually due to the third harmonic. It generates a positive phasor sequence in the three-phase system, which in turn generates an i_q current oscillation at $2p\omega_m$ that can be profitably used as healthy index:

$$i_q^{it}(t) = i_1^{it} \cos(2p\,\omega_m t) \tag{3.20}$$

The i_q current was obtained under different interturn fault hypotheses (i.e. different values of μ) from the $i_{\alpha\beta}$ current of the model represented in Figure 3.7, through the inverse of transformation (3.16). Then, the current patterns were stored for next use in the CNN training procedure.

3.2 *Convolutional neural networks*

This section reports the fundamentals of convolutional neural networks, whose properties and design issues will facilitate the understanding of the following paragraphs.

CNNs are a type of AI-based algorithm that are inspired by the behaviour of mammalian visual cortex [47, 115]. In particular, their principal similarity is in the procedure called feature extraction, which is the recognition of more or less complex characteristics that are present inside the image. This operation is performed by applying several filters, called kernels, through different layers in cascade. Such structure allows the recognition of characteristics that are as complex as the number of layers increases. This set of layers forms the convolutional stage of the CNN.

Other common layers in CNNs are then briefly described. For an example of their utilization inside a CNN see Figure 3.8 which is the CNN that has been used within this chapter.

The next layer after the convolution is nonlinearity, that can be used to adjust or cut-off the generated output. For many years, sigmoid and tanh were the most popular non-linearity. More recently, the Rectifier Linear Unit (ReLU) has been used

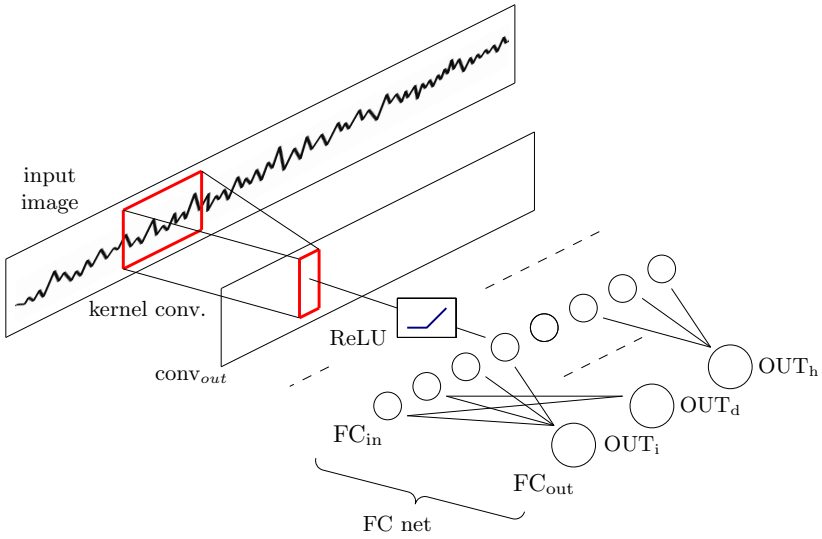

Figure 3.8. Example of a 1D convolutional neural network.

more often, for its simpler definitions in both function and gradient [3]. It implements the following function:

$$y = \begin{cases} x & \text{if} \quad x \geq 0 \\ 0 & \text{otherwise} \end{cases} \tag{3.21}$$

The nonlinear layer helps in training and fitting nonlinear behaviours. Finally, a classical Fully Connected (FC) net layer is used to classify the image among the possible output classes .

Generally, in image recognition a 2D discrete convolution is used. It is applied between the input image I and a kernel K characterized by a certain receptive field (i.e. height m and width n) which is typically smaller than the dimensions of the image. The output is often called *feature map*. The operational definition of the convolution may vary, depending on whether or not it is of interest to maintain the commutative property [36]. In this work, the convolution $S = K * I$ has been implemented as follows:

$$S(i,j) = \sum_m \sum_n I(i-1+m, j-1+n)K(m,n) + b \tag{3.22}$$

where it is intended that the matrix indices start from 1. The algorithm may also be defined as a *cross-correlation*, which is identical to a standard convolution, without flipping the kernel [36]. An example, reported in Figure 3.9, will help in understanding the procedure.

Firstly, an element-by-element (Hadamard) product between a sub-matrix of the input image and the kernel is performed. The portion of the input matrix that must be considered is identified by the indexes (i, j). In Figure 3.9, the computation of $S(1, 1)$ is obtained by the Hadamard product of a 3×3 kernel matrix and sub-matrix of the

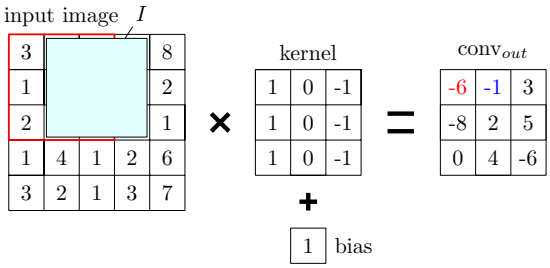

Figure 3.9. A convolution example. In case of 1D CNN, heights of input image, kernel and convolution output (conv_{out}) are unitary.

same size located in the upper-left corner of I. The products (i.e. the elements of the Hadamard matrix) are summed together with a bias b, generating a value for $S(1,1)$ element. To compute $S(1,2)$, one has to refer to the sub-matrix I highlighted in blue in Figure 3.9, and so forth.

3.2.1 Convolutional neural networks properties

Due to convolution, three are the main properties of a CNN that a normal fully connected neural network does not have: sparse interactions, parameter sharing and equivariance to translations. Sparse interactions and parameter sharing are properties which are reciprocally highly connected. Since the kernel dimension is generally smaller than the input image, the same weights (i.e. the elements of the kernel) are applied on different portion of the image. Therefore, the same parameters are shared among the neurons of the each layer, justifying the *sparse interaction* quality.

Opposite to traditional neural networks, that are fully connected, in CNNs the reduced kernel dimensions enable both a lower storage capability and a lighter computational load.

Finally, *equivariance* of a function means that if the input changes, the output changes too, accordingly. The property of *equivalence to the translation* of a CNN network means that if the input image is shifted in time, so will the output. Having in mind the pattern recognition problem, the equivariance is definitely useful, since the position of the fault within the input image is unknown.

3.2.2 Convolutional neural networks parameters

The design of a CNN is a very complex task, with a huge number of possibilities and parameters. This is the main concern when approaching the use of this powerful, but rather challenging analysis tool. In the following paragraphs some hints will be given in order to guide the designer in the choice, with specific reference to the condition monitoring problem.

The definition of a CNN requires many different parameters, which can be subdivided into hyperparameters and learnable parameters.

The formers define the architecture of the network. Some examples are the number

or type of layers that compose the CNN, the number of filters in each convolutional layer or the number of neurons in the filters.

The learnable parameters are the weights and biases of each neuron of the CNN. They are chosen after that the CNN structure is designed through the definition of all the hyperparameters.

The design of the CNN does not necessarily follow that order. In the present chapter it has been found that a procedure that goes back and forth between the hyperparameters and the learnable ones may be the most suited way to come to satisfactory results. In the following, some details are given.

Learnable parameters

The training procedure defines the weights and biases inside the network. This problem is faced within a very powerful class of methods that are known as *supervised* learning techniques. A labelled training dataset is necessary, that is, a set of images to feed the network and that it tries to classify.

If the network performs its task properly, i.e. the CNN classifies the images as their are labelled, the weights are correctly tuned. If not, an optimization method to update them is necessary.

A typical choice falls in the back-propagation error-based techniques in which the target is the minimisation of a given *loss function*, which is evaluated at each iteration of the training dataset (*epoch*) by comparing the known (labelled) fault conditions with the ones predicted by the CNN.

A commonly used method is the Stochastic Gradient Descendent (SGD) algorithm [92]. This method is particularly known for its simplicity in the implementation and for its optimality in the convergence rate, equal to $\mathcal{O}(1/T)$. This parameter is the expected excess cost of the approximated solution respect to the optimal one after T optimization iterations.

With this method, once the loss on the training dataset is calculated, weights are updated by a small step in the direction of negative gradient of the loss itself. The dimension of the step is imposed by the *learning factor* coefficient, which governs the convergence speed. An upper limit to the learning factor is given by the possible triggering of oscillations of the loss function around its minimum, without reaching it. A deeper analysis of SGD is done in [103] or still in [36].

It is of paramount importance that the training dataset covers the whole space of images that the network is asked to classify. When the CNN is trained on a very small subset, it will perform well only locally, since it has not a good extrapolation ability.

Hyperparameters

The focus moves now on the design of the CNN structure, i.e. the definition of the hyperparameters. A typical AI-related problem is the *overfitting* issue.

Overfitting is a situation such that the neural network is so closely fitted to the training set that it finds difficult to generalize the problem and make correct predictions for new data. This is directly related to the neural network model capacity, which defines the complexity of the tasks that a neural network is able to solve. The more

well-structured the CNN, the larger its model capacity. On the other hand, if the CNN has a too big model capacity, it may tends to overfit training data and will be unable to elaborate new data.

The opposite condition, the *underfitting*, is also a problem. In that case, the model capacity is insufficient and the CNN does not track the real trend of training data. It tends to interpolate the experimental data by a too simple model and some crucial information are lost.

In the present work, it has been found that an iterative procedure can help in defining all the hyperparameters of the CNN. The training procedure is started with a CNN of minimum model capacity. The training set obtained by the drive models is splitted into two datasets (*cross-validation* method). The first is used for the training by the SGD algorithm. After each training epoch the SGD evaluates the loss function to decide whether to reiterate the training by starting a new epoch or to stop it. The end of the training can happen because the loss function has either reached a predetermined minimum value, or it has not improved during the last epochs.

The second dataset, called *validation set* is used to check the CNN during the training outlined above, at regular intervals. The loss function is evaluated but (opposite to the training procedure) the check is not intended to modify the weights of the CNN. It just interrupts the training flow, verifying the ability of the network to recognise a dataset (i.e. a motor fault) that it has never seen before. At the end, the time evolution of the loss function of both the training and validation during the SGD training yields three possible situations:

- *overfitting*: the training accuracy is satisfactory, but the validation test on new images still returns a poor result. The CNN has to be simplified, for example reducing the number of layers.
- *underfitting*: both the training and validation still exhibit low accuracy. The CNN model capacity is too small and it shall be increased by either adding layers, increasing kernel sizes or making other decisions that lead to a more complex structure. Iteratively, the architecture of the CNN will become more and more structured till it edges an overfitting flaw.
- *well-tuned*: the predetermined overall accuracy (for example, 97% of positive matches) is reached and the validation test on new images returns a good result as well. The CNN is sized appropriately and the weights are well tuned. The training procedure has been successful.

The procedure outlined above was used to design the CNN that underlies the present condition monitoring technique. Even not revolutionary, still it represents an operative and effective way for the implementation. The various steps are summarised in Figure 3.10, while the CNN specific features are reported in section 3.2.2.

3.3 *Design of the experiment*

This section analyses the design and execution of experiments for the proposed condition monitoring of a fractional-slot permanent magnet synchronous motor. It is subdivided into a part related to the validation of the models necessary for the generation of the artificial training dataset and a part relative to the CNN design.

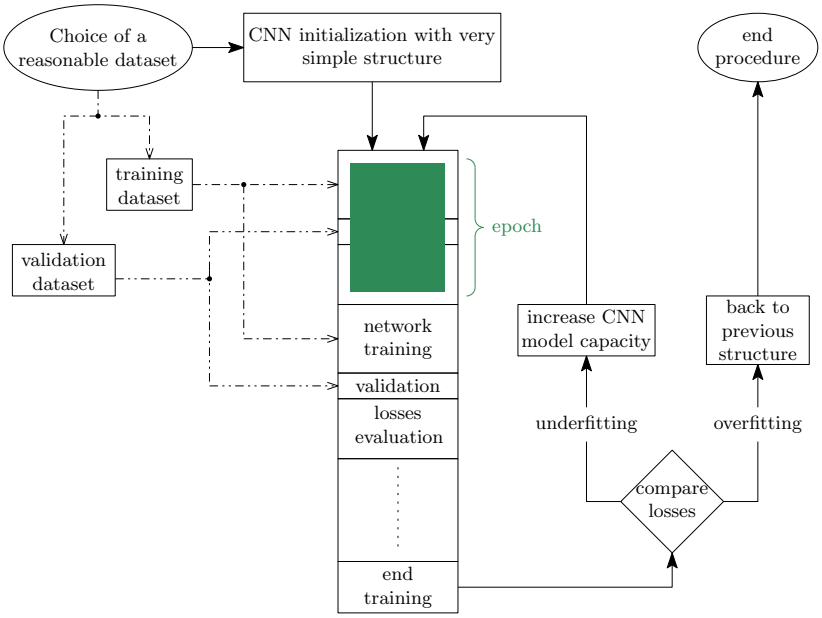

Figure 3.10. Proposed iterative design of CNN for condition monitoring.

3.3.1 Permanent magnet synchronous motor drive models validation

One of the main innovation proposed in this thesis is the combined use of motor models and CNN to get a comprehensive approach to condition monitoring. The motor models need to be validated before being used as generators of artificial dataset for the CNN training. The availability of a virtual unlimited dataset greatly enhance the industrial feasibility of the method, with respect to those based on the collection a great number of real faulty motors.

The validation of the models presented in the previous sections was achieved by comparing their behaviours with a real PMSM. It was a 1.5 kW PMSM whose main features are reported in Table 3.1.

In order to validate the models under different loading conditions, the PMSM was stiffly coupled and dragged at constant speed ω_m^* by a Dragging Motor (DM). The whole test bench is shown in Figure 3.11.

Actually, two prototypes of the same motor were manufactured with customised features. The first one was an healthy motor with a modified winding. According to the modelling of section 3.1.3, a contact has been extracted from an intermediate point of the phase *b*. In this way, it was possible to insert an external variable resistance to simulate interturn faults of different severity. The absence of the resistance was the healthy motor, of course.

The second motor was used for the validation of the condition monitoring in case of demagnetisation. The rotor was modified removing the permanent magnets of a pole pair and replacing them with demagnetised elements, namely with the 20 % of

Table 3.1. Healthy PMSM nameplate data.

Stator pole pairs (p_w)	1
Rotor pole pairs (p)	4
Nominal current (I_N)	3.8 A
Nominal speed ($\Omega_{m,N}$)	576 rad/s (5500 rpm)
Nominal torque (T_N)	2.6 N m
Stator resistance (R)	1.6 Ω
Phase inductance (L)	9.15 mH
DC link voltage	540 V
PWM switching frequency	10 kHz

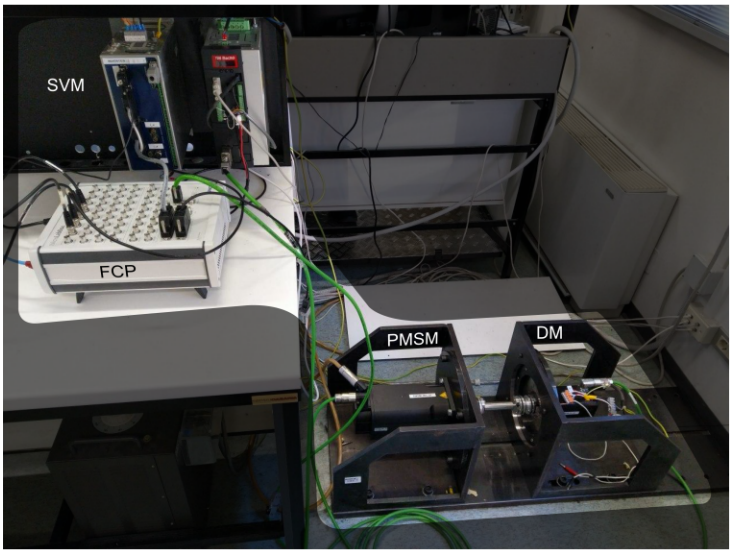

Figure 3.11. Experimental laboratory setup.

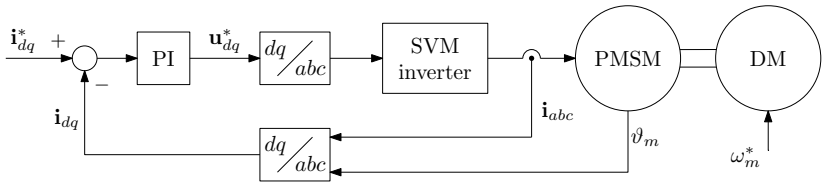

Figure 3.12. Experimental current-controlled PMSM drive.

nominal remanence.

The experimental setup was completed by two Space Vector Modulation (SVM) inverters connected to the motors and controlled by a Fast Control Prototype (FCP) system (Figure 3.11), implementing the conventional field oriented control (Figure 3.12).

The phase motor currents are of fundamental importance for the condition monitoring proposed in this work. They were directly measured through the MicroLabBox Analog to Digital Converters (ADCs), with a resolution of 16 bit for a full scale current of ±14A. The inverter switching frequency and the ADC sampling frequency were both of 10 kHz. The drives were operated at different speed and load conditions and the real currents were compared with those obtained by the Simulink models, for validation purposes.

The validation has involved both healthy and faulty motors and the related models. The first point to resolve was whether a frequency or time comparison was more appropriate. The former is a well-defined method, even if it involves the burden of a transformation in the frequency domain. It can be the best candidate in case you want to automate the validation procedure. The second enables a qualitative analysis of the trend of the signals over time. It is convenient because it provides at a glance information on the quality of the model. Although the validation was performed on different working conditions, only one per type of fault is here reported, for illustrative purposes.

As described in section 3.1, an incoming fault is characterised by the emergence of new (fault) harmonics in the current spectrum. For what concerns the qualitative validation in the time domain, Figure 3.13 shows the i_q current in healthy conditions, at a speed of 104.7 rad/s and a load torque of about 0.5 Nm, corresponding to a current $i_q = 1$ A.

The same working point was selected for the demagnetised PMSM and the interturn fault. The results of the comparisons are analysed in Figure 3.14 and Figure 3.15, respectively. It is worth to note how the demagnetisation of a single magnetic pole pair (out of 4) causes a marked oscillation at the frequency $9\omega_m/2\pi = 150$ Hz, as required by (3.13).

It is also evident that the interturn fault gives rise to an oscillation, due to the phase unbalance. Its period is of about 7.5 ms, as expected from (3.20) that indicates a frequency of $2p\omega_m/2\pi = 133.3$ Hz.

All figures also track the percentage error in the i_q current between model and experiments, referred to the nominal motor current (3.8 A_{eff}, Table 3.1). In all cases the errors lie within the satisfactory range of ±1 %.

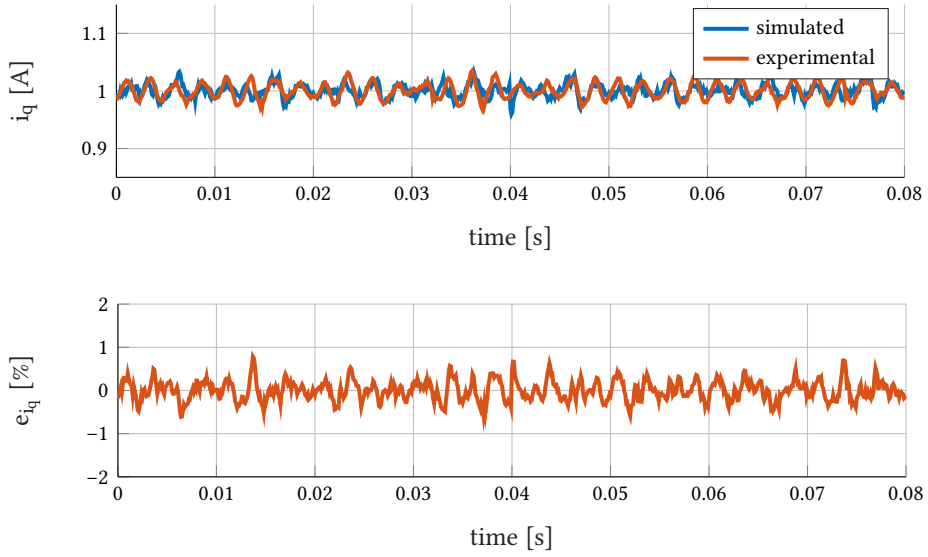

Figure 3.13. Model and experimental i_q current time patterns, healthy PMSM. The percentage error is referred to the nominal motor current.

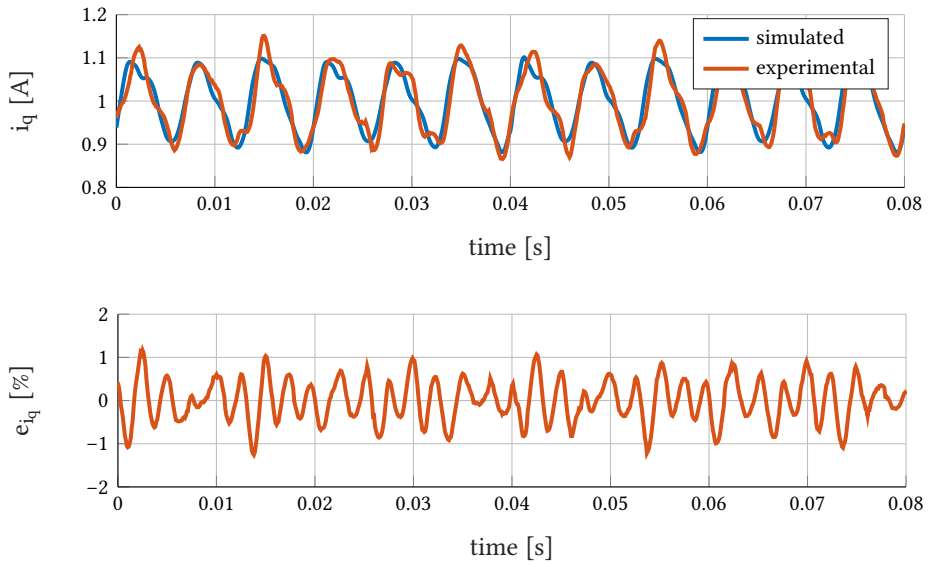

Figure 3.14. Model and experimental i_q current time patterns, partially demagnetised PMSM. The percentage error is referred to the nominal motor current.

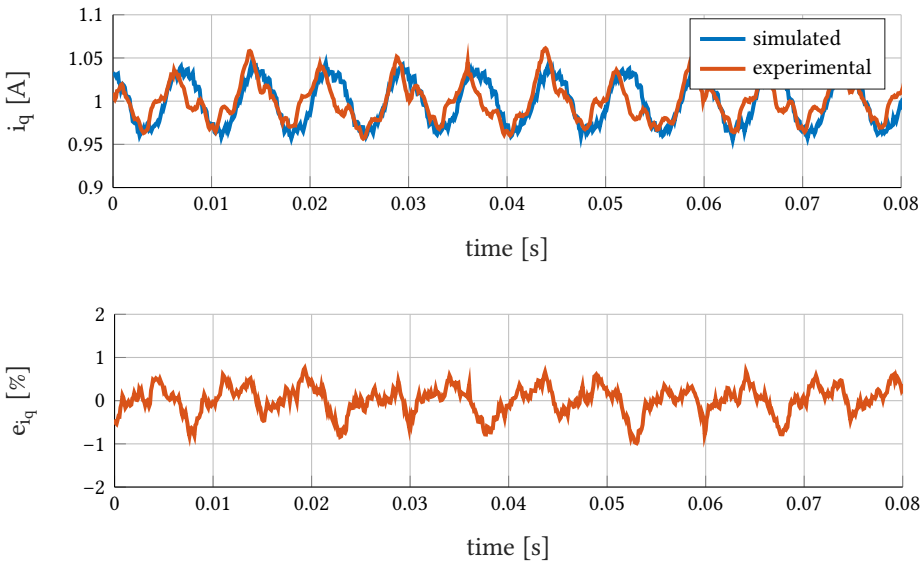

Figure 3.15. Model and experimental i_q current time patterns, interturn fault. The percentage error is referred to the nominal motor current.

For what concerns the validation in frequency domain, Table 3.2 shows the comparison between the amplitudes of both the fundamental current components and fault harmonics, in case of simulation models (sim) and of experimental prototypes (exp). The percentage errors (err) are referred to the PMSM nominal current (Table 3.1). All data refer to the same working conditions described in Figure 3.13-Figure 3.15. It is easy to note the impressive similarity of the results, which confirms the accurate FEA of the motor. The strong correspondence between models and real prototypes will yield a trustworthy generation of artificial patterns for the CNN training, which is one of the key-features of my thesis work.

Table 3.2. Model validation through Fast Fourier Transform (FFT) analysis of the i_q current.

		sim [A]	exp [A]	err [%]
healthy	fundamental	1	0.999	0.018
	fault harmonic (absent)	-	-	-
demagnetized	fundamental	0.9997	1	-0.0055
	fault harmonic (@ 150 Hz)	0.108	0.102	0.111
interturn	fundamental	0.964	0.972	-0.141
	fault harmonic (@ 33.3 Hz)	0.039	0,038	0.025

3.3.2 Convolutional neural network design hints

The CNN was designed by adopting the approach explained in section 3.2. To make it easier to reproduce the conditioning monitoring system, some design hints are reported below.

Since the system is operating on current patterns, a 1D neural network was realized. The only one dimension is the q current record length that will be indicated with letter M.

At steady state, an healthy PMSM should exhibit a constant q current. As highlighted during the model validation stage, either a partial demagnetisation or an interturn fault cause oscillations to arise, because of harmonics at frequency different from the fundamental one.

It is expected that more severe is the fault level, the greater the amplitude of oscillations, while its angular frequency should identify the type of fault. The angular frequency is strictly dependent on the motor speed and this eases the evaluation of the right fault-related harmonics. In principle, a proper threshold on the oscillation amplitude could then implement a good condition monitoring. This apparently simple method has some implementation flaws, as the need of establishing the threshold and facing possible slight frequency shifts of the selected harmonic.

The use of a well-tuned convolutional neural network is definitely preferable, as it takes the index in the recognition process not only a specific harmonic but the current time behaviour as a whole. The classification of the motor conditions will be more robust and successful.

Choice of kernel and current record sizes

The condition monitoring is based on the analysis of i_q current time strings, each of them composed by M points, usually sampled at the beginning of every inverter switching period $T_c = 100\,\mu$s. The mean value associated to the operating point of the motor is out of interest, and it is removed. After data post-processing, an healthy motor should return current patterns just noisy around zero. A first important choice is about the kernel size (or length) (Figure 3.9), that is the time period by which the i_q current record is scanned by convolution. The following considerations provide some hints in the trade-off.

The oscillations due to the demagnetisation and interturn faults have a time period established by equations (3.13) and (3.20) and it is a function of the motor speed.

The kernel elements are the CNN weights that after the training will approximatively have a sinusoidal shape, at the fault-related harmonic frequency. Therefore, the minimum kernel length M_{min} that may guarantee the detection needs to includes at least one period of oscillation in the worst conditions, i.e. at the minimum motor speed ω_{min} and in presence of an interturn fault:

$$M_{min} \geq \frac{\pi}{p\,\omega_{min}\,T_c} \tag{3.23}$$

A longer kernel would contain more than one period of oscillation, with a detection capability preserved and even improved, at the cost of a longer processing time. A

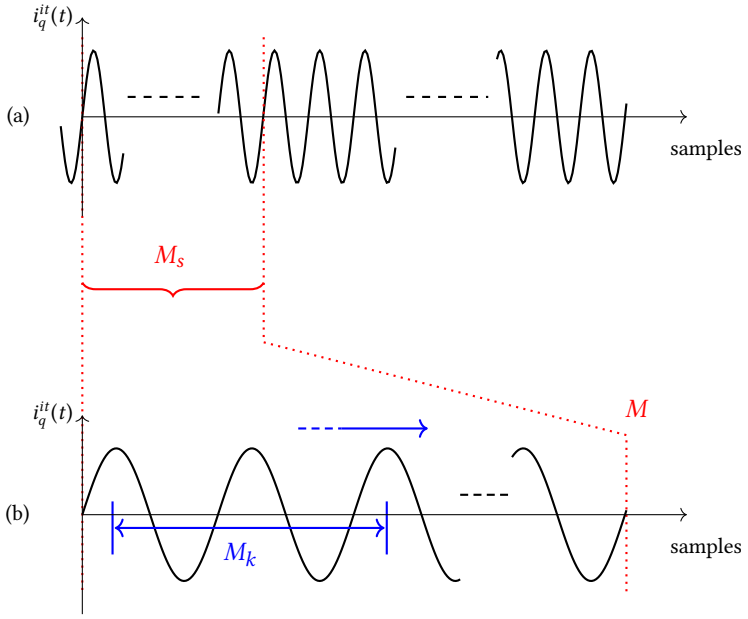

Figure 3.16. Frequency normalization for kernel matching. The graphs are two i_q current records, (a) @ $\omega_m > \omega_{min}$, (b) @ ω_{min}. After normalisation, M_s samples contain the same number of oscillations of M samples @ ω_{min}.

rough, but effective, rule of thumb is to set $M_k \approx 2M_{min}$, while the length of each i_q current record was set to $M \approx 25M_{min}$.

It is worth to note that a certain independence between the fault-related harmonic period and the kernel length enables the use of the same kernel for both the monitored faults, without increasing the depth of the CNN.

The technique is based on the effects of the faults into the airgap flux density, which in turn affects the b-EMF and finally the current patterns. The effect is less evident at low speed and therefore below a certain minimum speed the algorithm cannot work. It has been found that a proper choice for the PMSM prototypes used during the experiments is to trigger the operation of the condition monitoring algorithm above the minimum operating speed $\omega_{min} = 42$ rad/s $= 400$ rpm, less than $0.1 \cdot \Omega_{m,N}$. In turn, that choice leads to a minimum kernel length $M_{min} = 187$, $M_k = 300$ and $M = 5000$, according to (3.23) and the related discussion.

Frequency normalization

For the sake of an easier implementation in the real drive, the i_q current time records always contain the same number M of samples. As the speed increases, more and more oscillation periods are present, as depicted in Figure 3.16, upper track. This is a big issue, since the kernel size and weights cannot be changed in real time.

When the PMSM runs at the minimum speed ω_{min}, by construction M_{min} samples correspond to a whole period of oscillation and each i_q current record, composed by M elements contains $M/M_{min} = 25$ whole oscillation periods. This is a design feature that must be preserved in any working condition. As the motor accelerates to a speed ω_m, the i_q records more than 25 periods, so it must be scaled down by taking only the first M_s samples, calculated proportionally as

$$M_s = M \frac{\omega_{min}}{\omega_m} \tag{3.24}$$

so that the number of oscillations is still 25 at any speed and the effectiveness of the convolution is maintained.

3.4 *Experimental results*

As it is evident from the previous sections, the road to a complete algorithm is a complex interweaving of interdisciplinary skills, ranging from the physics of electric motors to the design of appropriate neural networks.

Each phase involved theoretical studies, simulations and experimental sessions. Therefore, this section is entitled Experimental Results in the sense that it will show CNN's actual classification capabilities on PMSM propotypes that in no way took part to its training. First, some further implementation details are given below.

3.4.1 Convolutional neural network implementation details

The convolutional neural network was implemented in Matlab through the Neural Network Toolbox. The training requires the design of an artificial dataset, composed by i_q current records (*images*) obtained from the models validated above. Training samples among the three classes (healthy, demagnetized and motor with interturn fault) have to span the whole motor operating region in terms of both current and speed. Records are randomly mixed to compose epochs, as described in section 3.2.2. Once the kernel length M_k is fixed, it can be applied along each current pattern, for all the patterns of the epoch.

The convolutional network structure depicted in Figure 3.8 ends with a classification among healthy and two faulty conditions. In details, the CNN returns a real number for each neuron of the FC output layer. Namely, OUT_h for the healthy motor class, OUT_d and OUT_i) for the demagnetised and interturn fault classes, respectively. Them alone are insufficient for a proper final decision on the PMSM state.

Another layer, called *softmax*, translates the neurons output in a percentage. Then, the label C of the class which has the higher probability to include the given i_q time record is computed by the simple expression:

$$C = \max_x \left[\frac{\mathrm{OUT}_x}{\sum_x \mathrm{OUT}_x} \right]; \qquad x = \{h, d, i\}. \tag{3.25}$$

By comparing C returned by (3.25) with the known state of the PMSM that has produced the current record, the training algorithm iteratively tunes the elements of the kernel as well as the weights of the FC net, as already described in Figure 3.10.

In the training dataset generation process, speed was imposed at different levels starting from ω_{min} = 42 rad/s at steps of 20 rad/s up to $\Omega_{m,N}$ = 576 rad/s, while the i_q current was controlled by steps of 0.5 A up to I_N = 3.8 A_{eff}.

Several demagnetization levels were included in the training set, generating samples with PMs at 20 %, 40 % and 60 % of nominal remanence. Interturn fault samples were achieved at the following different levels of the fault resistance r_f: 0.01 Ω, 0.1 Ω, 1 Ω.

The artificial training dataset (14700 current vectors, of M samples each) was divided randomly into two subsets: the first, composed by the 70 % of the original dataset, was used for the training, while the remaining samples were used for the validation of the neural network (Figure 3.10). Thus, $0.7 \cdot 14700 = 10290$ samples were used in each epoch for the update of the network weights.

3.4.2 Data augmentation techniques

The data augmentation is the artificial generation of training patterns to enlarge the training dataset and obtain better tuned networks. Actually, in the present case, the whole training set is created artificially through the simulation model and therefore, also this operation can be classified within the data augmentation methods. The application of this approach gives wide possibilities for the generation of several training patterns in different working conditions of the motor. Nonetheless, as it will be appreciate in the following, the implementation of additional data augmentation methods is mandatory to reach satisfactory results.

A recent review [112] has collected the main time series DA methods, framing them in an accurate taxonomy. All methods have the goal of increasing the number of training samples.

The most challenging ones are the decomposition, the learning methods and finally the model-based methods. The formers decompose the initial training dataset in a series of statistical informations as trend, seasonality and residuals. Then they apply some transformations to these variables creating the augmented training dataset. While interesting, they are probably too complex for using in the present work. Learning-based methods assume that simple transformations applied to encoded inputs rather than to the raw inputs would produce effective DA [112]. They represent a viable improvement and are worth a future deepening.

Last, model-based time series augmentation approaches typically involve modelling the dynamics of the time series with statistical models. The present implementation borrows some DA techniques, namely white noise addition and random cropping, always with an eye to maintain the necessary overall simplicity. They have been applied to both simulation and experimental current patterns, as described below.

Firstly, a white noise was added to the i_q patterns obtained by the models, obtaining new patterns and therefore enlarging the artificial dataset.

Secondly, special attention was paid to the phase of the artificial faulty patterns. Since they are generated by a model, it is easy to make the mistake of polarising them with unrealistic conditions. This is particularly true for the initial conditions of the simulation that, if unchanged, may lead to faulty current patterns with always the same initial phase of the harmonics. It has been found that a good solution is to

generate quite long current patterns and then obtain several artificial sequences by randomly cropping M-samples portions.

The same cropping technique was used to triple the experimental dataset used to validate the classification capabilities of the CNN in Section 3.4.3.

3.4.3 Convolutional neural network classification capabilities

The classification capabilities of the condition monitoring system were finally validated through an experimental set of samples collected on the custom real motors available in the laboratory. None of the sets was used in the training of the CNN.

A set of 144 current vectors was obtained in different working conditions. In details, the experiment grid was obtained by regularly spacing the speed in the interval $[1/10 \dots 1\ \Omega_{m,N}]$ and the i_q current within $[0.2 \dots 1\ I_N]$. As regards the interturn fault, fault resistances were selected in the range $[1 \dots 15\Omega]$. They were finally presented to the proposed condition monitoring system for classification in order to test its performances.

To evaluate the impact of the DA techniques to the network classification accuracy, they were applied one after the other for the generation of the training dataset. After each improvement, the CNN was asked to classify the same experimental dataset.

As common practice in supervised learning algorithms, the results are reported in a so-called *confusion matrix*, a specific table layout (Figure 3.17) that allows the evaluation of performances at a glance. Each column of the matrix represents the instances in a predicted class while each row represents the instances in an actual class.

In the first case (Figure 3.17 (a)) neither noise addition (except quantization noise) nor random cropping were applied for the generation of each sample of the training dataset. Each sample pattern started from the same initial condition. In this case the classification results are very poor and the network is able to classify correctly only the 59.7% of the experimental motor conditions.

Some improvements were achieved by adding a white noise to the current patterns used to train the CNN (Figure 3.17 (b)), increasing the net accuracy up to 66.67%. The performance is still non-optimal because in this way the same initial phase is always imposed on the harmonics (Section 3.4.2), a condition that is obviously not respected by the experimental data.

The classifier accuracy was further increased by random M-samples cropping within each simulation sample. This improvement in the training dataset produced the classification reported in Figure 3.17. In this case the recognition is perfect and all cases are correctly classified (Figure 3.17 (c)), confirming the validity of both the method and the proposed DA hints.

Last, the experimental batch was enlarged by adding 9 further measurements at very low speed (26.2 rad/s), below the speed of 42 rad/s fixed as lower limit during the system design (section 3.3.2). Such new measurements were accomplished in the interturn fault case with r_f varying between $[0.025\,\Omega \dots 0.1\,\Omega]$ with $i_q = 1$ A.

This new test was intended to validate the recognition problems at low speeds of the motor. Even increasing the severity of the fault by strongly reducing the fault

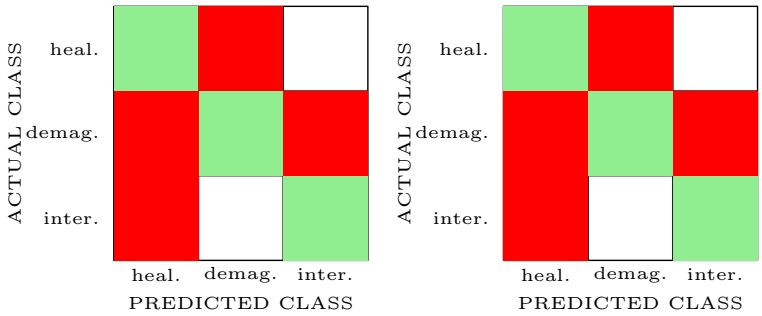

(a) No data augmentation.

(b) With white noise.

(c) WN and random cropping.

(d) With 9 samples out of range.

Figure 3.17. Experimental confusion matrices. Classification results are listed by gradually including different DA techniques to the training dataset. The rightmost matrix includes 9 experimental patterns out of the CNN training range.

resistance r_f, the reduced rotor speed leads to some false positive predictions. In particular, the CNN correctly classifies only 3 current patterns over 9 (Figure 3.17 (d)).

Finally, it is worth remembering that the study has been conducted considering a torque controlled PMSM (the speed was imposed by the load), but the technique is general and can be applied also to speed-controlled motors provided that they are in steady-state conditions. In this case the only difference is that the current reference is not constant but generated by the speed controller and so an additional background noise due to the speed control loop can be present. In order to properly manage this issue the training dataset should be composed by patterns including also this noise, enabling the network to learn it and to distinguish it from the fault-related harmonics.

3.5 *Conclusive remarks*

An effective method for condition monitoring of PMSM has been presented in this chapter. As the following chapters, it falls into the category of knowledge-based systems, matching the *more-intelligent drives* paradigm.

The proposed condition monitoring technique is composed of two parts. The first one, performed offline, consists in the model setup and tuning, the training dataset generation and the CNN training. The second one, performed online, is relative to the experimental current pattern acquisition and their processing by the trained CNN, for a continuous monitoring of the health conditions of the motor. Therefore, the algorithm well fits for the Industry 4.0 paradigm and can be easily adapted to an IoT environment. The integration of the PMSM drive in an articulate and complex system eases the exchange of data between the components of the system itself. With such a structure it is possible to designate each task to the appropriate element. So the operations which need determinism and real-time behaviour, as for the motor control, are implemented in the slave inverter, while the condition monitoring of the motor can be performed by a master server which can be devoted also to other, more complex, but not deterministic tasks. The interconnection guarantees an online master-slave communication. The slave can acquire in real-time the motor current patterns sending them to the master, that performs the condition monitoring and takes the proper actions if it detects a potentially dangerous situation.

The use of 1-D CNNs fits for the simplicity that is required by the industrial field, while providing the benefits of versatility and robustness typical of artificial intelligence.

From the very beginning, the approach was intended to be comprehensive, in the sense of addressing every theoretical and implementation aspect. An objective impediment to the straightforward transposition of the techniques used for image recognition to the field of electric motors is the lack of an adequate number of test cases.

To tackle the problem and as a distinctive feature of this thesis, we proposed the generation of artificial training patterns, obtained on motor models validated on custom prototypes. The effort is certainly less than either finding a vast archive of faulty current signatures, or reproducing the faults by damaging several motors.

The models were merged in the complete AC drive simulation, to get realistic current patterns. Actually, the second important feature of this work is that it uses

only existing current sensors, present in any AC motor drive.

The datasets for both training and validation were enlarged by using simple DA techniques. Some more advanced and challenging methods are worth deepening in a next research steps.

The chapter includes all the design hints for reproducing the condition monitoring system. Experimental results relative to each stage have been included, and final verification of the classification ability, carried out on real prototypes, has confirmed the effectiveness and the practical feasibility.

The procedure is general and relevant for all the types of fault that have a measurable effect on phase currents. The approach is then easily extendible to other faults, as for example the ball bearing-related ones and to other types of motor as well. The results of this activity are documented in [89].

4

IM FAULT DETECTION USING STRAY FLUX MEASUREMENTS

In recent years, predictive maintenance on IMs has become of increasing interest in the industry, due to the intense participation of these machines in a vast number of processes and applications. Despite the characteristic robustness of the machines, the severe repercussions of failures justify the development of diagnostic techniques to avoid premature failures. This chapter and the following one are targetted to the early fault detection of this type of electrical machines.

One of the most widely used diagnostic techniques in the industry (especially for IMs) is the MCSA, which analyses the current during steady-state operation. However, the classical techniques have some drawbacks. Many of the techniques are not immune to the existence of false indicators caused by the presence of oscillations in the load torque or fluctuations in the supply voltage [31]. In this respect, techniques such as transient stray-flux analysis can provide immunity against those phenomena. The technique also has other advantages over other classical techniques which are widely used in industry, such as the non-invasive nature and the low cost of the sensors that are required. This can convert stray-flux analysis onto an excellent alternative or complement for the diagnosis [22], [53].

Several works have studied the viability of this approach to detect different type of failures, such as eccentricities [75, 97], rotor damages [8, 42, 85, 93, 94], coupling system problems [29] and even winding asymmetries in wound rotor induction motors [116]. Many of these papers are based on the analysis of these EMF signals under steady-state conditions. However, there are some drawbacks when using classical methods. The presence of load torque oscillations or rotor axial air ducts could result in a false positive in steady-state analysis.

On the other hand, it is well-known that IMs demand a high current under starting. This has negative effects such as significant voltage drops in the installations, possibility of stressing the motor insulation and additional energy wastes under starting. Due to this, different reduced voltage modalities have been proposed with the aim of reducing the startup current peak, being the use of soft-starters quite extended in industry.

Soft-starters are based on modifying the supply voltage applied to the motor by changing its rms value with the aim of allowing a softer startup. Most are based on a power circuit with anti-parallel thyristors installed on one, two or all three phases of the motor supply line (i.e. one, two or three-phase control). Changing the angle of the thyristors, enables the variation of the rms value of the voltage applied to the motor. Many soft-starters allow certain parameters to be varied at start-up. The most common soft-starters allow the starting time and the percentage of voltage applied to be varied, and some even allow the current to be limited during starting.

However, the use of soft-starters does not avoid the possibility of motor failures. In fact, their use is known to amplify certain harmonics and introduce others, which could make motor diagnostics more difficult [26], [25].

This chapter presents the results of a joint research, made in collaboration with professor Antonino Daviu of the Universitat Politecnica de Valenica and it is aimed to the analysis of the stray-flux in the transient regime in motors started by using static starters. The patterns obtained by analysing the stray-flux have been characterised by various authors. Despite this, the translation of these signals to the identification of the health degree of the motor is still subject to the user's interpretation. In line with the paradigm of "more intelligent drives" that is the thread of my thesis, the target was then to automate the fault diagnosis using artificial intelligence techniques. CNNs will be applied with the ultimate goal of obtaining an automatic diagnosis of the fault (i.e. without user intervention). Even in this case the main issue to deal with is the availability of a proper training dataset. Differently from the case of PMSMs, the very complex nature of the stray flux signal makes difficult the realization of an accurate model able to artificially generate the training dataset. As a valid alternative, in this case the poor experimental training dataset has been intelligently dealt through some drive-oriented data augmentation techniques.

4.1 *Rotor Bar Damage*

Stray-flux analysis under the starting transient allows the detection of different types of faults in induction motors [93]-[116]. With regards to bar breakages, some components are amplified over others in the time-frequency maps. It has been shown that the $s \cdot f$ and $3 \cdot s \cdot f$ components (where f is the supply frequency and s is the slip) are particularly sensitive to rotor faults [14]. These components are axial in nature. On the other hand, the $s \cdot f$ component can also be amplified in the case of the existence of eccentricities in the machine [14].

In addition to the components of axial nature, there are components of radial nature given by $f \cdot (1 \pm 2s)$. These components are known as the sideband components, located on either side of the fundamental frequency, depending on the sign that is considered [14].

The nature of the failure components is relevant since depending on the position of the sensor the Electro-Motive Force (EMF) induced components will be axial or radial. Figure 4.1 shows the different sensor positions usually considered for stray-flux measurement. In position A, the sensor measures axial flux. In position B, the sensor measures radial flux and a portion of axial flux. Finally, sensor position C measures radial flux (Figure 4.1). Depending on the position studied, one component or the other prevails.

On the other hand, it should be noted that some authors have shown that the existence of bar breakage can amplify the component related to eccentricities or misalignments with the load given by $f_{ecc} = f \cdot (1 \pm m \cdot \frac{(1-s)}{p})$ (p is the number of pole pairs and $m = 1, 2, 3 \ldots$) [52].

All components are slip-dependent and therefore follow a certain evolution during the transient which was well-characterized in previous works of the Spain research group [93]-[116]. In particular, the Short Time Fourier Transform (STFT) is applied

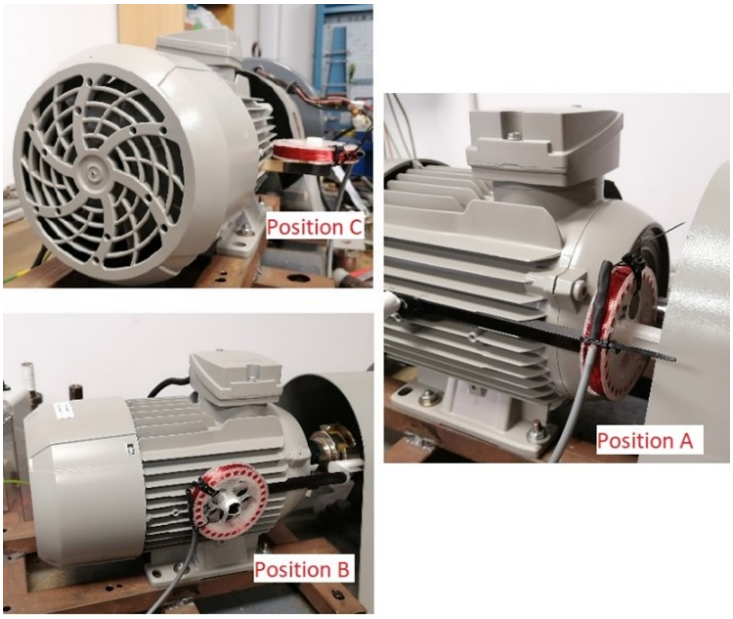

Figure 4.1. Coil sensor positions for stray flux measurements.

to process the signals obtained from coils. Using a Matlab program, the appropriate parameters have been modified to obtain a good representation of the time-frequency map and to visualise the fault patterns.

4.2 *Convolutional Neural Network Basics*

A CNN is a particular type of ANN which is especially suitable for image recognition problems. The key difference respect to a traditional Fully Connected ANN is in the application of at least one convolution process during the elaboration of the input image. This operation allows the recognition of the presence in the image of particular signatures useful for its classification. As a matter of fact, this stage of the network is also called *feature extraction stage*. This primary stage is followed by another stage that performs the classification of the image according to the extracted features (therefore called *classification stage*). The CNN design methodology used in this chapter is the same of previous chapter 3.

4.2.1 The importance of training phase - a comprehensive view

Once the network structure is determined, a tuning of its weights (or *learnable parameters*) is necessary. As a recall, this design step needs three different datasets, namely, training, validation and test datasets. In the following, the size of these datasets will be indicated by symbols n_{tr}, n_{va}, n_{te}, respectively. The first is used to tune iteratively the CNN weights, with the aim of optimizing the network performances on the classifi-

cation of this dataset. The validation one is used during the training, but not to update the weights. It is only needed as a mean to detect arise of overfitting issues [36]. It helps in understanding whether the network is going to improve its performance also on new data or only on the training ones (section 3.2.2). Finally, the test dataset is used to test the network capabilities on a dataset completely independent from the design procedure.

A crucial issue in electric drives is the availability of these large datasets. In the present work, the enhancement of poor training datasets through DA techniques tailored on the application is the main key point. It will be dealt with separately in section 4.2.2.

The training procedure is composed by two steps, namely the forward propagation and the back-propagation. In the former, the training samples are fed to the network returning for each image of the training dataset the relative estimated classification. These estimates are then compared with the correct labels to obtain the classification error on the training dataset. In the latter, the back-propagation of this error is applied, updating the network weights with the aim of minimizing the training error as cost function of this optimization process.

Different algorithms for the update of these weights are already present in literature [67]. The iterative repetition of the forward and backward operations returns the optimal choice of the network weights for the considered training dataset.

Periodically, to monitor the network capabilities, a forward propagation of the validation dataset is applied. This is not followed by the back-propagation update. Actually, to recognize the overfitting condition, the validation dataset should not influence the CNN weights.

4.2.2 The data augmentation of training dataset

The absence of a large volume of historic data in the electric drives field is the main barrier to the diffusion of knowledge-based fault detection systems. It has been found, and proposed in this chapter, that a simple and immediate solution relies on DA theory.

Basically, DA means a synthetic generation of training samples. It encompasses a suite of techniques for the artificial enlargement of the available dataset using some label-preserving transformations [99]. The goal is a better exploration of the input space can be achieved while maintaining correct labels [112].

It is worth noting that the STFT images are very simple respect to the typical applications of CNNs. Therefore, it is expected that among the several DA techniques available in literature the more basics can easily and effectively improve the CNN classifier performances. The study was focused on which of them were best suited for this application. They turned out to the following:

- Random Cropping (RC): it consists in a random crop of a portion of the original image with a next resize to fit the CNN input size requirements. The aspect ratio of the crop is equal to the original image while its dimensions are determined according to a scaling factor. With a high scaling factor the crop is similar to the original image while little translations with a spreader distribution of the harmonics involved in the image can be emulated.

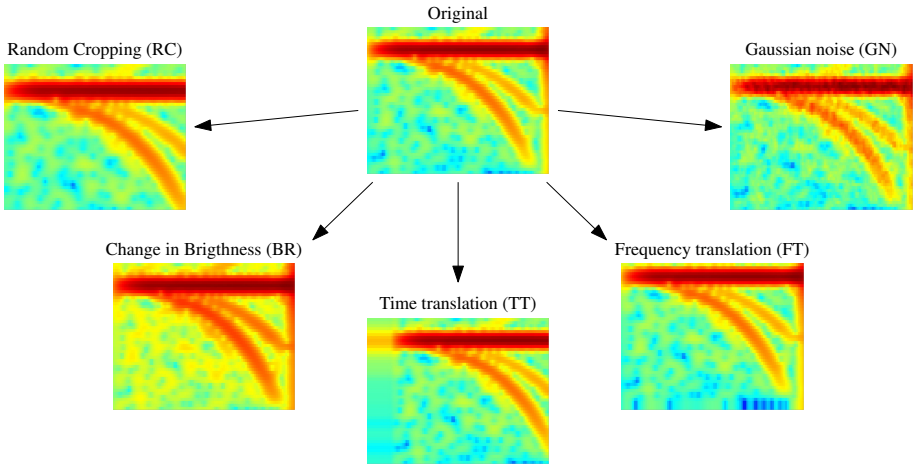

Figure 4.2. Data augmentation techniques on a STFT image sampled from a one broken bar motors.

- Change in Brightness (BR): in practice it is a random scale in amplitude of the original STFT values. This transformation takes into account of slight variations of the fault-related harmonic intensity or of other spurious ones.
- Time Translation (TT): A single transient can occur repeatedly with some time delay resulting in horizontal offsets of the original STFT image. This phenomena can be easily taken into account shifting the image by a random number of samples. The empty space left in the opposite side of the shift direction is filled replicating the last sample column for all the empty columns.
- Frequency Translation (FT): As the previous transformation but along the frequency axis (i.e. vertical of the STFT image). Although this behaviour is not expected because of the constant supply frequency, the addition of this augmentation can improve the CNN robustness on small variations of the frequency distribution of the STFT.
- Addition of Gaussian Noise (GN): To achieve a satisfactory robustness to noise measurements a Gaussian noise can be added on the STFT images with zero mean and randomly chosen standard deviation.

The chosen parameters must generate reasonable images and their proper definition is part of the designer expertise, acquired on the particular application (especially the chosen STFT features). A graphical description of the mentioned DA techniques applied on a STFT image is reported in Figure 4.2.

4.3 *Fault detection - design of experiment*

For the class of drives here considered a well-diffused solution to economically start the motor while limiting the stator currents is the soft-starter. Therefore, the fault detection of soft-started IMs was considered in the experimental stage.

In particular, my study was focused on the evaluation of the effectiveness of DA in the performance improvement of CNN-based predictive maintenance tools. In order to provide this, different CNNs were used for the detection of broken bar damages of an experimental IM prototype. The measurement setup and the STFT parameters are reported in section 4.3.1. To appreciate the effect of DA, the same CNN structure and training options are maintained the same and they are described in section 4.3.2. Therefore, the only difference among the reported cases is in the training dataset generation according to the DA technique previously described into section 4.2.2.

4.3.1 Induction motor drive setup and stray flux signal processing

The tests carried out in the laboratory consist of a 1.1 kW squirrel cage motor, which was subjected to the bar damages, coupled to a DC motor acting as a load.

The motor was started using 4 different industrial starters, modifying the parameters of starting time and applied voltage. Each of the tests was carried out with and without load. Two sensor positions, A and B, were studied (Figure 4.1).

Through the described experimental setup 180 different start-up STFTs were collected, equally distributed among the three considered fault conditions (Healthy (H), One Broken Bar (1BB), Two Broken Bars (2BB)). Of these, the 60 % (108 samples) were randomly chosen as training dataset, 10 % (18 samples) for the validation dataset while the remaining (54 samples) were used as test dataset.

4.3.2 The adopted convolutional neural network structure and training parameters

The design of a CNN is a very complex task, due to the large number of possibilities and parameters. This is the main concern when approaching the use of this powerful, but rather challenging tool. As highlighted in the previous chapter and published in [89] there are some useful guidelines and hints that can be followed for the design of a CNN applied to electric drives. In that work the observed signals were time-series, but the developed concepts also apply to the 2-dimensional case. Following those hints, the final network architecture was obtained (Figure 4.3). The CNN consists of a four element sequence. The convolution stage recognizes the presence of more or less complex signatures in the signal pattern thanks to some filters normally called kernels. The size of the input image elaborated by the convolution, was equal to 200 samples along time axis (abscissa), 100 samples along frequency axis (ordinate). The convolution process was composed by 10 kernels (with size 80 × 40). The nonlinear behaviour of the classification problem calls for nonlinear elements in the CNN. This feature is guaranteed through a ReLU which improves the fitting capabilities of the network (see section 3.2). Therefore, each output of the convolution is passed through a ReLU function. A FC layer is then used to elaborate the features extracted from the previous layers. The number of output neurons is equal to the number of classes that the network has to recognize (namely H, 1BB, 2BB). Finally, a softmax operation returns the most probable class as classification of the elaborated input image (section 3.4.1).

Also in this case the SGD was chosen as training algorithm for its simple implementation (section 3.2.2). The training dataset size n_{tr} will be different in function of the DA

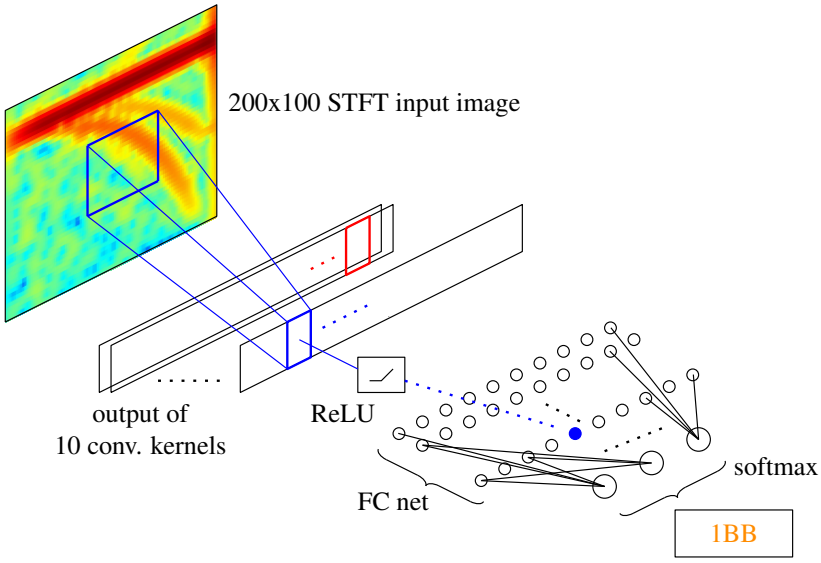

Figure 4.3. CNN architecture for STFT analysis.

technique applied on the 108 initially available training samples. The training dataset was subdivided in mini-batches [72]. During the classification of each mini-batch a cumulative 0-1 loss function was evaluated. The error obtained at the end of the mini-batch was then back-propagated through the network for the optimization of its weights. The choice of the mini-batch size is arbitrary. If the mini-batch size is equal to one sample the resulting training would be slow (for each sample a back-propagation is applied) and noisy. The opposite boundary is to choose the batch size as the entire training dataset. In this case, the training will be smoother and faster as less back-propagation iterations are required. It is worth noticing that some noisy behaviour is useful in an optimization problem, as it helps in avoiding the convergence on local minima of the cost function. For the Author expertise a proper value of the batch size is one hundredth of the training dataset size.

Another important parameter is the learning rate which represents how fast the network should learn from its classification errors. High learning rate implies that for the same error an heavier modification of the weights during the back-propagation is obtained. In order to avoid instability of the training process this parameter should be initially chosen very small and gradually increased to speed up the procedure. Another useful tip is to gradually decrease the learning rate during the progress of the training to obtain a fine tuning of the network weights, avoiding to excessively oscillate around the optimal point. An initial learning rate equal to 10^{-5} was chosen and it was divided by a factor of ten every 5 epochs, i.e. every 5 times the entire training dataset was given to the network. The training of the network was performed offline on a GPU Nvidia GeForce 1070 GTX board.

The training dataset was augmented through the techniques described in section 4.2.2. Here below, the main parameters of the DA techniques are summarised.

- RC: a random scaling factor for the crop was chosen between the boundaries 0.9 and 0.99.
- BR: a random scaling factor in brightness was chosen between 0.95 and 1.15.
- TT: a random value of time samples delay was chosen between −15 and 15.
- FT: a random value of frequency samples offset was chosen between −10 and 10.
- GN: a zero-mean and random value (below 15) of the variance were chosen for the application of the Gaussian Noise.

4.4 *Experimental results*

By exploiting the experimental setup described above, 7 different training datasets were realized. A first dataset was composed by only the experimental measurements, without applying any of the mentioned DA techniques. It represented the classical application of an AI-tool, i.e. taking advantage of some previously collected historical data (108 for the training, 18 for the validation and 54 for the test) a CNN was trained to recognize the failure condition.

Other 5 training datasets were developed applying only one DA technique at a time on the initial dataset. Considering for example the Random Cropping, in addition to the raw images, the training dataset was composed by 2 random cropping for each image. The resulting training dataset size was equal to 432 samples ($(2+1)\times 108 = 432$). The same was made for the other 4 DA techniques (BR, TT, FT, GN).

The last (7^{th}) dataset was realized to appreciate the effect of the simultaneous application of all the methods. The same DA options were applied concurrently on the initial training dataset in this case. Therefore, the total amount of training samples were $(2 + 1)^5 \times 108 = 26244$, which is a significant increase over the initial small batch.

Once these semi-synthetic datasets were realized, 7 CNNs with equal structures were trained on them. The previously acquired $n_{va} = 18$ and $n_{te} = 54$ samples were used respectively to validate (during the training) and to test each network. The obtained predictors accuracy on the test dataset was evaluated as number of correct predictions over the total amount of classifications.

The features and results of the 7 described experiments are reported in Table 4.1. From the table it is possible to appreciate that the network trained on the raw data is characterized by very poor performance. Only the 61.1 % of the test samples were correctly classified. The improvements linked to each DA technique are also reported. Each of them enhances the network capabilities but it is shown that only the application of all DA techniques leads to a very good accuracy (94.4 %). The intersection of all of them seems to improve, rather than weaken, CNN's performance.

Taking the application of all DA case as the best solution to the artificial dataset generation, the evolution of the accuracy and loss quantities, as well as the confusion matrix relative to the classification of the test dataset are reported in Figure 4.4a and 4.4b, respectively.

A gradual improvement of network classification indexes is observed during the training and no evident overfitting issues are noticed (validation points are quite close to training ones in Figure 4.4a). The confusion matrix shows that among the 54 test samples only 3 are wrongly classified (accuracy = 94.4 %).

Table 4.1. Features of the augmented training datasets. n_{tr}, n_{va} and n_{te} represent the number of samples used for the training, for the validation and for testing, respectively.

Dataset n	DA technique	n_{tr}	n_{va}	n_{te}	accuracy
1	None	108	18	54	61.1 %
2	RC	324	18	54	72.2 %
3	BR	324	18	54	70.4 %
4	TT	324	18	54	74.1 %
5	FT	324	18	54	68.5 %
6	GN	324	18	54	70.4 %
7	All	26244	18	54	94.4 %

Among the three wrong classifications, in two cases a fault with 2 broken bars was recognized as 1BB and in one case it was vice-versa. Therefore, the incorrect predictions refer only to the severity of the failure, not whether it is present or not. This is definitely less serious than predicting a false healthy/faulty motor condition.

4.5 *Conclusive remarks*

The chapter draws some considerations about AI the feasibility of artificial intelligence techniques to automate the diagnosis of induction motors started by soft starters.

The difficulty with this work was that soft starters introduce harmonics, and this can make it difficult to detect the characteristic patterns of the fault components. The other big drawback common to any ANN-based technique is that a large amount of data is required for training. Despite this, the DA techniques selected and applied in this thesis work have led to a correct detection of the fault in an automatic way, based on the transient evolutions of the fault harmonics present in the flux signals under the starting. The experimental stage has demonstrated the feasibility of the proposed method, that is ready for industrial implementation. Partial results of this work were published in [87] while the more recent achievements are currently being presented at the 47th Annual Conference of the IEEE Industrial Electronics Society [88].

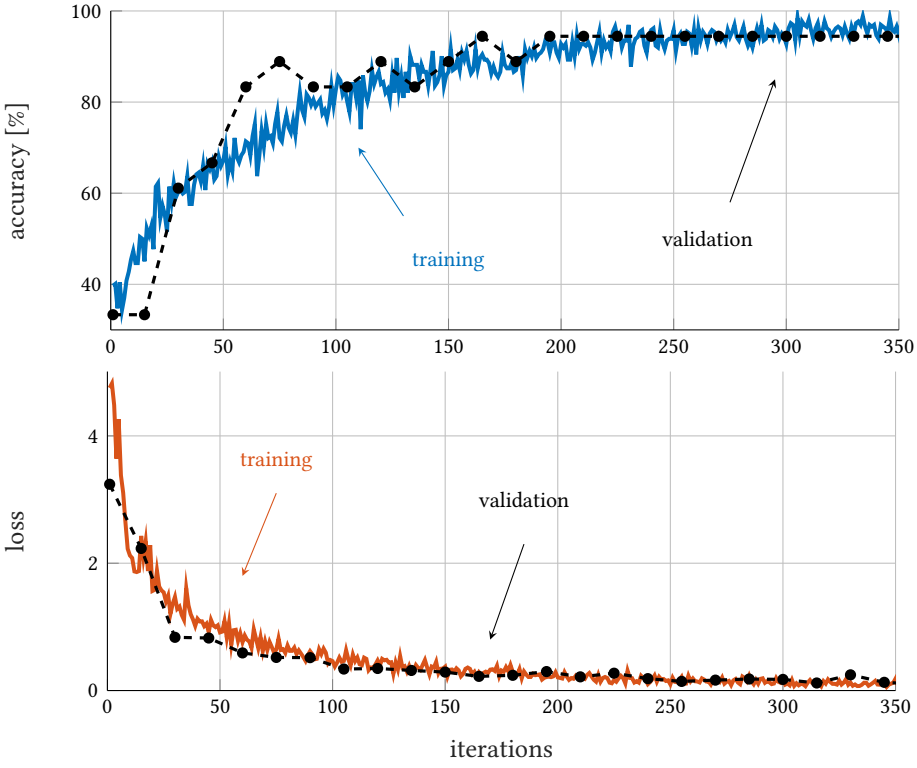

(a) Accuracy and loss evolution.

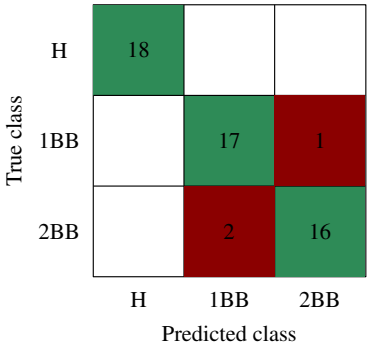

(b) Confusion matrix of test dataset classification.

Figure 4.4. Results achieved tuning the CNN weights on complete training dataset (number 7).

5

IM FAULT DETECTION USING STATOR CURRENTS

In this chapter the broken bar fault prediction of IMs is still considered. Somehow merging the concepts of the previous chapters, the aim of the present one is to describe a CNN-based algorithm able to recognize the fault condition elaborating the motor currents during the start-up, thus avoiding the necessity of additional stray-flux sensors.

As detailed in the chapter, to tackle the need of a huge amount of experimental data an accurate model of the IM is derived with the aim of generating artificially the entire training dataset. The model takes advantage of several FEA and a specific ANN for the accurate description of the magnetic behaviour under different levels of failures.

The recognition capabilities of the CNN when classifying concomitant or different faults were not tested, but as reported in reference [80], each of the most common faults in IMs affects the current with different harmonics. Therefore, it is expected the CNN is able to minimize incorrect classifications even with other or mixed failure conditions if a proper, comprehensive training dataset is used. Inverter faults are abrupt and disruptive and therefore they cannot be included in an early fault detection system. On the other hand, the proposed algorithm was designed to recognize the failure condition during the start-up of the motor through a wide range of possible start-up transients. Nothing can be said on the behaviour of the algorithm under transients outside the ones used for the training.

5.1 *Broken bar induction motor model*

In this section a model of the squirrel cage IM is developed. It is oriented to the study of broken bars, but its completeness makes it eligible for the analysis of other failures that may affect the IM, too. The aim of this model is the artificial generation of the training dataset

First, the overall mathematical description is reported. Then, the dissertation is focused on the attainment of the motor magnetic relationship through the exploitation of some FEA and an ANN. Finally, a brief mathematical recap of the wavelet transform is exposed.

5.1.1 Mathematical background

The electrical dynamic behaviour of the IM can be described in different coordinate systems. In this chapter the spatial vector notation is considered and a stationary reference frame $\alpha\beta$ fixed to the stator winding is preferred. As a matter of fact, the

implementation on a synchronous reference frame would need the knowledge of the rotor flux position. This approach is particularly suitable from the standard control point of view in which only the fundamental synchronous component is of interest. In the present case in which the key point is the behaviour of the other fault-related harmonics, the synchronous reference frame results unsuitable.

The voltage balance equations for the stator and rotor are the following:

$$\begin{aligned} \mathbf{u}_s &= \mathbf{R}_s \mathbf{i}_s + \frac{d\boldsymbol{\lambda}_s}{dt} \\ \mathbf{0} &= \mathbf{R}_r \mathbf{i}_r + \frac{d\boldsymbol{\lambda}_r}{dt} + \omega_{me} \mathbf{J} \boldsymbol{\lambda}_r \end{aligned} \quad , \quad \mathbf{J} = \begin{bmatrix} 0 & 1 \\ -1 & 0 \end{bmatrix} \tag{5.1}$$

where $\mathbf{u}_s = \left[u_{s\alpha}, u_{s\beta}\right]^T$, $\mathbf{i}_s = \left[i_{s\alpha}, i_{s\beta}\right]^T$, $\boldsymbol{\lambda}_s = \left[\lambda_{s\alpha}, \lambda_{s\beta}\right]^T$ and $\mathbf{R}_s = \text{diag}(R_s)$ are the stator voltages, currents, flux linkages and constant resistance matrix, respectively. The same quantities for the rotor are indicated with symbols $\mathbf{u}_r = \left[u_{r\alpha}, u_{r\beta}\right]^T$, $\mathbf{i}_r = \left[i_{r\alpha}, i_{r\beta}\right]^T$, $\boldsymbol{\lambda}_r = \left[\lambda_{r\alpha}, \lambda_{r\beta}\right]^T$ and $\mathbf{R}_r = \text{diag}(R_r)$, in which the rotor voltages are equal to zero, due to the squirrel cage structure. The electromechanical speed and position are respectively $\omega_{me} = p\omega_m$ and $\vartheta_{me} = p\vartheta_m$, with p the number of pole pairs of the motor.

To keep the model as general as possible, the flux linkage vectors $\boldsymbol{\lambda}_s$, $\boldsymbol{\lambda}_r$ are expressed as nonlinear functions of both current vectors $\mathbf{i}_s$, $\mathbf{i}_r$. The saturation of the iron core is the main cause of nonlinearity, that becomes even more pronounced in the case of failure, due to the intrinsic asymmetry involved.

It is also worth to note that a broken bar generates speed-dependent harmonics, that are the best indicators of the health conditions. Therefore, for a simulation to be a valid substitute of a real damaged motor, it has to include the rotor position in the magnetic model.

The electromechanical torque τ generated by the motor can be expressed as

$$\tau = \frac{3}{2} p \left(\lambda_{r\beta} i_{r\alpha} - \lambda_{r\alpha} i_{r\beta} \right) \tag{5.2}$$

while the motor mechanical dynamic is described by the following equation.

$$\tau - \tau_L = J \frac{d\omega_m}{dt} + B\omega_m \tag{5.3}$$

The inertia of the motor and the viscous friction are indicated with symbols J and B respectively and an external load torque τ_L is considered. Equations (5.1), (5.2) and (5.3) lead to the graphical representation of the IM model shown in Figure 5.1. The same figure includes the block schematic of the different start-up methods that were used to gather the simulated start-up current patterns described in Section 5.4. Quantities A and f represent respectively amplitude and frequency of the three-phase sinusoidal voltage reference to the inverter-fed IM.

The magnetic model is represented by the multi-input, multi-output function $\mathbf{g}$. The determination of $\mathbf{g}$ is not trivial, since the FEA just produces (for any given position) a direct map $\mathbf{f}$ from currents to flux linkages. The details are given in Section 5.1.3.

Finally, it is worth noting that a broken bar affects the model twice, both in $\mathbf{g}$ and the rotor resistance matrix $\mathbf{R}_r$. Accounting for a resistance variation in the rotor bars

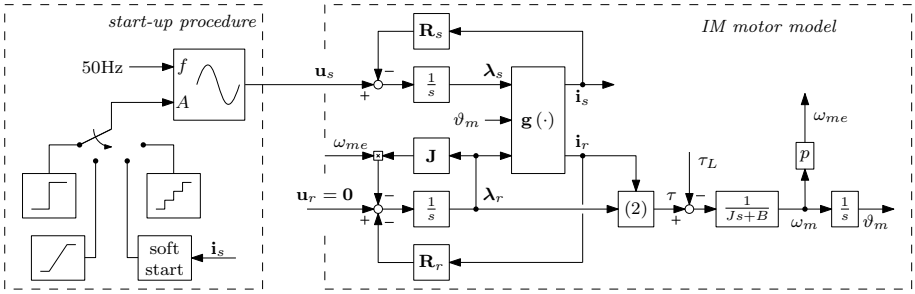

Figure 5.1. IM model for both healthy and faulty cases and drive setup for the generation of artificial training sequences.

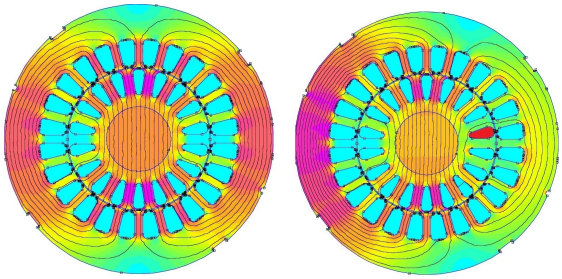

(a) Healthy motor. (b) One broken bar motor.

Figure 5.2. IM sheet drawings and FEA under different health conditions.

would imply the return to a three-phase physical model, that could hardly be included in a complete drive simulation as that depicted by Figure 5.1. On the other hand, the proposed health monitoring is able to identify a single broken bar failure, so that the overall phase resistance variation remains very limited. Some tests have proven that considering a constant resistance matrix $\mathbf{R}_r$ even after the fault does not compromise the accuracy of the current pattern generation.

5.1.2 Finite element analysis for the determination of the magnetic model

Symbol $\mathbf{f}$ represents a multivariate function which maps the quintuple $\left[i_{s\alpha}, i_{s\beta}, i_{r\alpha}, i_{r\beta}, \vartheta_m\right]^T = [\mathbf{i}_s, \mathbf{i}_r, \vartheta_m]^T$ to the quadruple $\left[\lambda_{s\alpha}, \lambda_{s\beta}, \lambda_{r\alpha}, \lambda_{r\beta}\right]^T = [\boldsymbol{\lambda}_s, \boldsymbol{\lambda}_r]^T$. The accurate determination of this function by measurements on a real IM is almost impossible. Nonetheless, the availability of the stator and rotor sheets drawing allows to easily obtain $\mathbf{f}$, i.e. the *direct* magnetic model, through several FEA simulations. The main interesting parameters of the considered motor are shown in Table 5.1 and the relative stator and rotor sheets can be appreciated in Figure 5.2.

Each FEA is realized initializing an input vector $[\mathbf{i}_s, \mathbf{i}_r, \vartheta_m]^T$, while the output of the simulation is the vector of the fluxes $[\boldsymbol{\lambda}_s, \boldsymbol{\lambda}_r]^T$. Evaluating the output for different input points, it is possible to estimate the non-linear function $\mathbf{f}$ as four look-up tables

Table 5.1. IM parameters.

Symbol	Parameter	Value
P_n	Nominal power	3000 W
p	Number of pole pairs	1
I_n	Nominal current	9.3 A
ω_n	Nominal speed	2900 rpm
N_{ss}	Number of stator slots	24
N_{rs}	Number of rotor slots	18

with one output and five input variables each.

It should be remembered that all the currents and fluxes are referred to a stationary reference frame fixed with the stator. Therefore, there is the need to report the variables in the relative abc reference frame in order to impose the correct FEA currents in both the stator and the rotor [16], [4]. Once the currents and the rotor position are imposed on FEA drawing, the simulation returns one point of the function $\mathbf{f}$.

If a motor with one broken bar is considered, it is sufficient to limit the current in the relative bar, to an extent determined by the degree of the damage. A qualitative example is shown in Figure 5.2, in which for the same input vector $[\mathbf{i}_s, \mathbf{i}_r, \vartheta_m]^T = [0\text{ A}, 0\text{ A}, 0\text{ A}, 3\text{ A}, 0^\circ]^T$ the results obtained considering an healthy rotor and a rotor with one completely broken bar (current in the slot equal to zero) are reported. The damaged bar is the red-coloured one and it highlights the possible effects of the broken bar on the magnetic flux path. The failure distorts the flux density distribution creating an asymmetry in the machine which is anyway well described through the respective non-linear function $\mathbf{f}$.

Repeating the simulation for different input vectors it is possible to map $\mathbf{f}$ in the considered healthy and faulty case. In the present application, it was evaluated for each combination of the currents among the following values: $[-1, -0.4, -0.2, 0, 0.2, 0.4, 1]\, I_n$. In order to reduce the simulation time requirements some symmetries were exploited and the position was changed by constant steps of 7.5° between 0° to 60° and 0° to 180° for the healthy and faulty rotor respectively. Therefore, the function $\mathbf{f}$ consists of four look-up tables (one for each stator and rotor flux linkage component) with $7^4 \cdot (60/7.5 + 1) = 21609$ points for the healthy motor and 60025 points for the faulty case. These vectors were chosen as the best compromise between the computational load and the accuracy in modelling both the saturation and the position harmonics.

The multi-dimensionality of $\mathbf{f}$ makes a comprehensive graphic investigation very cumbersome. Anyway, some useful considerations can be made observing the behaviour of $\mathbf{f}$ by imposing changes only to some of the input variables, while maintaining fixed the others. For example, the evolution of the stator flux along the α-axis varying the currents (Figure 5.3a, 5.3b) or position (Figure 5.3c) are shown in Figure 5.3.

Figure 5.3a reports the stator flux linkage as function of the stator and rotor currents along the α axis from $-I_n$ to I_n. In a linear system, the graph would be a plane, being the flux a linear combination of the α-axis currents. Yellowish and deep blue meshes, relative to the curved upper and lower part of the graph are representative of iron

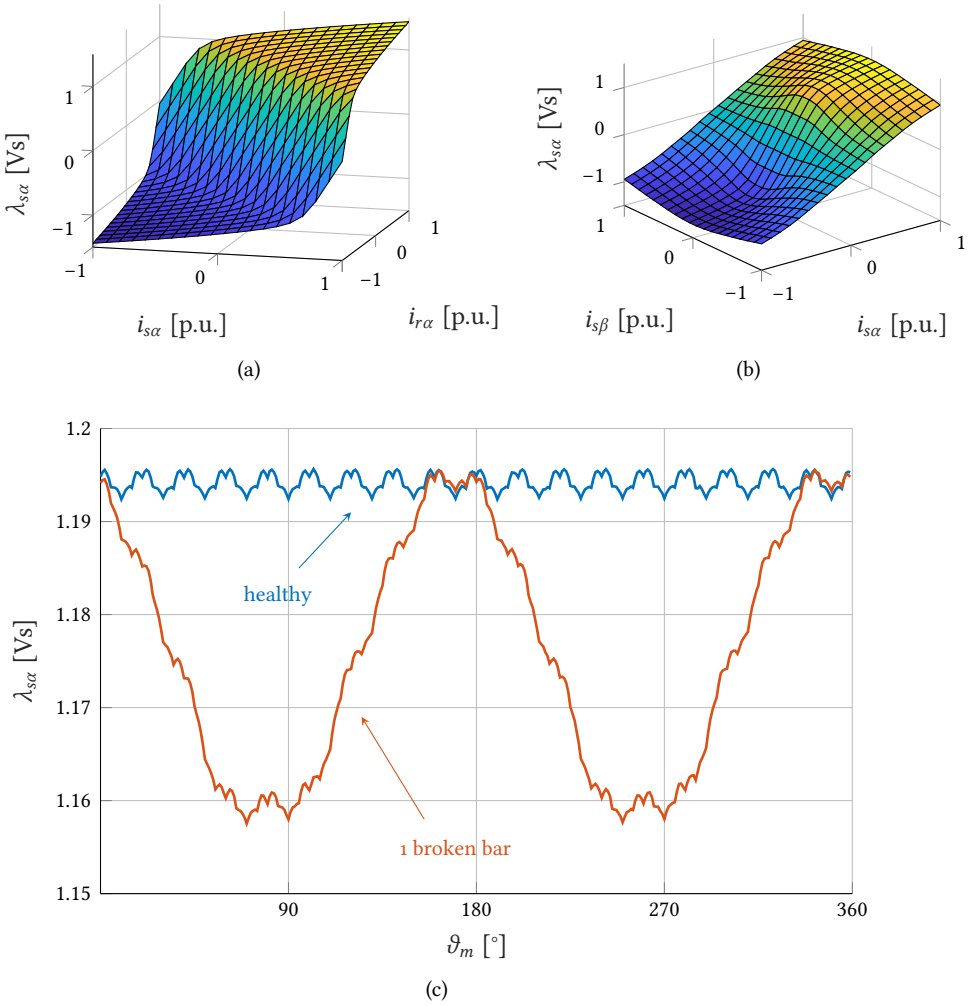

Figure 5.3. IM magnetic model (current to flux linkages), obtained through FEA simulations. (a): $\lambda_{s\alpha}$ as function of the stator and rotor α currents ($i_{s\beta} = i_{r_\beta} = 0$ A, $\vartheta_m = 0^\circ$) in the healthy IM. (b): $\lambda_{s\alpha}$ as function of the stator currents ($i_{r\alpha} = i_{r_\beta} = 0$ A, $\vartheta_m = 0^\circ$) in the healthy IM. (c): $\lambda_{s\alpha}$ as function of the position ($i_{s\alpha} = i_{s_\beta} = i_{r_\beta} = 0$ A, $i_{r\alpha} = I_n$) in both healthy and damaged motor.

saturation, that evidently begins below the nominal current.

In Figure 5.3b, one appreciates the presence of some cross-coupling between the $\alpha\beta$ axes. This is another non-ideality that can be easily modelled through the proposed FEA-based approach.

Finally, Figure 5.3c shows the flux linkage as function of the rotor position (i.e., the position of the broken bar), while a current $i_{r\alpha} = I_n$ was applied (all the other currents were null). With respect to the healthy case, the fault condition causes a position-dependent oscillation to appear, which is the cause of the fault harmonics at the mechanical frequency and around.

The general concept that comes out from Figure 5.3 is that only a FEA-based model is capable of encompassing all of the IM details necessary for generating a reliable set of current patterns, that in turn will be used for an effective training of the CNN, as detailed in section 5.4.

As mentioned, the IM model depicted in Figure 5.1 requires the inverse function $\mathbf{g} = \mathbf{f}^{-1}$. Even in the simpler case of a two-dimensional magnetic model, the inversion requires special precautions [6]. After some trials, it becomes soon evident that the nonlinearity makes the multivariable system really hard to reverse. For each angular position, FEA provide a four-dimensional vector map, that can be imagined as scattered input-output data links. The problem is the interpolation of the function out of the known points. A particularly efficient and original solution specifically developed to solve the problem is described in the next section.

5.1.3 The magnetic model interpolation based on artificial neural network

After FEA simulations, a set of precise relations between flux linkages $[\boldsymbol{\lambda}_s, \boldsymbol{\lambda}_r]^T$ and currents $[\mathbf{i}_s, \mathbf{i}_r, \vartheta_m]^T$ is available for each rotor position ϑ_m. An analytical approach to interpolation is extremely involved, and this has sparked interest in an artificial neural network solution. The ANN can be trained in order to obtain an approximating function of the scattered points used during the training. Among the possible solutions, a fully connected feedforward ANN has been shown to successfully accomplish the task.

In the design procedure, the network complexity is increased until it proves to be able to solve the given problem. For example, one-neuron network is surely not able to fit the considered $\mathbf{g}$ function. Conversely, a network with thousands of neurons would be not only complex in the implementation, but also particularly sensitive to the problem of overfitting [36]. Gradually increasing the network complexity and continuously evaluating its performances through the comparison between training and validation losses, it is possible to find the right balance, in the narrow space between underfitting and overfitting. The approach is very similar to the method used to design the CNN in chapter 3 and described in section 3.2.2. Transposing that design method and tailoring it to the ANN case the procedure reported in Figure 5.4

The architecture of the ANN obtained in this chapter is shown in Figure 5.5. It features just one hidden layer of $n_{hl} = 100$ fully connected neurons. The 5-element input vector $\mathbf{u} = [\boldsymbol{\lambda}_s, \boldsymbol{\lambda}_r, \vartheta_m]^T$ is linearly weighted by the $n_{hl} \times 5$ weight matrix $\mathbf{W}_1$ and the bias vector $\mathbf{b}_1$. Each of the n_{hl} weighted elements fires the sigmoid activation function σ associated to the neurons of the hidden layer, producing the n_{hl}-element

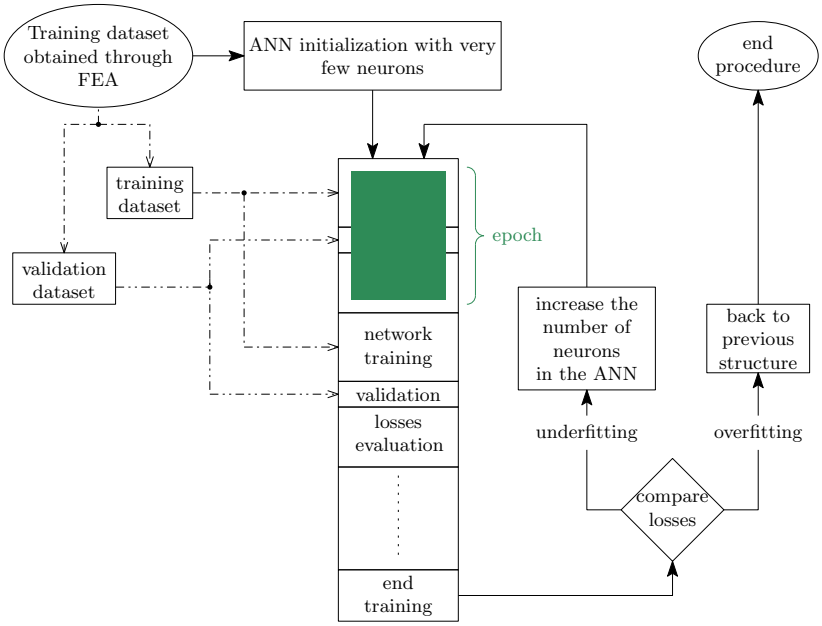

Figure 5.4. The iterative procedure for the design of the ANN..

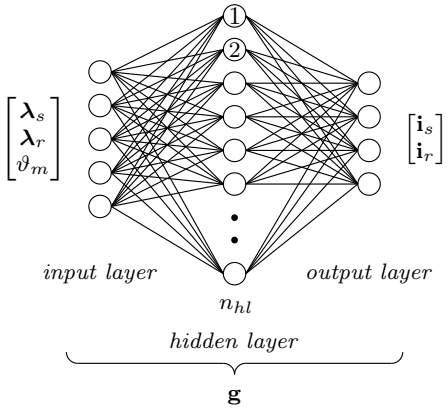

Figure 5.5. ANN architecture to reverse and interpolate the currents-to-fluxes motor model.

intermediate output vector $\mathbf{y}_{hl}$. The output layer returns the 4-element output vector $\mathbf{y} = [\mathbf{i}_s, \mathbf{i}_r]^T$ by a $4 \times n_{hl}$ weight matrix $\mathbf{W}_2$. The searched function $\mathbf{g}$, i.e. the *inverse* magnetic model, is obtained from the composition of the results of the two layers, that is, the inherent input-output behaviour of the ANN [36]:

$$\left.\begin{aligned} \mathbf{y}_{hl} &= \sigma\left(\mathbf{W}_1\mathbf{u} + \mathbf{b}_1\right) \\ \mathbf{y} &= \mathbf{W}_2\,\mathbf{y}_{hl} \end{aligned}\right\} \quad \mathbf{y} = \mathbf{g}(\mathbf{u}) \tag{5.4}$$

The weights of $\mathbf{W}_1$, $\mathbf{W}_2$ and bias $\mathbf{b}_1$ are obtained by training the ANN using the points of the function $\mathbf{f}$ derived from the FEA simulations. Of those, 60% were randomly selected for the training, 20% for test and the remaining 20% for validation, as common good practice [36].

The tuning of the ANN weights was realized through the Levenberg-Marquardt training algorithm [76]. This method, as the SGD, is used to solve non linear least square problems. It is a combination of two other methods: the gradient descent and the Gauss-Newton. Both the gradient descent and Gauss-Newton methods are iterative algorithms. The gradient descent differs in that at each iteration, the solution updates by choosing values that make the function value smaller. More specifically, the sum of the squared errors is reduced by moving toward the direction of steepest descent. In the Gauss-Newton method, the cost function is reduced assuming that it is locally quadratic in the parameters, and finding the minimum of this quadratic problem. At each iteration, the Levenberg–Marquardt algorithm chooses either the gradient descent or Gauss-Newton and updates the solution. The iterative update is dependent on the value of an algorithmic parameter, λ, a non-negative damping factor which smooths out the graph. The update is Gauss-Newton if λ is small (i.e. close to the optimal value) and a gradient descent if λ is large [33]. The Gauss-Newton is more accurate and faster than the gradient descent when close to the minimum error. While it is more complex from the implementation point of view, the merge of the two methods results in a more robust training. The complexity of the function the ANN has to interpolate led to choose the Levenberg-Marquardt rather than the previously used SGD for which no satisfactory results were achieved. In the present case the default level of $\lambda = 0.001$ suggested by the Matlab implementation was considered.

As an index for the evaluation of the ANN performances the mean squared error on the validation dataset estimation was used, and the training was stopped when this MSE was below $0.01\,\mathrm{V}^2\,\mathrm{s}^2$, which roughly corresponds to a mean error of ±1% over the known validation dataset.

5.1.4 Wavelet transformation

The presence of broken bars reflects into the current pattern through some harmonics around the supply frequency at $f_f = f\,(1 \pm 2s)$, as mentioned in the introduction. In particular, the proposed technique is focused on the observation of the smaller frequency $f\,(1 - 2s)$. This assumes its maximum value (f) at the beginning of the transient for which $s = 0$. It becomes 0 when $s = 0.5$ and then it increases again to a steady-state value, smaller than f, which depends on the load conditions. Therefore, the frequencies of interest are limited between 0 and f (50 Hz if the grid supply is

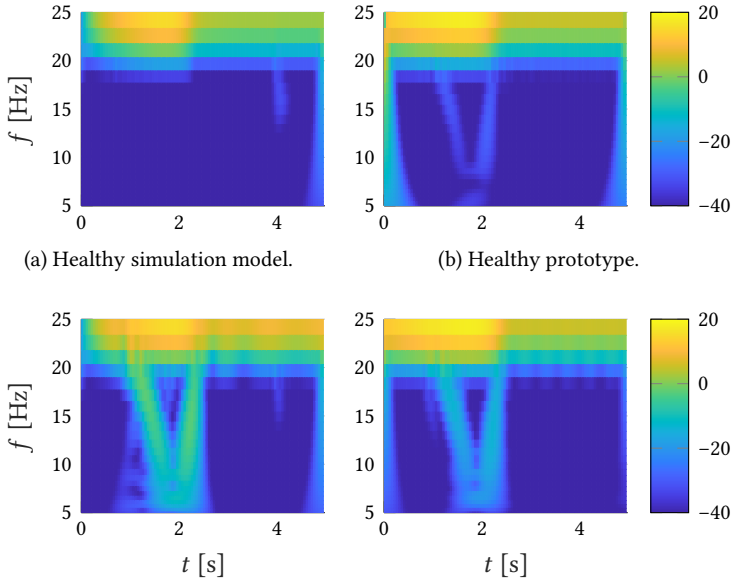

(a) Healthy simulation model.

(b) Healthy prototype.

(c) Faulty simulation model.

(d) Faulty prototype.

Figure 5.6. CWTs of the stator current under the start-up of the motor.

used). In synchronous motors the recognition of such harmonics may be profitably achieved by the direct monitoring of the current in the time domain at steady state [89]. Conversely, in IMs the harmonics are related to the slip frequency, so that monitoring during the transient start-up has to be preferred, as it involves high values of slip even at light loads. Nevertheless, the evaluation of a transient current pattern is easier in the frequency domain. Specifically, a joint time-frequency representation is needed, as for example the STFT used in chapter 4. Unfortunately, STFT is quite time consuming and it suffers of a trade-off between frequency and time resolution [91].

A more effective approach is based on the CWT, which is less computationally demanding and less resolution-critical than STFT [70]. The CWT has a $O(n)$ complexity [78], less than a conventional FFT which is $O(nlogn)$ For a deeper analysis and comparison of the two analysis tools (STFT and CWT) see appendices B and C. As the Fourier transform, also the CWT is based on the description of the signal through a base signal conveniently weighted and modified (*mother wavelet*). The transformation can be different in function of the chosen type of mother wavelet. In absence of a suitable unifying theory for wavelet behaviours, the choice of a particular wavelet for a particular problem may even appear arbitrary. In this chapter a Morse wavelet has been selected, as it may be recommended as an ideal starting point for general purpose use [66]. The application of the CWT tool to the acquired current patterns during IM speed start-up produces a 2D image able to describe the evolution of current spectra during the transient, as shown in Figure 5.6.

5.2 *Validation of the model for virtual patterns generation*

In order to validate the model represented in Figure 5.1, some of its (virtual) current patterns were compared with those obtained in a real experimental test bench. The validation process is of paramount importance, since the CNN fault detection capability will depend on the accuracy and precision of the dataset used during the training.

The experimental prototype is shown in Figure 5.7a. The IM motor was coupled to a permanent magnet synchronous motor acting as a virtual load. Both motors were controlled through a MicroLabBox dSpace FCP system. The current sampling was maintained at 10 kHz (synchronous with the inverter switching frequency) to avoid the current ripple induced by the modulation. Actually,the characteristic fault harmonics are very low in frequency with respect to 10 kHz. According to the Nyquist sampling theorem, a downsampling was adopted to reduce the memory requirements. Table 5.1 recalls the main parameters of the IM under analysis.

The validation was performed by comparing the model and prototype current patterns. In the prototype, the broken bar condition shown in Figure 5.2b was realized by drilling the rotor in correspondence to a bar, as shown in Figure 5.7b. It is worth to note that it was not a complete open-circuit, since even with an hole diameter larger than the bar width, some current still flows due to the undesired loss of insulation between the magnetic sheets caused by the drill bit.

The CNN deputed to fault detection analyses the current pattern during speed transients (start-up). Anyway, the start-up condition is very difficult to model due to the countless phenomena and spurious effects which afflict this transient. Therefore, a first comparison was carried out in steady-state conditions, by a simple Volt/Hertz control strategy.

The supply frequency was imposed at half the nominal speed. In order to appreciate the behaviour of the model under different saturation conditions, the voltage was varied to obtain a stator current vector equal to $I_n/3$ and $2/3I_n$. In case of healthy IM, the time behaviour of the currents with $|i_s| = 2/3I_n$ obtained experimentally and in simulation are reported in Figure 5.8. Even being only a qualitative comparison, it already gives an idea of the accuracy of the model, accurately replicating the experimental measurement.

A quantitative evaluation can be based on the analysis in the frequency domain, with focus in the current harmonics around the fundamental one. The FFT of the steady-state current $i_{s\alpha}$ in the two considered cases ($I_n/3$ and $2/3I_n$) returns the values reported in Table 5.2. Obviously, a perfect match is not expected, due to the several items that can affect the analysis, as for example little differences in the material permeability, slight errors in the motor dimensions, the disregard of the leakage flux in the stator back iron, and so forth. The added value of the present analysis is that it gives a hint of the bearable imprecision in the model that still ensures optimal performance in generating CNN traning patterns. The same comparison in case of faulty motor deserves some considerations. As previously mentioned, in the real prototype the interruption of the bar is not completely achieved. Therefore, it is very difficult to estimate the real degree of failure to impose in the simulation model to obtain the best match among the twos. Consequently, the same analysis for the broken motor has not been made, while a more qualitative comparison is reported in the

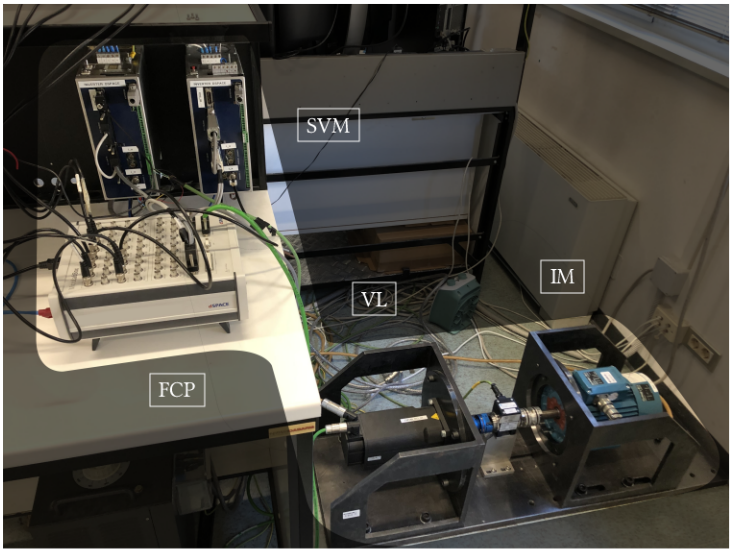

(a) Test bench.

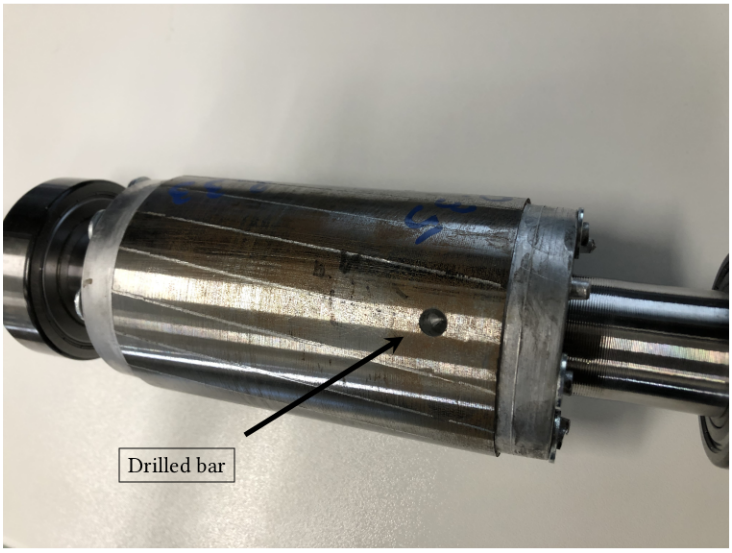

(b) Broken bar rotor.

Figure 5.7. The experimental test bench.

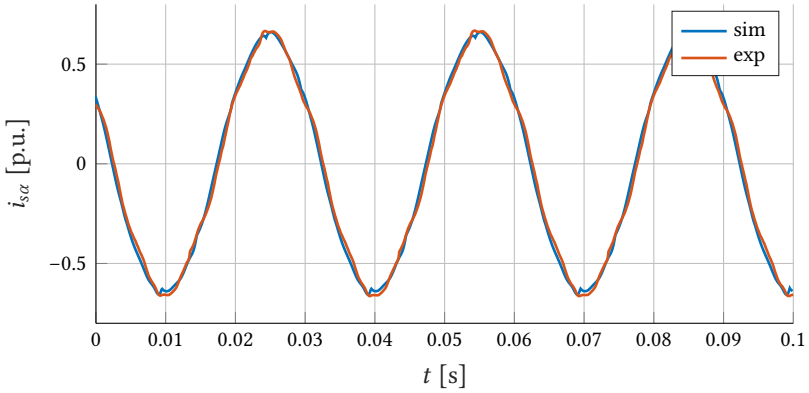

Figure 5.8. Experimental and simulated $i_{s\alpha}$ current in steady-state condition. Healthy motor.

Table 5.2. Main harmonics comparison. Healthy motor.

$\lvert i_s \rvert$	harmonic order	sim. ampl. [A]	exp. ampl. [A]
$I_n/3$	fundamental	3.1483	3.1483
	II	0.03476	0.05504
	III	0.02395	0.03
	IV	0.008562	0.01265
$2/3I_n$	fundamental	6.0937	6.0951
	II	0.03059	0.01405
	III	0.103	0.1053
	IV	0.02288	0.01383

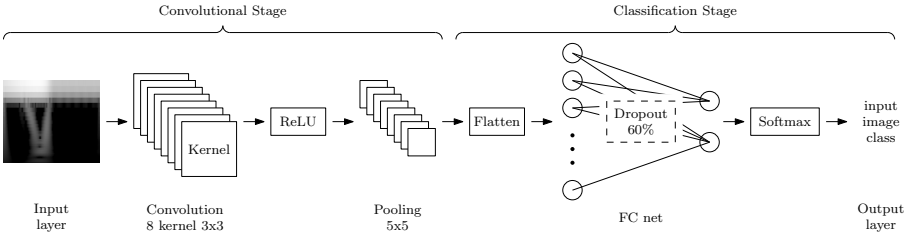

Figure 5.9. Architecture of the CNN used for broken bar detection in IM.

following.

As described in section 5.1.4, the CNN is trained on a Morse wavelet transform of the current transient, with the decomposition level equal to 36 covering the frequency range from 5 to 60 Hz. For the decomposition level meaning, see appendix C. In Figure 5.6 the CWTs obtained from the simulation model and experimental prototype in the healthy case are reported in figures 5.6a and 5.6b, while the same in the faulty case in figures 5.6c and 5.6d. In the faulty case, the CWT exhibits the typical V-pattern due to the fault-related harmonics, that are absent in case of an healthy motor. Comparing experimental and the simulation-based faulty CWTs it can be observed that they are very similar. A slight difference is only in terms of amplitude of the fault harmonic, as expected. Actually, while in the simulation a total loss of the bar conductivity is considered, in the experimental case this is not achieved and the fault harmonic is smaller (the V-pattern is less intense).

On one hand, it is to stress out that the validation of the model is important for a successful training of the CNN. On the other hand, this does not mean that the correspondence must be absolute. A certain degree of imprecision, as that shown in the present paragraph, is well tolerated by the network, that somewhat takes advantage on imprecise input to increase its classification capability.

5.3 *Convolutional neural network*

A CNN similar to that used in previous chapter 4 has been considered in this chapter. In the following the main differences are highlighted.

5.3.1 Architecture and training

The CNN architecture adopted for the interpretation of the CWT images, chasing the early defects in rotor bar conductivity, is graphically described in Figure 5.9. A design procedure that goes back and forth between hyperparameters and learnable parameters may be the most suitable way to achieve a satisfactory result as previously described in chapter 3. At first, it may appear either fuzzy or daunting with respect to conventional tuning algorithms. Nevertheless, there are some powerful tools, as those made available by Matlab [13], that let the designer to change quickly some parameters (as the number and size of convolution kernels and pooling), so that the entire design process can be sketched out in less than two days. The Matlab listing

used in this thesis for the design and training of the CNN is reported in following listing.

```
%% Layers
dropoutProb = 0.2;

layers = [
  imageInputLayer([100 100 1])

  convolution2dLayer([3 3], 8)
  reluLayer()
  maxPooling2dLayer([5 5])

  dropoutLayer(dropoutProb)

  fullyConnectedLayer(2)
  softmaxLayer()
  classificationLayer()];

%% Training options

opt = trainingOptions('sgdm', 'MaxEpochs', 30,
    'InitialLearnRate', 0.000001,
    'Plots','training-progress',
    'MiniBatchSize', 20,
    'ValidationData', valData,
    'ValidationFrequency', 10,
    'LearnRateSchedule', 'piecewise',
    'LearnRateDropPeriod', 6,
    'LearnRateDropFactor', 0.1);

%% Network training

[net, trainInfo] = trainNetwork(trainData, layers, opt);
```

Listing 5.1. Matlab code used for the design and training of the CNN.

In Figure 5.9, the convolutional stage is deputed to extract the "V-shaped" feature from the input image, while the classification stage performs the final choice, as function of the recognized feature. Some design hints are highlighted below.

- *Input image pre-processing* - While for constant supply frequency the CWT y-axis is constant too, the x-axis (i.e. time) depends on the duration of the transient, that can vary upon speed ramp settings and load conditions. In this work, a 100 × 100 input layer was fixed and the dimension of any CWT image was adapted accordingly, through a proper resizing. This operation is performed through a resampling of the original image according to the desired dimensions (100 × 100). The new samples of the image are obtained linearly interpolating the original ones. Moreover, the native double-precision CWT values were converted to a 8-bit greyscale. Thus, the total amount of memory required to store each single image was less then $10 kbytes$. These features were chosen through a trial and error approach as a trade off between memory and calculation requirements and the image resolution.
- *Convolution* - The input image is elaborated by a convolution through 8 kernels with a dimension of 3 × 3 [36].

- *ReLU and Pooling* - Among popular nonlinear activation functions, the ReLU has been preferred for its simplicity and widespread use in deep neural networks, especially in image processing tasks. ReLU's output is the maximum between the input and zero, which is easy to compute. The max-pooling operation (with size 2x2) mainly provides a spatial dimension reduction technique and its role is not as critical [3].
- *Output flattening and dropout* - The output of the convolutional stage is then flattened as required by the subsequent FC network. The FC net connects all the outputs of the convolution to only two neurons that represent the probability of the input image to belong to either an healthy or faulty motor. An additional feature, called *dropout*, has been added to the FC net. It consists in randomly drop units from the FC during training, along with their connections [102]. During the training, each neuron becomes more independent from the previous ones due to the dropped connections. The training becomes longer as the convergence to the optimal weights has been complicated but it results in a more general network. This has been shown to be effective against overfitting, which is an impending danger with limited training data available. The percentage of neuron dropout was selected at 60%.
- *Classification through Softmax* - The Softmax function takes as input a vector of K real numbers (the output of the FC network), and normalizes it into a probability distribution composed of K probabilities proportional to the exponentials of the input numbers. Therefore, it returns as output the class of health conditions with the highest probability.

5.4 *Convolutional neural network training and experimental results*

While the potentiality of a CNN is directly related to its architecture, the achievement of good performances relies on the training dataset. The training is the most challenging aspect in bridging a sophisticate AI-based technique to the world of AC drives, which is relatively simple and with very few examples of broken motors to be used as training data (e.g. compared to huge datasets of animals). This work mainly addressed this obstacle and in this direction a great help is offered by data augmentation methods, which pursue the artificial increase of the available dataset. In this work the concept was carried to the extreme, as the entire training was based on an artificial, model-based dataset.

Two output classes were considered, namely healthy or faulty motor. As regards the former, the model of Figure 5.1 has been particularized for the case of completely healthy IM and with a small percentage of failure, obtained by imposing a 10% reduction of the due current in the broken bar. Similarly, for the faulty class the model of Figure 5.1 was fitted with other two magnetic maps, featuring the 90% and 100% of reduction of the due current in the bar, respectively. This introduces some degree of fault tolerance, which can be graduated depending on the specific application requirement.

For each of the aforementioned four conditions, four different transients were simulated, and namely a nominal voltage direct start-up, a three equally-spaced voltage

steps up to the nominal value, a voltage ramp and the start-up of the motor through a soft-starter, with a limitation on the stator current to three times the nominal value I_n.

Different levels of inertia (from 1 to 10 of IM's own one), load torque (from 0 to the motor nominal one) and duration of the voltage ramp (from 0.5 s to 4 s) were used to generate the different cases of an artificial dataset of 2284 start-up transients. Random noise was added in each sample that composes the training dataset. Of these, 60% were used to train the network, while the remaining ones were equally split between validation and testing. The detailed functionality of these three datasets has already been explained in [36].

The 80 elements of the convolution kernels and the weights of the FC net were trained with the same approach already described in Figure 3.10 of chapter 3. An initial learning rate equal to 10^{-6} was used, that was then decreased to 10^{-7} after 6 epochs. The update of the weights by the back-propagation algorithm was performed not after the presentation of the single input image, but at the conclusion of the presentation of a group of them (a 20 images minibatch, in the present work). This stabilizes and speed-up the training process [36].

These design choices in the CNN training, obtained after many attempts in different directions, proved to be the best in relation to the early fault detection problem and on the dataset considered.

The ANN training is usually heavy and it can be done offline once and for all for any drive-motor pair. The trained ANN can be either made resident on a server that is fed by the current patterns (according to the Industry 4.0 paradigm) or implemented in the AC drive, bearing a certain amount of computational power. Being focused on the many innovative aspects of both the IM model and the CNN, this work meets the former case. The training was performed in the Matlab environment, on a PC featuring a GPU NVIDIA GeForce GTX1070 and it took about 5 minutes. Certainly, the latter solution would lead to a stand-alone drive, with the inherent ability of self-detecting the motor defects. In this perspective, the most demanding part is the post-elaboration of the transient pattern through the CWT algorithm. In any case, the Author believes that the solution is feasible, since the calculation can be part of the main control cycle, released from the rigid timing of the control routines, as an instantaneous evaluation of the motor status is not necessary.

The real accuracy of a classifier is in general hard to define, since it would theoretically imply the availability of an infinite number of experimental data. On the contrary, here the accuracy is necessarily based on a restricted set of available data obtained from healthy and damaged motors.

Specifically, in the real IM drive (Figure 5.7) 72 new current patterns during the IM start-up were acquired, half with the healthy motor and half with a broken bar rotor. Of them, 8 were direct start-ups at nominal voltage, 32 start-ups under voltage ramp and the remaining were generated by starting the IM with a soft-starter. For all these cases, the CWT was applied to the current patterns and the achieved 2-D images were downsampled according to the CNN input image dimension. The experimental dataset was given to the network in terms of new, never seen before samples to test its classification capabilities and it was able to correctly classify all of them (Figure 5.10). This remarkable result is due to (a) the stochastic nature of the CNN training (b) the data augmentation with artificial addition of white noise on the training dataset (c) a

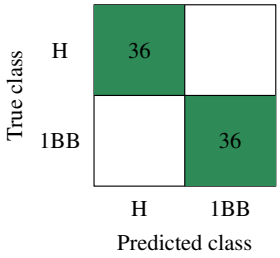

Figure 5.10. Confusion matrix obtained from the classification of the experiments through the CNN..

wide range of transient durations and load levels.

It is clear that the 100% of accuracy is not realistic. It is surely what it was obtained, but on relatively few never-seen-before test dataset. If a much larger experimental dataset was available, very likely this accuracy would decrease. Anyway, the result is surely informative on the quality of the proposed algorithm. From an industrial application perspective, one could consider starting with the proposed implementation and then exploiting the CNN's ability to self-improve, as will be discussed in the conclusive remarks.

5.5 *Conclusive remarks and possible developments*

An automatic classifier for the health recognition of a squirrel cage rotor, based on a convolutional neural network, has been described in this chapter. Several issues have been addressed, strictly related to the target of bridging the gap between the complex design of artificial neural networks and the world of electric drives, which is approaching the concepts of predictive maintenance with curiosity, sensing the advantages in terms of reliability and production efficiency.

From the experiments, some conclusions can be drawn:

- The use of Wavelet Transform as time vs. frequency analysis tool during start-up transients is accurate and avoids risks of miss-classifications due to slightly loaded, steady-state conditions.
- The CNN is reliable in recognizing the single broken bar in a never-seen-before real case. A single bar has been here considered as an early fault warning. The CNN has been trained to recognise also partially damaged bars, further graduating the CNN prediction.
- The innovative use of a tuned model to generate artificially all of the training sequences, taking to the limit the concept of data augmentation, has demonstrated to be a methodology that paves the way for the application of CNNs to the electrical drive industry, still poor in experimental series of data for training (as also demonstrated in chapter 3 for PMSMs).
- One key point is the reliability of the IM model. Perceptron neural networks can be surprisingly useful in the inversion of magnetic current-flux linkage maps obtained from FEA.

As a resume, the adopted design procedure for the proposed technique is sketched in the Algorithm 1 pseudocode.

Algorithm 1: Design procedure of the proposed fault recognition technique.

1. Creation of the FEA model of the motor and the relative ANN-based magnetic maps (Figure 5.2);
2. Setup of the IM model (Figure 5.1);
3. Simulation of several start-up transients and recording of the motor currents;
4. Application of the CWT algorithm for the realization of the CNN training dataset (Figure 5.6);
5. CNN design (Figure 5.9) and training in the Matlab environment;

Of course, the use of complex AI-tools as a means towards more-intelligent AC drives requires specific skills and good computational power, and there is still a lack of case studies. in particular, no guidelines for the initial design of the CNN were not available in the literature. As a contribution, it has been decided to include in this thesis work several hints and reasonings about the choices made during the long experimental stage. Another evident drawback is the time needed for the FEA setup, which also implies the availability of all IM constructive details and materials.

It is worth noticing that since the training of the CNN is based on simulated patterns, the proposed fault detection system can be categorized between the model-based fault detection methodologies. A first remarkable difference with respect to the existing one resides in the accuracy of the model, attained by using a complex multivariable function $\mathbf{g}$ (obtained through FEA). It represents a substantial improvement to the problem of model mismatches that affects the model-based methodologies.

Now let's come to the choice of using a CNN to classify the state of health of the IM. Since an accurate model is available, one could directly compare the simulation output with the experimental measurements to understand the health level of the motor. A direct, online comparison of the model output and the experimental data would require a simulation to be incorporated into the drive, with a high computational burden, often excessive for a standard AC Drive. Conversely, a trained CNN has proven to fairly manage the task, with an unpaired robustness, due to the large number of cases used for its training. Additionally, in an incremental learning perspective, the CNN can be continuously and automatically updated whenever new labelled samples are available. In this way a better tuning of the CNN on all the features and spurious behaviours not considered in the model but present in the real system is expected.

Finally, it is worth remembering that only the current acquisition is necessarily achieved online by the IM drive, while FEA, magnetic model inversion, CWT algorithm and CNN training can all be performed offline by a supervision software, according to the Industry 4.0 paradigm.

This work has been submitted and it is at the moment in press in the IEEE Journal of Emerging and Selected Topics of in Power Electronics [90].

6

SYNRM EKF-BASED SENSORLESS CONTROL

To further increase the reliability and to augment the fault tolerant characteristics of modern industrial drives, the sensorless control of a SynRM through EKF has included in my PhD studies. The proposal technique was individuated after a detailed analysis of the existing solutions, and in particular how they could match the specificity of the SynRMs.

Several methodologies for the sensorless position estimation of AC motors are present in literature. A recent review of them can be found in [114] and specifically for synchronous motors in [109] and [43]. Each sensorless algorithm can be classified as either a saliency-based or a model-based method. While the former is suitable for stationary or low-speed conditions [58, 69], the latter is preferable at high speeds. The full range can be obtained if the twos converge seamlessly into a complete sensorless control algorithm. These types of solutions are effective, but they often entail complex implementation and fine-tuning [20, 44, 107].

The saliency-based methods are usually based on high-frequency signal injection and measurement of the related motor response. They can provide an accurate estimation at low speeds, showing good immunity against dc offset and low-frequency noises. The acoustic noise can be mitigated by randomly modifying the injected signal, as proposed in [63]. However, the injection methods still have some drawbacks, including complexity, less operating voltage, higher core losses, and extra torque ripples. The research is now oriented towards the reduction of the injected signals to minimize audible noise and high-frequency losses, as described in [19].

Many applications in which the reluctance motor can compete with the induction motor do not require high starting torques. Clear examples include pumps and Heating Ventilation and Air-Conditioning (HVAC) drives, as well as wind turbines [9]. An alternative to the delicate full-range algorithms is the combination of a robust model-based technique with a simple I-f start-up algorithm, which allows the motor to operate at low speeds without either initial position estimation or machine parameters identification [1]. To exit the open-loop operations as soon as possible, it is advantageous to extend the validity of the model-based sensorless technique as far as possible towards low speeds [34], which was one of the primary goals of the present work.

Most popular model-based methods to reconstruct the rotor position were developed for PMSMs through the estimation of the b-EMF. Nonetheless, extending the sensorless techniques already pioneered for PMSM and Interior Permanent Magnet (IPM) to SynRM is not trivial, due to the marked magnetic nonlinearity [71].

The problem is well represented by [48], which proposes a control based on novel extended electromotive force models. The inclusion of magnetic saturation is done by

a complex online parameter estimation technique, that uses a pseudorandom sequence signals injection.

In general, the model-based sensorless methods of SynRMs can be categorized into Extended Electromagnetic Force (EEMF) based methods and Direct Flux Observer (DFO) based methods [64]. The formers are based on the tracking of extended b-EMF as in [48] or [83] in which a design method of the full-order EEMF observer is proposed. Methods based on DFO instead exploit voltage integration to estimate the direct flux position. A Phase Locked Loop (PLL) is effectively used for flux position estimation in [51].

A good and effective sensorless algorithm for synchronous motors is based on the EKF. Since its early applications to AC drives, it has shown excellent qualities as an optimal recursive estimation algorithm for non linear systems, and is very suitable in case of noisy measurements. [18, 98]. Unfortunately, the transposition to SynRMs is not straightforward. The first attempts date back to the early 2000s, which immediately highlighted the problems associated with magnetic saturation [98]. The complexity is evidenced by the few publications that followed that seminal article [9, 82], but a recent upswing indicates that the interest in this technique has not waned [65, 79, 119].

The main obstacles are the instability that the linearization around the working point can in a too-simple model and the derivative of Jacobian matrices, which is critical when the magnetic model is based on a piecewise-linear interpolation of LUTs [56]. A viable alternative can represented by the use of approximating functions, if one accepts non negligible estimation errors in some portion of the working region. Once again, it all comes down to the SynRM model.

In the frame of the use of AI to improve the next generation of electric drives, this chapter reformulates the EKF algorithm exploiting an innovative magnetic model, based on RBF-ANN, firstly proposed in [84]. This AI-based tool can be tuned offline to accurately describe the magnetic behaviour of the motor, including any self- and cross-saturation. But the distinctive feature is that it returns an analytical model, which guarantees differentiability of any order.

The typical implementation of the EKF on a synchronous motor neglects the saturation and assumes a linear magnetic model with nominal inductances. In other words, the model indicated with the red lines and previously described in chapter 1, Figure 2.4 is assumed. It is easy to understand that if this model is quite correct for small currents this is no longer true when the motor operates under heavy load conditions. Therefore, to properly deal with this, the model described in section 2.2 in equations (2.14) and (2.15) are used.

6.1 *Extended Kalman Filter*

For what concerns the mechanical model of the motor a "infinite inertia" hypothesis is adopted, i.e. the variation in speed within the control cycle T_s is assumed negligible. Therefore, it can be described with equations (6.1).

$$\frac{d\omega_{me}}{dt} = 0, \qquad \frac{d\vartheta_{me}}{dt} = \omega_{me} \tag{6.1}$$

The more traditional and simple choice of the state variable for the EKF implementation is chosen

$$\mathbf{x} = \left[i_\alpha, i_\beta, \omega_{me}, \vartheta_{me} \right]^T \tag{6.2}$$

of which $[i_\alpha, i_\beta]^T$ are directly measured on the drive. Combining equations (2.14) and (6.1) the total state-space non linear model of the SynRM can be derived

$$\begin{aligned} \dot{\mathbf{x}}(t) &= \mathbf{f}\left(\mathbf{x}(t), \mathbf{u}(t)\right) + \boldsymbol{\sigma}(t) \\ \mathbf{y}(t) &= \mathbf{h}\left(\mathbf{x}(t)\right) + \boldsymbol{\mu}(t) \end{aligned} \tag{6.3}$$

in which the measurements $\mathbf{y}(t)$ are the currents $\mathbf{i}_{\alpha\beta}$. While:

$$\begin{aligned} \mathbf{f} &= \begin{bmatrix} \mathbf{A}^{-1}\left(\mathbf{u}_{\alpha\beta} - \mathbf{R}\mathbf{i}_{\alpha\beta} - \omega_{me}\left(\mathbf{B}\mathbf{i}_{\alpha\beta} + \mathbf{C}\right)\right) \\ 0 \\ \omega_{me} \end{bmatrix} \\ \mathbf{h} &= \begin{bmatrix} 1 & 0 & 0 & 0 \\ 0 & 1 & 0 & 0 \end{bmatrix} \end{aligned} \tag{6.4}$$

This notation allows a direct application of the EKF theory and estimator, provided that the added system and measurement noises, $\boldsymbol{\sigma}(t)$ and $\boldsymbol{\mu}(t)$, are both zero-mean, white Gaussian noises with covariance $\mathbf{Q}_\sigma$ and $\mathbf{R}_\mu$ respectively. Moreover, these covariance matrices must be symmetric, positive semi-definite and independent from state $\mathbf{x}(t)$. All these hypothesis are assumed to be valid on the considered system.

The EKF is an optimal, stochastic estimator able to perform estimations on noisy systems. It implements a predictor-corrector estimator and it is optimal in the sense that it minimizes the estimated error covariance. Conversely to its linear version, the EKF is able to estimate the state of non linear systems hinging on a local linearisation for the update of the covariances.

Starting from a state-space model described as in (6.3) the discrete implementation of the EKF can be derived. The model is firstly discretized according to the control period T_s

$$\begin{aligned} \hat{\mathbf{x}}(k+1) &= \mathbf{f}\left(\hat{\mathbf{x}}(k), \mathbf{u}(k)\right) + \boldsymbol{\sigma}(k) \\ \mathbf{y}(k) &= \mathbf{h}\left(\mathbf{x}(k)\right) + \boldsymbol{\mu}(k) \end{aligned} \tag{6.5}$$

While $\mathbf{h}$ remains unchanged, henceforth with $\mathbf{f}$ is intended the discrete version of the model state space function. To synthesise, the time dependence is reported as subscript.

$$\mathbf{f} = \begin{cases} \begin{aligned} i_{\alpha,k+1} &= i_{\alpha,k} + T_s\gamma_{11,k}[u_{\alpha,k} - Ri_{\alpha,k} - \omega_{me,k}(b_{11,k}i_{\alpha,k} + b_{12,k}i_{\beta,k} + c_{\alpha,k})] + \\ &\quad + T_s\gamma_{12,k}[u_{\beta,k} - Ri_{\beta,k} - \omega_{me,k}(b_{21,k}i_{\alpha,k} + b_{22,k}i_{\beta,k} + c_{\beta,k})] \\ i_{\beta,k+1} &= i_{\beta,k} + T_s\gamma_{21,k}[u_{\alpha,k} - Ri_{\alpha,k} - \omega_{me,k}(b_{11,k}i_{\alpha,k} + b_{12,k}i_{\beta,k} + c_{\alpha,k})] + \\ &\quad + T_s\gamma_{22,k}[u_{\beta,k} - Ri_{\beta,k} - \omega_{me,k}(b_{21,k}i_{\alpha,k} + b_{22,k}i_{\beta,k} + c_{\beta,k})] \end{aligned} \\ \omega_{me,k+1} = \omega_{me,k} \\ \vartheta_{me,k+1} = \vartheta_{me,k} + T_s\omega_{me,k} \end{cases} \tag{6.6}$$

The Jacobians of functions $\mathbf{f}$ and $\mathbf{h}$ are evaluated on the actual working point k.

$$\mathbf{F}(k) = \left.\frac{\partial \mathbf{f}}{\partial \mathbf{x}}\right|_{\mathbf{x}=\hat{\mathbf{x}}(k)}, \qquad \mathbf{H}(k) = \left.\frac{\partial \mathbf{h}}{\partial \mathbf{x}}\right|_{\mathbf{x}=\hat{\mathbf{x}}(k)} \tag{6.7}$$

The $\hat{}$ operator is introduced to specify that in the implementation the real state is unknown and its estimate is used.

It is worth recalling that the coefficients γ depends on non linear inductance functions (2.16), (2.15) that are in turn obtained by derivation of the synchronous flux linkages $\boldsymbol{\lambda}_{dq}$. Starting from the knowledge of the currents vs fluxes relationship. the achievement of Jacobians (6.7) requires two orders of derivation. The first for obtaining the synchronous inductances, while the second to evaluate the Jacobian terms. It is easy to understand the overwhelming complexity of these calculations if the flux functions are not chosen properly. In keeping with the characters of this thesis, a RBF-ANN fitting function was used. The calculations for the achievement of Jacobians of (6.6) are reported in appendix D.

The algorithm is composed by two steps. The former is the *measurement update* (or correction) in which the estimation is corrected through the new measurement at point k (a posteriori estimation). The latter is called *time update* (or prediction) and consists in the estimation at step $k+1$ given the previously corrected estimate at step k (a priori estimation). They will be differentiated using respectively the temporal indexes $k|k$ and $k+1|k$.

The main operations performed at time kT_s are the following.

- *measurement update* (correction)

$$\begin{aligned}
\mathbf{H} &= \left.\frac{\partial \mathbf{h}}{\partial \mathbf{x}}\right|_{\mathbf{x}=\hat{\mathbf{x}}(k|k-1)} \\
\mathbf{K} &= \mathbf{P}(k|k-1)\mathbf{H}^T(\mathbf{H}\mathbf{P}(k|k-1)\mathbf{H}^T + \mathbf{R}_\mu)^{-1} \\
\hat{\mathbf{x}}(k|k) &= \hat{\mathbf{x}}(k|k-1) + \mathbf{K}\left[\mathbf{y}(k) - \mathbf{h}(\hat{\mathbf{x}}(k|k-1))\right] \\
\mathbf{P}(k|k) &= \mathbf{P}(k|k-1) - \mathbf{K}\mathbf{H}\mathbf{P}(k|k-1)
\end{aligned} \tag{6.8}$$

- *time update* (prediction)

$$\begin{aligned}
\hat{\mathbf{x}}(k+1|k) &= \mathbf{f}(\hat{\mathbf{x}}(k|k), \mathbf{u}(k)) \\
\mathbf{F} &= \left.\frac{\partial \mathbf{f}}{\partial \mathbf{x}}\right|_{\mathbf{x}=\hat{\mathbf{x}}(k|k)} \\
\mathbf{P}(k+1|k) &= \mathbf{F}\mathbf{P}(k|k)\mathbf{F}^T + \mathbf{Q}_\sigma
\end{aligned} \tag{6.9}$$

$\mathbf{K}$ represents the Kalman gains matrix evaluated at step k used to correct the state estimation through the innovation contribute $\mathbf{y}(k) - \mathbf{h}(\hat{\mathbf{x}}(k|k-1))$. The matrix $\mathbf{P}(k)$ represents the error covariances of each state variable.

The Kalman estimate is optimal provided that the covariance matrices $\mathbf{Q}_\sigma$ and $\mathbf{R}_\mu$ are properly tuned on the real system noises. They are typically chosen as diagonal matrices assuming that each state is only affected by its relative noise [17]. While the measurement covariance can be easily identified experimentally, during the commissioning of the drive, the estimation of $\mathbf{Q}_\sigma$ is not trivial and typically requires an iterative trial and error fine tuning. This approach was considered in this thesis.

6.2 *Radial Basis Function Neural Network*

The computation of the Jacobian $\mathbf{F}$ in (6.9) is relevant in deciding the feasibility of the EKF algorithm. Due to the strongly non linear magnetic behaviour included in

the model equations (2.14), the evaluation of $\mathbf{F}$ requires the estimation of the first and second order derivatives of the flux linkages shown in Figure 2.4. The former are directly employed, in form of differential inductances, in the implementation of equation (2.14) during the prediction step, while the latter are necessary as derivatives of these inductances in the determination of $\mathbf{F}$.

There is the need to estimate the fluxes as continuous and differentiable functions, at least up to the second order of derivation. An effective solution is represented by a description based on a RBF-ANN, as suggested in [84]. The model is based on an equally distributed neuron network which, elaborating the input currents $\mathbf{i}_{dq}$, estimates the output fluxes $\boldsymbol{\lambda}_{dq}$. Gaussian activation functions are used for each neuron and the synchronous fluxes $\boldsymbol{\lambda}_{dq}$ can be expressed as linear combination of exponential terms.

$$\boldsymbol{\lambda}_{dq} = \sum_{k=0}^{K} \mathbf{w}_k e^{-\left(\|\mathbf{i}_{dq}-\mathbf{x}_k\| b_k\right)^2} \tag{6.10}$$

The usage of a Gaussian activation function gives to each neuron a local characteristic, which means that if the input is sufficiently far from a neuron this last is not used in the determination of the network output. This distance is an Euclidean distance evaluated respect to each of the K neurons which compose the network. In other words, the distance between the input $\mathbf{i}_{dq}$ and the k-th neuron is represented by $\|\mathbf{i}_{dq} - \mathbf{x}_k\|$ in which $\mathbf{x}_k = \left[x_k^d, x_k^q\right]^T$ are the coordinates of the neuron. The distances are scaled by the coefficients b_k and passed through an exponential function. The results are then linearly combined according to the weights $\mathbf{w}_k = \left[w_k^d, w_k^q\right]^T$ to estimate the synchronous fluxes $\boldsymbol{\lambda}_{dq}$.

Clearly, the computational effort required by the assessment of equations (6.10) is heavier respect to the same evaluation through LUTs. Nonetheless, the realization by means of exponential functions guarantees differentiability at any order of derivation. Moreover, once the network weights are tuned offline is also possible to implement online only a reduced order Mac-Laurin approximation of the exponential, thus reducing the computational effort required by the algorithm.

Based on (6.10), the synchronous inductances can be easily evaluated as the following equations show.

$$\begin{aligned}
L_d &= \frac{\partial \lambda_d}{\partial i_d} = \sum_{k=0}^{K} -2\left(i_d - x_k^d\right) b_k^2 w_k^d e^{-\left(\|\mathbf{i}_{dq}-\mathbf{x}_k\| b_k\right)^2} \\
L_q &= \frac{\partial \lambda_q}{\partial i_q} = \sum_{k=0}^{K} -2\left(i_q - x_k^q\right) b_k^2 w_k^q e^{-\left(\|\mathbf{i}_{dq}-\mathbf{x}_k\| b_k\right)^2} \\
L_{dq} &= \frac{\partial \lambda_d}{\partial i_q} = \sum_{k=0}^{K} -2\left(i_q - x_k^q\right) b_k^2 w_k^d e^{-\left(\|\mathbf{i}_{dq}-\mathbf{x}_k\| b_k\right)^2}
\end{aligned} \tag{6.11}$$

Finally, applying the transformation (2.12), it is possible to express equations (6.10) and (6.11) as functions of stationary currents $\mathbf{i}_{\alpha\beta}$ with the aim to derivate them respect to the state $\mathbf{x}$ and evaluate Jacobian $\mathbf{F}$ as reported in appendix D. It is evident that, despite the computational load, the derivation of the flux linkages becomes straight-

Table 6.1. SynRM parameters.

Symbol	Parameter	Value
P_n	Nominal power	1600 W
U_n	Nominal voltage	400 V
I_n	Nominal current	4 A
p	Number of pole pairs	2
$\omega_{m,n}$	Nominal speed	1500 rpm
$L_{d,n}$	Nominal d inductance	380 mH
$L_{q,n}$	Nominal q inductance	85 mH

forward when this RBF model of the fluxes is considered. Once these are evaluated, the Jacobian $\mathbf{F}$ can be obtained.

The identification of the weights $\mathbf{w}_k$ and biases b_k which best fit the flux maps is carried out through a supervised training of the ANN. This procedure is based on the availability of a training dataset [39], in this case composed by a series of inputs $\mathbf{i}_{dq}$ and their relative outputs $\boldsymbol{\lambda}_{dq}$ that should span all the motor operating region. As previously done for the ANN in section 5.1.3, a Levenberg-Marquardt algorithm was chosen to evaluate the estimation error of the network on the training dataset and back-propagate it for updating the ANN weights.

From the implementation point of view, the training dataset was realized offline. Thanks to the availability of a test bench as that reported in Figure 6.1 and described in section 6.3, a set of couples $\mathbf{i}_{dq}$, $\boldsymbol{\lambda}_{dq}$ was acquired. The currents were explored from $-I_n$ to I_n with 19 points equally spaced along both dq axes, obtaining $19 \times 19 = 361$ points. Performing the steady-state measurements of currents, voltages and speed for each of these points the corresponding $\boldsymbol{\lambda}_{dq}$ set was obtained [11].

The RBF-ANN was then trained with this training dataset. After some attempts the best results were achieved using an ANN architecture with $14 \times 14 = 196$ neurons equispaced along the axes of the dq synchronous reference frame. Comparing the currents to fluxes maps obtained experimentally with the outputs given by the trained ANN a mean square error equal to $1.22 \times 10^{-6}\mathrm{V}^2\mathrm{s}^2$ while the absolute error evaluated for each $\mathbf{i}_{dq}$, $\boldsymbol{\lambda}_{dq}$ point was always below 1.24 % respect the nominal value.

6.3 *Experimental Results*

6.3.1 Test rig description

The experiments were performed on the test bench shown in Figure 6.1. The SynRM (Table 6.1) was speed-controlled through the sensorless feedback of the estimated state. A PMSM was mechanically coupled with the SynRM in a back to back configuration in order to emulate the effect of a load torque during the operation of the SynRM. Both the motors were actuated with two Voltage Source Converters (VSCs) connected to the same DC bus. The DC bus voltage value was 540 V and the switching frequency of the inverters equal to 8 kHz. The VSCs were controlled through a MicroLabBox

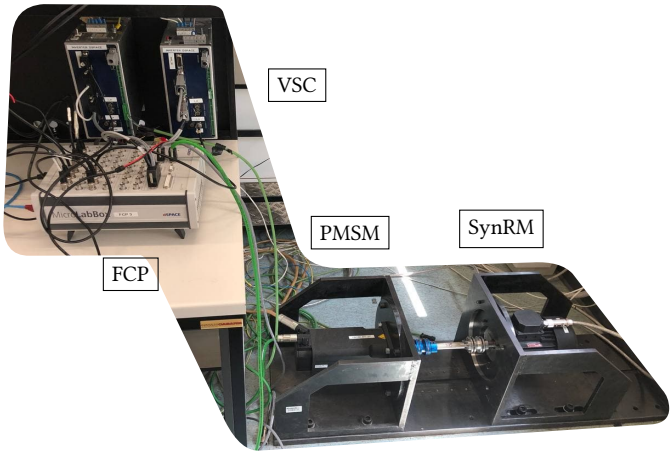

Figure 6.1. The experimental test bench.

dSpace FCP system.

The idea was to appreciate the effect of magnetic non linearities on the filter estimation and sensorless control of the SynRM. The dynamics of the inner current loops was maintained flat through an adaptive PI current control structure [7]. With this solution a constant bandwidth of the current control loop was guaranteed in each working condition. Therefore, the stability or instability of the sensorless control during the tests was ascribable to only the EKF performances and not to the variations of the current control dynamics. The PI gains were tuned to obtain 200 Hz bandwidth with 70° phase margin and 5 Hz bandwidth with 70° phase margin in the current and speed control loops respectively.

As is known, the EKF applied on SynRM suffers of observability issues [20, 106] when the motor flux is absent, i.e. when the motor is unloaded. In order to guarantee a widespread range of operability a modified Maximum Torque Per Ampere (MTPA) approach was considered (see Figure 6.2), limiting the d-axis current above 30% the nominal value. This was chosen as an arbitrary threshold. The experimental optimization of this value was not the aim of my study, but it would be advisable in an industrial application to maximize the drive efficiency.

Three types of EKF were considered whose performance comparison is the main target of this project.

- a standard implementation of the EKF using the nominal, linear magnetic model of the SynRM as those already present in literature (hereafter called Linear (Lin) EKF),
- an implementation which takes into account of magnetic non linearities (Non Linear (NL)) thanks to the knowledge of an accurate neural network-based magnetic model of the motor,
- an hybrid version of the previous twos, optimized from the execution time point of view (called Hybrid (Hy)).

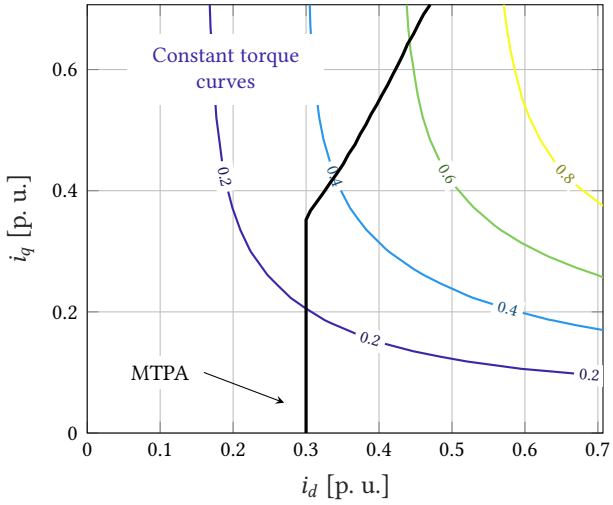

Figure 6.2. MTPA currents in the dq plane.

The first was the simpler, based on a nominal and linear magnetic model. Taking advantage of the RBF neural model a second version was considered which includes the magnetic non linearities of the motor.

It should be highlighted that, even though the ANN allows to easily estimate all grade derivatives of the fluxes, the equations to implement are quite complex. As it is known, the EKF tries to overcome the non linearity problem in two ways. On one hand, it hinges on the model knowledge for updating the state estimates. On the other hand, since the propagation of covariances consists in matrix calculations a linearised version of the model is considered.

Since some imprecision is tolerated in the covariance matrix, and given the heavy computational load for estimating the Jacobian components, a novel hybrid solution was evaluated. It was based on the complete RBF magnetic model for the state estimation, while it considered a simplified model for the propagation of the covariances. In other words, during the estimation of $\mathbf{F}$ the saturation of inductances was neglected and the nominal model was considered.

Although the complete non-linear proposal is theoretically more correct, the hybrid solution becomes very interesting from the implementation point of view. As a matter of fact, the formulation of Jacobians taking into account of non-linear magnetic effects is quite complex and requires many operations during the cycle time. An overrun condition can easily occur if the control time is slightly reduced or if the algorithm is not accurately optimized. The features of the considered three versions of the EKF are resumed in Table 6.2. In the table, the linear or non-linear characteristic means whether the dependence of $\mathbf{L}_{dq}$ on the motor currents were neglected or not during the prediction or the evaluation of the Jacobian. Each of the three EKFs were experimentally tuned through a trial and error approach optimizing the state estimation over the whole operating region of the motor. Although some differences

Table 6.2. EKF types and relative features.

Symbol	Name	Prediction $\mathbf{L}_{dq}(\mathbf{i}_{dq})$	Jacobian $\mathbf{F}$
Lin	Linear	Linear	Linear
Hy	Hybrid	Non-Linear	Linear
NL	Non-Linear	Non-Linear	Non-Linear

were expected due to the different precision on the motor model, the experimental KF tuning leads to the same optimal covariance matrices for all the three filter versions which were $\mathbf{Q}_\sigma = diag(1, 1)$ and $\mathbf{R}_\mu = diag(0.01, 0.01, 0.1, 1e^{-10})$.

6.3.2 Comparison of the three EKF solutions - Pullout curve test

The different EKFs performances were tested on a very demanding pull-out curve. This was arbitrarily chosen with the aim of stressing out the sensorless control capabilities of the different EKF algorithms. Figure 6.3 reports the speed and torque references for the SynRM and PMSM respectively. The transient lasts 12 s, in which the speed gradually changes from 50%, to 100% and finally to 15% of the nominal value, while the torque goes from 0 p.u. to 0.95 p.u.

The aim was to get an insight of the operative range of the motor. Clearly, as theory demonstrates [20], very low speed functioning is not feasible. In this operating point an alternative injection-based sensorless algorithm is mandatory in an industrial application. It is important that this threshold between the two sensorless methods (i.e. injection-based or EKF) is as low as possible. In the experiments, a satisfactory lower limit for the speed at full load was set to 15% of the nominal value.

The results obtained on the experimental rig driven by the reference of Figure 6.3 with the SynRM speed control closed on the linear, hybrid or non-linear EKF are reported in Figure 6.4, 6.5 and 6.6 respectively.

At the beginning of the transient ($t \leq 1$ s) the motor was rotating at half the nominal speed and it was unloaded ($\tau_L = 0$). These are quite favourable conditions for the EKF estimator and no particular critical behaviours are expected. Moreover, the motor currents are quite low. In this case also the linear EKF behaves well since the nominal model quite corresponds with the actual one. Nonetheless, even in this uncritical situation, observing the position estimation error ($\epsilon_{\vartheta_m} = \hat{\vartheta}_m - \vartheta_m$), a better behaviour of the hybrid and non-linear filters is remarkable. The position error goes from a medium error of -2.2° for the linear EKF to quite -0.6° for the other versions.

Some minor differences can be pointed out but all the three versions work properly during the speed transient up to $\omega_{m,n}$ with no load applied.

The magnetic model knowledge forcefulness is as more valuable as the level of motor currents increases due to the growing in the load torque. In this circumstance the motor inductances saturate, the linear EKF model is substantially different respect to the actual one and the estimation error diverges. Even with a time-consuming fine tuning of the covariance matrices, a successful accomplishment of the entire transient managed by the linear EKF estimates was not achieved. In steady-state conditions,

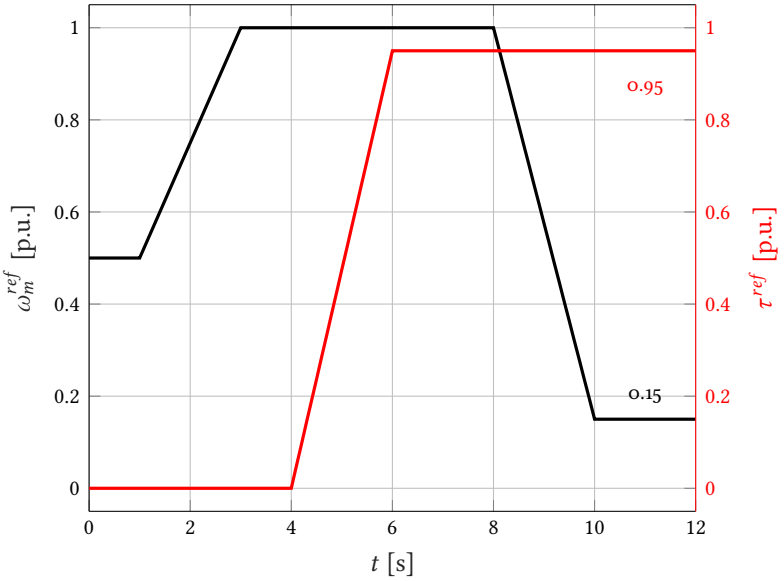

Figure 6.3. Speed and torque references used during the tests of the three different EKF sensorless controls.

Table 6.3. Turnaround times.

Symbol	EKF type	Turnaround time
Lin	Linear	27 µs
Hy	Hybrid	79 µs
NL	Non-Linear	108 µs

the maximum level of load torque the SynRM was able to bear with the linear EKF was about the 45 %.

The situation was far better with the hybrid and non-linear solutions. Albeit some little differences on the estimate noisiness and errors, the hybrid and non-linear EKFs behaved the same, as regard the stability.

6.3.3 Comparison of the three EKF solutions - Execution time collation

An additional information which could help in determining the best EKF choice for the speed sensorless control of a SynRM is the execution time. This value was evaluated as the total amount of time required to complete the control algorithm during a cycle period. It includes not only the EKF calculations but also the control algorithm and the measurement procedure.

Table 6.3 reports the execution time for the three EKF versions. The simple EKF with nominal, linear magnetic model on the considered test bench takes 27 µs. If a

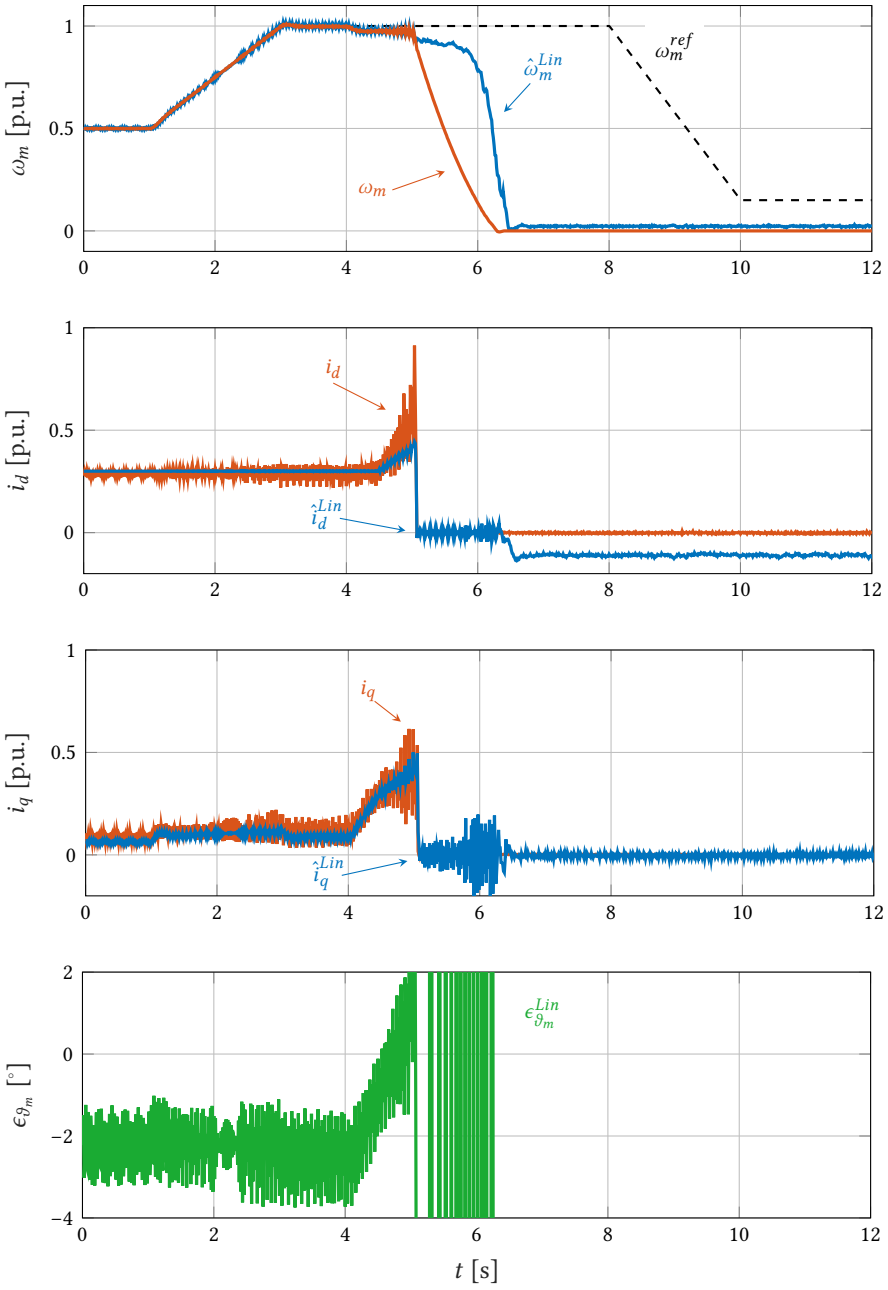

Figure 6.4. Experimental results. Linear EKF.

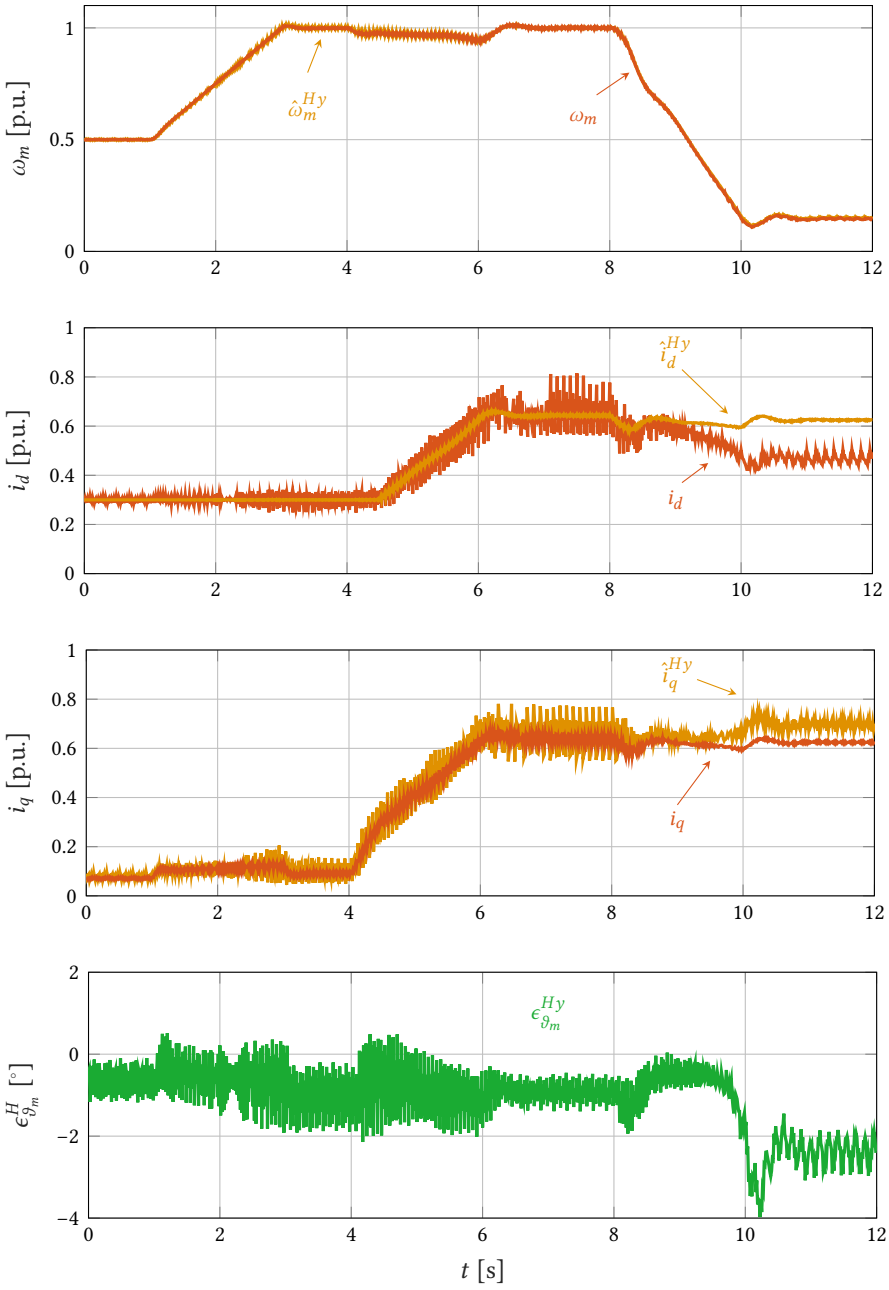

Figure 6.5. Experimental results. Hybrid EKF.

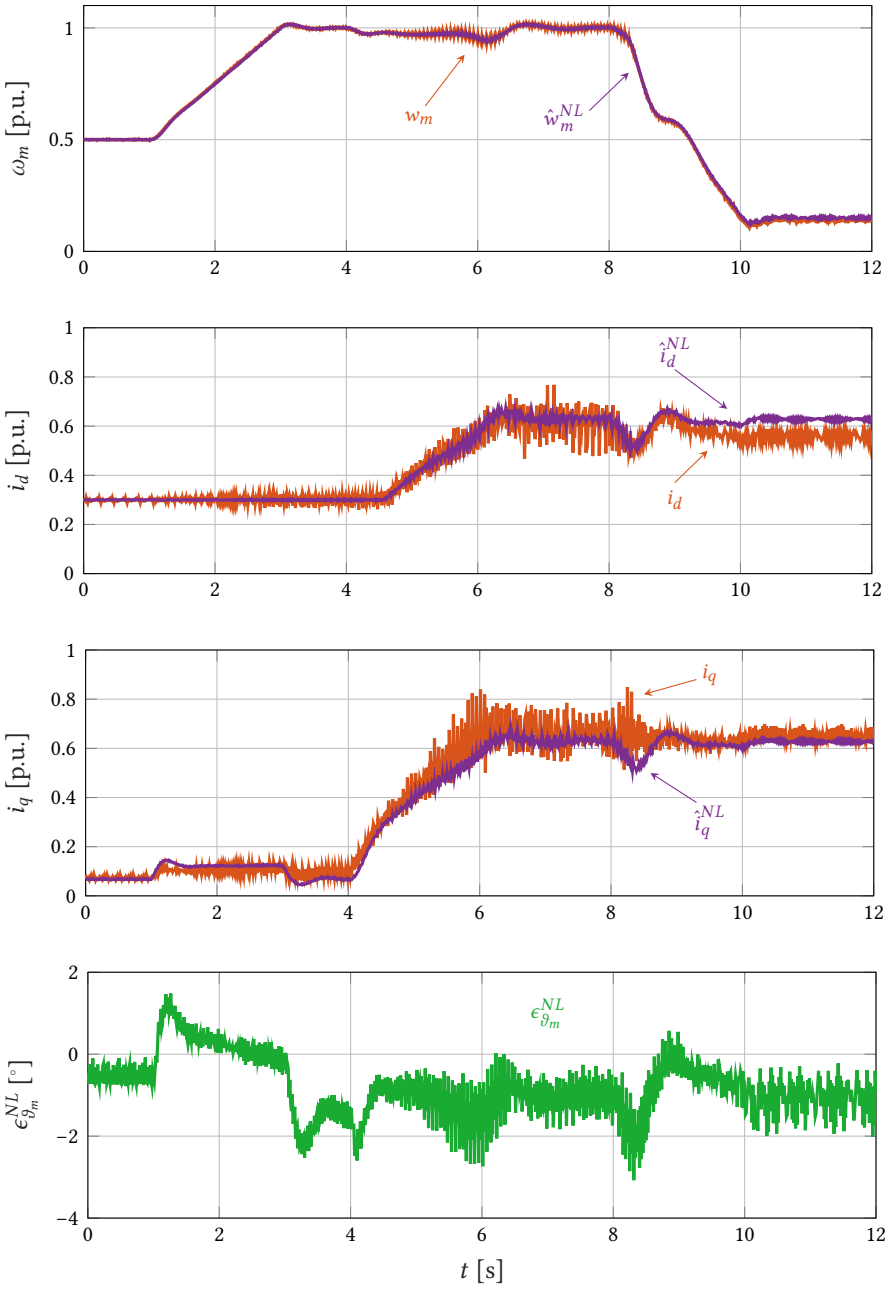

Figure 6.6. Experimental results. Non linear EKF.

comprehensive description of the non linear magnetic model through a RBF-ANN is included an almost prohibitive algorithm is obtained. An increase of 300 % of the execution time in the experimental rig was recorded. It is worth noticing that the control period was $T_s = 125\,\mu s$ and therefore the EKF with non linear magnetic model wasted almost all the available period. A better compromise was reached with the hybrid EKF solution that takes 79 µs (vs 108 µs of the full-non linear EKF).

6.4 *Conclusive remarks*

A comprehensive experimental verification of an EKF-based sensorless control for SynRMs has been reported in this chapter. In order to properly understand and deal with the critic factors of the system three different EKF versions have been proposed. Firstly, the standard EKF for synchronous motors is considered and in particular, a linear magnetic model is assumed. This is the simpler solution, directly inherited from PMSM applications. Nonetheless, the experimental measurements show that the linear magnetic model assumption on a strongly non linear motor heavily limits the stability of the system. Perhaps that is the reason for EKF's lack of success for the time being. It is clear that in order to obtain reasonable performance for all the motor working region a method able to consider of magnetic non linearities is needed.

A solution has been found in the accurate modelling of these non-idealities through a RBF-ANN avoiding the augmentation of the state for the estimation of motor fluxes and inductances. Thanks to this, a very precise EKF model was achieved. Although the provided solution already solves the problem of operating at full torque and speed, the sensorless algorithm is still very time-consuming.

Therefore, an hybrid version of the previous two EKFs has been finally introduced in this chapter which leads to a reduction of the computational effort maintaining the enhanced operability range. Proper experimental results and measurements are reported to validate the provided assertions.

This research activity is not yet neither published nor under revision, but it will be made pubblic in the coming months.

CONCLUSIONS

The climate change requires rapid and deep counteractions. Recent national and international policies are leading to an industrial world more efficient, reliable and safe. Tailoring these concepts to the electric drives field, this thesis proposes a modern and innovative study based on AI tools. In this context, CNNs have been applied and experienced as valid expert predictors of the health conditions of different AC motors. The application of these intelligent tools is surely inline with the modern trends of Industry 4.0 and Internet of Things. As a matter of fact, the connectivity and share of data that are typical of these development guidelines surely facilitate the implementation of neural networks also to the electric machines. The implementations reported in this thesis are intended to work offline, in a dedicated server, to which the online measurements from the motor are sent. In a near future, it is probable that an increased computational power will allow an online implementation of all the proposed algorithms.

The interturn short circuit and the demagnetization where considered for PMSMs, while the broken bars for IMs. The avoidance of potential additional sensors in these industry-oriented drives was chosen as cornerstone of the presented predictive maintenance projects. Although during the collaboration reported in chapter 4 also the stray flux has been studied, I tried to preferentially develop condition monitoring systems based on the analysis of the motor currents. This because any modern drive is already provided of the current sensor and as it can be chosen as common index for the recognition of different failure conditions.

The standard approach for the realization of the training dataset for the CNN would require the collection of several current patterns from both healthy and faulty motors and in different load and speed conditions. This unaffordable method makes the application of this type of AI tool in the electric drives field still unpracticable. In order to enhance the feasibility of these condition monitoring systems a completely new approach has been investigated in this thesis. This was the completely artificial generation of the entire training dataset through some accurate models of the motors. The networks trained on them have shown to perform optimally. When the models were not available or they were not adequately precise, the application of different and tailored DA techniques for the training dataset enhancement has shown to strongly increase the accuracy of the final predictor and these results have been highlighted throughout the thesis.

It is confirmed that a general method for the design of the CNN architecture cannot be achieved. As a further contribute to the research world, the reported implementations are quite similar and the rule of thumbs and design hints reported in the thesis can be a valid tool for development of new CNNs able to recognize other types of

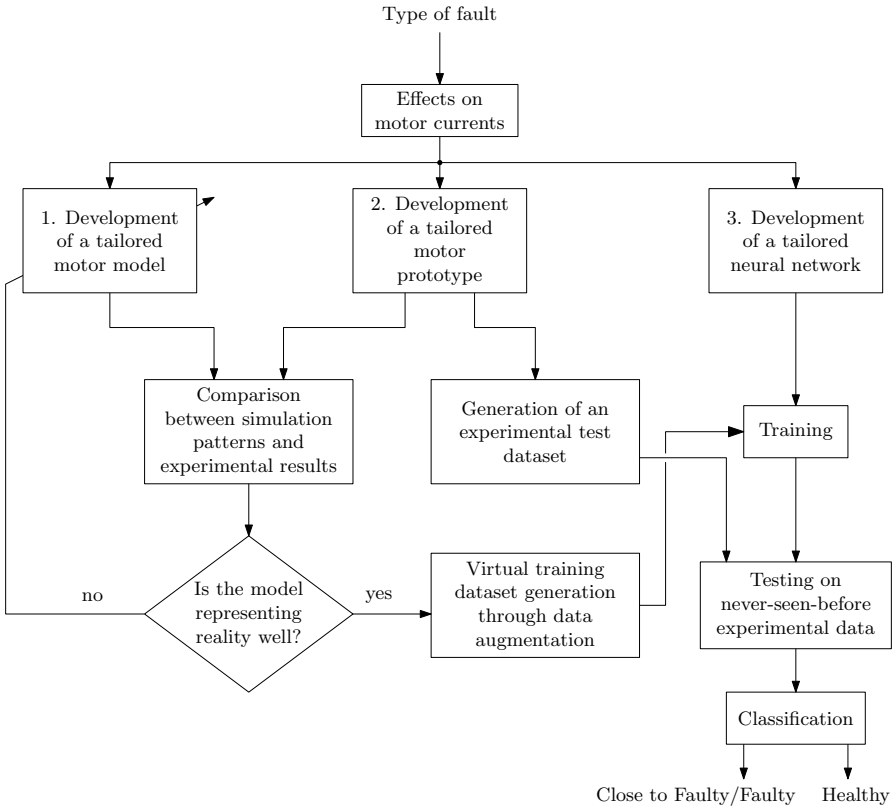

Figure 6.7. Design procedure of the CNN predictor developed in this thesis..

faults or applicable to other motors. In Figure 6.7 is reported a summary scheme of the adopted procedure for the design of a CNN-based fault monitoring system for AC electric motors.

Additionally, the knowledge-based identification of motor non linearities through ANNs has also been exploited successfully for the realization of a sensorless control algorithm for SynRMs. The topic has been studied as it represents an important step for the efficiency (usage of more efficient SynRMs) and reliability (avoidance of fault-prone position sensors). The standard implementation of the EKF has been modified with two novel proposals: a completely non linear and an hybrid one. This last one has been finally chosen as best as it gives the same stability performance, while limiting the computational load of the control algorithm.

All the results have been validated through extensive simulations and experimental stages in the Electric Drives Laboratory in Vicenza (EDLabVI).

Although very relevant results have been already obtained and described in this thesis, there is surely a lot to do in the next future. Something has been done for the simultaneously recognition of different faults, but a comprehensive and complete fault recognition system able to manage also the remaining failures has not been

developed yet. The optimized design of the CNN structure and implementation on an industrial micro-controller is certainly another relevant issue that up to date research has to face.

Finally, a self-tuning for the EKF applied to SynRM would conclude the transition to an autonomous, more intelligent generation of electric drives.

A

SOLUTION OF THE INTEGRAL FOR DETERMINING FLUX HARMONICS IN A DEMAGNETISED PMSM

The mathematical passages for the determination of the additional flux harmonics created by the demagnetization of a PMSM (3) are here reported. The analysis starts from equation (3.6) which is here recalled for convenience.

$$\lambda_a^{mg}(\theta_m) = \sum_{i=0}^{p_w-1}\sum_{n=1}^{\infty}\sum_{k=0}^{\infty} k_w \hat{B}_{g_n}\alpha_k \frac{DL}{4}\cdot \int_{-\frac{\pi}{2p_w}+\frac{2\pi i}{p_w}}^{\frac{\pi}{2p_w}+\frac{2\pi i}{p_w}} \cos\left[(np-k)(\theta_s-\theta_m)\right] - \cos\left[(np+k)(\theta_s-\theta_m)\right] d\theta_s \tag{A.1}$$

Solving the integral, one can obtain:

$$\begin{aligned}\lambda_a^{mg}(\theta_m) = \sum_{i=0}^{p_w-1}\sum_{n=1}^{\infty}\sum_{k=0}^{\infty} k_w \hat{B}_{g_n}\alpha_k \frac{DL}{4}\Bigg\{ & \frac{1}{np-k}\left[\sin\left((np-k)\left(\frac{\pi}{2p_w}+\frac{2\pi i}{p_w}-\theta_m\right)\right)\right. \\ & \left. -\sin\left((np-k)\left(-\frac{\pi}{2p_w}+\frac{2\pi i}{p_w}-\theta_m\right)\right)\right] \\ & -\frac{1}{np+k}\left[\sin\left((np+k)\left(\frac{\pi}{2p_w}+\frac{2\pi i}{p_w}-\theta_m\right)\right)\right. \\ & \left. -\sin\left((np+k)\left(-\frac{\pi}{2p_w}+\frac{2\pi i}{p_w}-\theta_m\right)\right)\right]\Bigg\}\end{aligned} \tag{A.2}$$

Each term is expanded to see if any simplification is possible. Let's denote the sine terms in (A.2) as s_1, s_2, s_3 and s_4.

$$\begin{aligned} s_1 &= \sin\left[(np-k)\left(\frac{\pi}{2p_w}+\frac{2\pi i}{p_w}-\theta_m\right)\right] \\ s_2 &= \sin\left[(np-k)\left(-\frac{\pi}{2p_w}+\frac{2\pi i}{p_w}-\theta_m\right)\right] \\ s_3 &= \sin\left[(np+k)\left(\frac{\pi}{2p_w}+\frac{2\pi i}{p_w}-\theta_m\right)\right] \\ s_4 &= \sin\left[(np+k)\left(-\frac{\pi}{2p_w}+\frac{2\pi i}{p_w}-\theta_m\right)\right] \end{aligned} \tag{A.3}$$

They can be expanded by applying repeatedly the trigonometric sum and difference identities. For example, considering s_1 it gives:

$$\begin{aligned}
s_1 &= \sin\left[(np-k)\frac{\pi}{2p_w} + (np-k)\frac{2\pi i}{p_w} - (np-k)\theta_m\right] \\
&= \sin\left[(np-k)\frac{\pi}{2p_w} + (np-k)\frac{2\pi i}{p_w}\right]\cos\left[(np-k)\theta_m\right] \\
&\quad - \cos\left[(np-k)\frac{\pi}{2p_w} + (np-k)\frac{2\pi i}{p_w}\right]\sin\left[(np-k)\theta_m\right] \\
&= \sin\left[(np-k)\frac{\pi}{2p_w}\right]\cos\left[(np-k)\frac{2\pi i}{p_w}\right]\cos\left[(np-k)\theta_m\right] \\
&\quad + \cos\left[(np-k)\frac{\pi}{2p_w}\right]\sin\left[(np-k)\frac{2\pi i}{p_w}\right]\cos\left[(np-k)\theta_m\right] \\
&\quad - \cos\left[(np-k)\frac{\pi}{2p_w}\right]\cos\left[(np-k)\frac{2\pi i}{p_w}\right]\sin\left[(np-k)\theta_m\right] \\
&\quad + \sin\left[(np-k)\frac{\pi}{2p_w}\right]\sin\left[(np-k)\frac{2\pi i}{p_w}\right]\sin\left[(np-k)\theta_m\right]
\end{aligned} \tag{A.4}$$

The same holds for s_2, s_3 and s_4. The following expansions are obtained.

$$\begin{aligned}
s_2 &= -\sin\left[(np-k)\frac{\pi}{2p_w}\right]\cos\left[(np-k)\frac{2\pi i}{p_w}\right]\cos\left[(np-k)\theta_m\right] \\
&\quad + \cos\left[(np-k)\frac{\pi}{2p_w}\right]\sin\left[(np-k)\frac{2\pi i}{p_w}\right]\cos\left[(np-k)\theta_m\right] \\
&\quad - \cos\left[(np-k)\frac{\pi}{2p_w}\right]\cos\left[(np-k)\frac{2\pi i}{p_w}\right]\sin\left[(np-k)\theta_m\right] \\
&\quad - \sin\left[(np-k)\frac{\pi}{2p_w}\right]\sin\left[(np-k)\frac{2\pi i}{p_w}\right]\sin\left[(np-k)\theta_m\right]
\end{aligned} \tag{A.5}$$

$$\begin{aligned}
s_3 &= \sin\left[(np+k)\frac{\pi}{2p_w}\right]\cos\left[(np+k)\frac{2\pi i}{p_w}\right]\cos\left[(np+k)\theta_m\right] \\
&\quad + \cos\left[(np+k)\frac{\pi}{2p_w}\right]\sin\left[(np+k)\frac{2\pi i}{p_w}\right]\cos\left[(np+k)\theta_m\right] \\
&\quad - \cos\left[(np+k)\frac{\pi}{2p_w}\right]\cos\left[(np+k)\frac{2\pi i}{p_w}\right]\sin\left[(np+k)\theta_m\right] \\
&\quad + \sin\left[(np+k)\frac{\pi}{2p_w}\right]\sin\left[(np+k)\frac{2\pi i}{p_w}\right]\sin\left[(np+k)\theta_m\right]
\end{aligned} \tag{A.6}$$

$$\begin{aligned} s_4 = &- \sin\left[(np+k)\frac{\pi}{2p_w}\right]\cos\left[(np+k)\frac{2\pi i}{p_w}\right]\cos\left[(np+k)\theta_m\right] \\ &+ \cos\left[(np+k)\frac{\pi}{2p_w}\right]\sin\left[(np+k)\frac{2\pi i}{p_w}\right]\cos\left[(np+k)\theta_m\right] \\ &- \cos\left[(np+k)\frac{\pi}{2p_w}\right]\cos\left[(np+k)\frac{2\pi i}{p_w}\right]\sin\left[(np+k)\theta_m\right] \\ &- \sin\left[(np+k)\frac{\pi}{2p_w}\right]\sin\left[(np+k)\frac{2\pi i}{p_w}\right]\sin\left[(np+k)\theta_m\right] \end{aligned} \tag{A.7}$$

Considering the expansion to (A.2) the following subtractions are of interest:

$$\begin{aligned} s_1 - s_2 &= 2\sin\left[(np-k)\frac{\pi}{2p_w}\right]\cos\left[(np-k)\frac{2\pi i}{p_w}\right]\cos\left[(np-k)\theta_m\right] \\ &\quad + 2\sin\left[(np-k)\frac{\pi}{2p_w}\right]\sin\left[(np-k)\frac{2\pi i}{p_w}\right]\sin\left[(np-k)\theta_m\right] \\ &= 2\sin\left[(np-k)\frac{\pi}{2p_w}\right]\left\{\cos\left[(np-k)\frac{2\pi i}{p_w}\right]\cos\left[(np-k)\theta_m\right]\right. \\ &\quad \left. + \sin\left[(np-k)\frac{2\pi i}{p_w}\right]\sin\left[(np-k)\theta_m\right]\right\} \end{aligned} \tag{A.8}$$

$$\begin{aligned} s_3 - s_4 &= 2\sin\left[(np+k)\frac{\pi}{2p_w}\right]\cos\left[(np+k)\frac{2\pi i}{p_w}\right]\cos\left[(np+k)\theta_m\right] \\ &\quad + 2\sin\left[(np+k)\frac{\pi}{2p_w}\right]\sin\left[(np+k)\frac{2\pi i}{p_w}\right]\sin\left[(np+k)\theta_m\right] \\ &= 2\sin\left[(np+k)\frac{\pi}{2p_w}\right]\left\{\cos\left[(np+k)\frac{2\pi i}{p_w}\right]\cos\left[(np+k)\theta_m\right]\right. \\ &\quad \left. + \sin\left[(np+k)\frac{2\pi i}{p_w}\right]\sin\left[(np+k)\theta_m\right]\right\} \end{aligned} \tag{A.9}$$

Now, substituting this differences (A.8) and (A.9) in (A.2), one obtains:

$$\begin{aligned}
\lambda_a^{mg}(\theta_m) &= \sum_{i=0}^{p_w-1}\sum_{n=1}^{\infty}\sum_{k=0}^{\infty} k_w \hat{B}_{g_n}\alpha_k \frac{DL}{4}\left\{\frac{1}{np-k}[s_1-s_2]-\frac{1}{np+k}[s_3-s_4]\right\} \\
&= \sum_{i=0}^{p_w-1}\sum_{n=1}^{\infty}\sum_{k=0}^{\infty} k_w \hat{B}_{g_n}\alpha_k \frac{DL}{4} \\
&\quad \left\{\frac{2}{np-k}\sin\left((np-k)\frac{\pi}{2p_w}\right)\right. \\
&\qquad \left[\cos\left((np-k)\frac{2\pi i}{p_w}\right)\cos\left((np-k)\theta_m\right)\right. \\
&\qquad \left.\left. + \sin\left((np-k)\frac{2\pi i}{p_w}\right)\sin\left((np-k)\theta_m\right)\right] \\
&\quad - \frac{2}{np+k}\sin\left((np+k)\frac{\pi}{2p_w}\right) \\
&\qquad \left[\cos\left((np+k)\frac{2\pi i}{p_w}\right)\cos\left((np+k)\theta_m\right)\right. \\
&\qquad \left.\left. + \sin\left((np+k)\frac{2\pi i}{p_w}\right)\sin\left((np+k)\theta_m\right)\right]\right\}
\end{aligned} \tag{A.10}$$

Simplifying and defining the coefficients:

$$\beta_{\pm k} = \frac{1}{np\pm k}\sin\left(\frac{(np\pm k)}{p_w}\frac{\pi}{2}\right). \tag{A.11}$$

equation (A.10) can be further simplified to

$$\begin{aligned}
\lambda_a^{mg}(\theta_m) = \sum_{i=0}^{p_w-1}\sum_{n=1}^{\infty}\sum_{k=0}^{\infty} k_w \hat{B}_{g_n}\alpha_k \frac{DL}{2}\Bigg\{ & \\
\beta_{-k}\left[\cos\left(\frac{2\pi i}{p_w}(np-k)\right)\cos\left((np-k)\theta_m\right)+\right. & \\
\left.\sin\left(\frac{2\pi i}{p_w}(np-k)\right)\sin\left((np-k)\theta_m\right)\right]- & \\
\beta_{+k}\left[\cos\left(\frac{2\pi i}{p_w}(np+k)\right)\cos\left((np+k)\theta_m\right)+\right. & \\
\left.\left.\sin\left(\frac{2\pi i}{p_w}(np+k)\right)\sin\left((np+k)\theta_m\right)\right]\right\} &
\end{aligned} \tag{A.12}$$

which is equal to equation (3.7) used in chapter 3.

B

SHORT TIME FOURIER TRANSFORM

The operating principle of STFT comes from the same theory of the classical Fourier transform, thus is used to analyse the steady state frequency behaviour of a windowed part of a signal. Different types of window can be applied.

In order to perform its discrete version, there are two parameters that have to be properly design: the time resolution T_s and frequency resolution F. The former, is directly related to the sampling frequency $f_s = 1/T_s$, specifies the maximum frequency that can be analysed through the Fourier transform according to the Nyquist theorem. The latter is directly related to the time length T of the signal on which the transform is applied. The frequency resolution of the obtained transform is equal to $F = 1/T$. As it is known, during the acquisition of a signal for this purpose, the parameters f_c and T must be properly chosen as trade-off between time and frequency resolution and the memory requirements for the storage of the signal. In online implementations also the computational cost is surely another important parameter for the design.

Generally, the entire signal is elaborated and the analysis returns correct results only if the signal is acquired in steady-state conditions. No information about the evolution of the frequency spectrum during time is provided.

The main idea of the STFT is to subdivide the original signal $x(t)$ in different equal parts and to perform a FFT on them [37]. The results are as many FFT as the number of parts in which the original signal is subdivided, thus obtaining a mean of analysing the evolution of the spectrum in time (Figure B.1).

Defining as $x(t)$ the signal and $w(t)$ the rectangular transform window (Figure B.1), the continuous STFT can be evaluated as follows.

$$X(\tau, f) = \int_{-\infty}^{\infty} x(t) w(t - \tau) e^{-j2\pi f t} dt \tag{B.1}$$

Its discrete version [59] is implemented by:

$$X(\tau, n) = \sum_{k=0}^{L-1} x(k) w(k - \tau) e^{-2\pi j n k / L} \tag{B.2}$$

in which L represents the length of the τ-th part of the original signal.

The output $X(\tau, n)$ is a function of two variables: the discrete time τ and the discrete frequency n. A typical way to appreciate its magnitude values in an informative and effective figure is the plot of the module of the transform values when varying frequency n and time τ along the ordinate and abscissa axes, respectively. This is called spectrogram or waterfall plot. The spectrogram of the stray flux measurements were used as fault index in the project described in chapter 4.

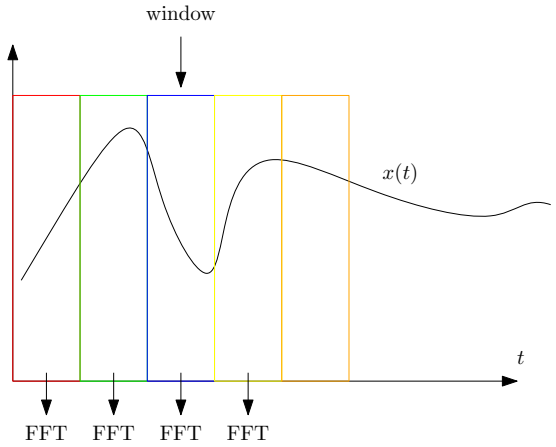

Figure B.1. Graphical example of the subdivision of a signal $x(t)$ for the implementation of a STFT.

The algorithm has a $O(nlogn)$ complexity. A particularly intuitive way of appreciating the resolution issues and differences between different types of decomposition is to look at the so-called "Heisenberg boxes" in the Phase Plane. The purpose of these boxes is to illustrate uncertainty principle governing the multi-resolution analysis, according to which the frequency and time of a signal at a specific instant cannot be known exactly. Instead, there is a trade-off between the resolution in time and in frequency, resulting in an area of ambiguity on a time-frequency graph. On the so-called Phase Plane, indeed, time is located on the horizontal axis, whereas frequency is on the vertical axis. Some examples are shown in Figure B.2. In Figure B.2a the raw signal is considered. It is composed by a series of samples in the time domain. Therefore, we have low uncertainties along time axis while no information is available for the frequency axis. The opposite case is when the Fourier transform is considered (Figure B.2b). In the STFT case, it is possible to reduce uncertainty in both axis but they are the result of a compromise among the two. The time resolution of the STFT is higher if the signal is divided in very small parts. Nonetheless, as observed for the traditional FFT (in this case applied to each part) the resolution in frequency is higher choosing longer parts. A graphical example of two extreme cases, in which the time or the frequency resolution is preferred, is reported in Figure B.2c and B.2d, respectively.

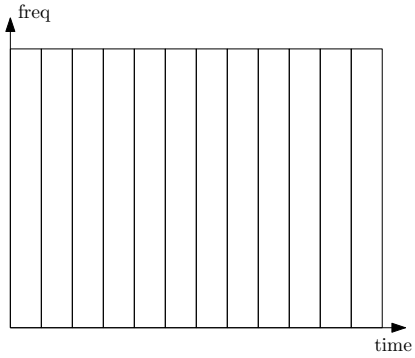

(a) Original signal resolution.

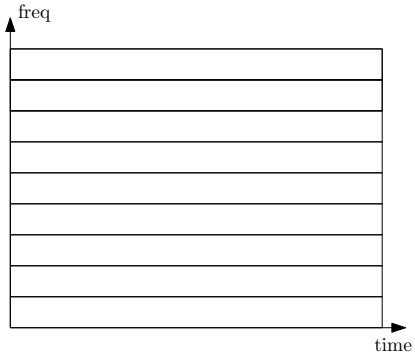

(b) Fourier transform resolution.

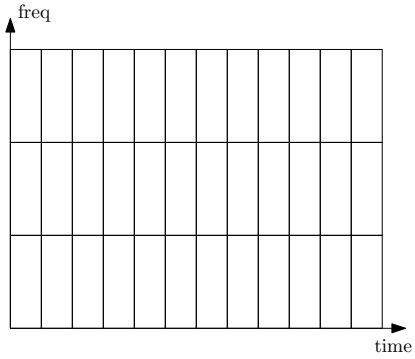

(c) STFT with high time but low frequency resolution.

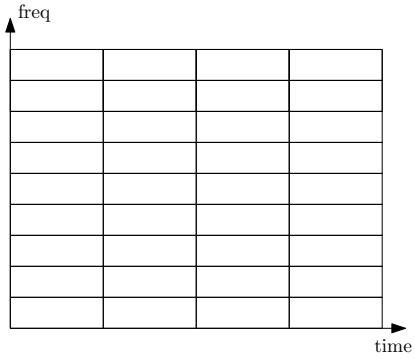

(d) STFT with low time but high frequency resolution.

Figure B.2. Resolution issues in STFT.

C

WAVELET TRANSFORM

The frequency analysis of a signal through the Fourier transform is based on the description of the original signal as sum of specifically defined sinusoids. The amplitude of each sinusoid describes how much that harmonic (positioned at a specific frequency) contributes in the definition of the signal waveform. In other words, the transform is the decomposition of the signal in different "mother" signals (the sinusoids) opportunely scaled and translated in frequency. As a general approach, one can perform a similar transformation using any mother signal.

Nonetheless, using the Fourier transform approach the time information is lost. In the CWT, the signal is decomposed according to a sum of simple mother signals (wavelets), but in this case the time information is preserved.

Let's define a general mother wavelet $\psi(t)$. In order to be eligible for the CWT it has to guarantee some properties [70]:

- Defining as $L^2(\mathbb{R})$ the set of square derivable functions, $\psi(t) \in L^2(\mathbb{R})$
- $\int_0^\infty \frac{|\Psi(\omega)|^2}{|\omega|} d\omega < \infty$, in which as $\Psi(\omega)$ is indicated the Fourier Transform of the mother wavelet $\psi(t)$

A "dilated-translated" version of the original wavelet can be defined as main decomposition tool of the original time-series.

$$\psi_{a,b}(t) = \frac{1}{\sqrt{a}} \psi \left(\frac{t-b}{a} \right) \tag{C.1}$$

The dilation coefficient a makes the wavelet larger or tighter, while the translation coefficient b specifies a time offset of the wavelet. Since a low frequency sinusoid has a larger period, large values of a are used for wavelets whose amplitudes describe the low frequency behaviour of the signal. The contrary is valid for high values of a. The time shift parameter b, considered respect to the original signal, is used to localize the wavelet (and so that specific frequency behaviour) along the time axis.

The CWT can be evaluated by the following integral.

$$W_x(a,b) = < x, \psi_{a,b} > = \int_{-\infty}^{\infty} x(t) \overline{\psi}_{a,b}(t) dt = \frac{1}{\sqrt{a}} \int_{-\infty}^{\infty} x(t) \overline{\psi} \left(\frac{t-b}{a} \right) dt \tag{C.2}$$

With symbol $\overline{\psi}$ is indicated the conjugate complex of ψ. The integral result gives a quantitative meaning of how much the specific dilated-translated wavelet contributes in the signal waveform.

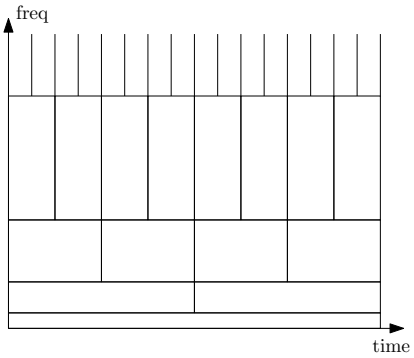

Figure C.1. Phase Plan partition with the CWT.

Generally, instead of the pure CWT $W_x(a, b)$, its energy density is considered:

$$S(a, b) = |W_x(a, b)|^2. \tag{C.3}$$

This quantity is called scalogram and it is typically plotted as function of the frequency-related parameter a and the time b.

For the present analysis, its discrete version is of interest.

$$W_x(a, kT_s) = \frac{T_s}{\sqrt{a}} \sum_n x(nT_s)\overline{\psi}\left(\frac{(n-k)T_s}{a}\right) \tag{C.4}$$

The computational complexity of this tool is $O(n)$ [70] and an example of its scalogram plot can be observed in Figure 5.6. In this case, the uncertainty principle application for the realization of the Heisenberg boxes leads to a dyadic partition of the Phase Plane (Figure C.1). Moving downside along the plane the wavelets at increasing values of a (larger wavelets, low frequency description capabilities of the wavelet) are considered. The abscissa axis describes the time position of the wavelet according to coefficient b. The decomposition level consists on the number of dilations a that are considered in the CWT implementation to span the desired range of frequency. For example, in the case of section 5.2, 36 values of a were chosen to describe the frequency behaviour in the range 5 to 60 Hz.

A CWT typical effect is called edge effect and it is caused by the finite length of the sampled pattern on which the CWT is performed. In order to obtain the CWT each dilated-translated wavelet must be applied along the entire signal. To do this, the centre of the wavelet is iteratively shifted and applied in correspondence of each original sample. At the beginning and at the end of the signal a particular condition, graphically described in top plot of Figure C.2 occurs. There is a part of the mother wavelet that is applied on a region in which the signal $x(t)$ is undefined. In order to perform the transform (C.4) it is assumed that the signal is zero outside its domain, thus causing a distortion of the original signal and relative CWT at initial and final instants. The time length of this distortion grows as the wavelet becomes wider, that is, at growing values of a. In the frequency-time plane this distortion is localized into a limited area shown in Figure C.2.

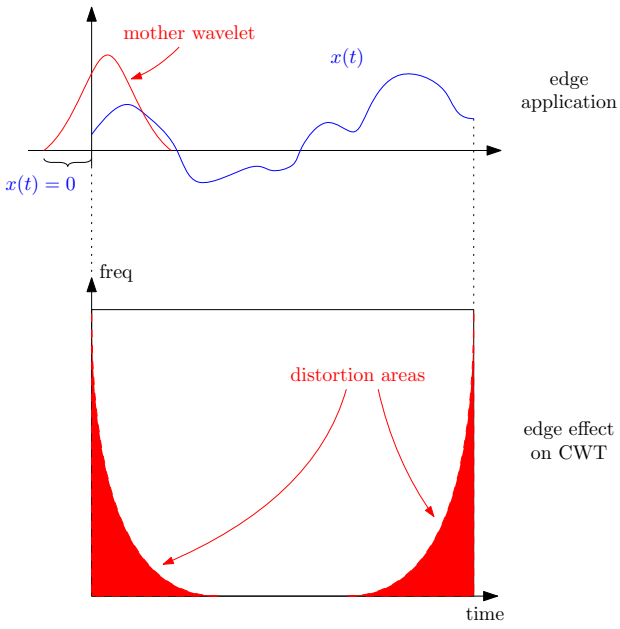

Figure C.2. Edge effect on the frequency-time plane CWT.

D

DERIVATION OF JACOBIANS USING THE RBF-ANN MODEL

The analytical Jacobian $\mathbf{F}$ is here derived. The dependence on sampling time k is omitted for simplicity. Equation (6.6) is considered and it is here recalled to make reading more comfortable.

$$\mathbf{f} = \begin{cases} i_{\alpha,k+1} = i_{\alpha,k} + T_s\gamma_{11,k}[u_{\alpha,k} - Ri_{\alpha,k} - \omega_{me,k}(b_{11,k}i_{\alpha,k} + b_{12,k}i_{\beta,k} + c_{\alpha,k})] + \\ \qquad + T_s\gamma_{12,k}[u_{\beta,k} - Ri_{\beta,k} - \omega_{me,k}(b_{21,k}i_{\alpha,k} + b_{22,k}i_{\beta,k} + c_{\beta,k})] \\ i_{\beta,k+1} = i_{\beta,k} + T_s\gamma_{21,k}[u_{\alpha,k} - Ri_{\alpha,k} - \omega_{me,k}(b_{11,k}i_{\alpha,k} + b_{12,k}i_{\beta,k} + c_{\alpha,k})] + \\ \qquad + T_s\gamma_{22,k}[u_{\beta,k} - Ri_{\beta,k} - \omega_{me,k}(b_{21,k}i_{\alpha,k} + b_{22,k}i_{\beta,k} + c_{\beta,k})] \\ \omega_{me,k+1} = \omega_{me,k} \\ \vartheta_{me,k+1} = \vartheta_{me,k} + T_s\omega_{me,k} \end{cases}$$

To easy the next mathematical passages, the following variables are defined:

$$\mathbf{f} = \begin{cases} f_{i_\alpha} \\ f_{i_\beta} \\ f_{\omega_{me}} \\ f_{\vartheta_{me}} \end{cases} \tag{D.1}$$

The Jacobian matrix is defined as

$$\mathbf{F} = \frac{\partial \mathbf{f}}{\partial \mathbf{x}} = \begin{bmatrix} \frac{\partial f_{i_\alpha}}{\partial i_\alpha} & \frac{\partial f_{i_\alpha}}{\partial i_\beta} & \frac{\partial f_{i_\alpha}}{\partial \omega_{me}} & \frac{\partial f_{i_\alpha}}{\partial \vartheta_{me}} \\ \frac{\partial f_{i_\beta}}{\partial i_\alpha} & \frac{\partial f_{i_\beta}}{\partial i_\beta} & \frac{\partial f_{i_\beta}}{\partial \omega_{me}} & \frac{\partial f_{i_\beta}}{\partial \vartheta_{me}} \\ \frac{\partial f_{\omega_{me}}}{\partial i_\alpha} & \frac{\partial f_{\omega_{me}}}{\partial i_\beta} & \frac{\partial f_{\omega_{me}}}{\partial \omega_{me}} & \frac{\partial f_{\omega_{me}}}{\partial \vartheta_{me}} \\ \frac{\partial f_{\vartheta_{me}}}{\partial i_\alpha} & \frac{\partial f_{\vartheta_{me}}}{\partial i_\beta} & \frac{\partial f_{\vartheta_{me}}}{\partial \omega_{me}} & \frac{\partial f_{\vartheta_{me}}}{\partial \vartheta_{me}} \end{bmatrix}$$

Exploiting coefficients γ_{11}, γ_{12}, γ_{21} and γ_{22} as denoted in (2.16) the component in (D.2) are evaluated with the following equations.

$$\frac{\partial f_{i_\alpha}}{\partial i_\alpha} = 1 + T_s \frac{\partial \gamma_{11}}{\partial i_\alpha}[u_\alpha - Ri_\alpha - \omega_{me}(b_{11} i_\alpha + b_{12} i\beta + c_1)] + \\ + T_s \frac{\partial \gamma_{12}}{\partial i_\alpha}[u_\beta - Ri_\beta - \omega_{me}(b_{21} i_\alpha + b_{22} i\beta + c_2)] + \\ + T_s \gamma_{11} \left[-R - \omega_{me} \left(\frac{\partial b_{11}}{\partial i_\alpha} i_\alpha + b_{11} + \frac{\partial b_{12}}{\partial i_\alpha} i_\beta + \frac{\partial c_1}{\partial i_\alpha} \right) \right] + \\ + T_s \gamma_{12} \left[-\omega_{me} \left(\frac{\partial b_{21}}{\partial i_\alpha} i_\alpha + b_{21} + \frac{\partial b_{22}}{\partial i_\alpha} i_\beta + \frac{\partial c_2}{\partial i_\alpha} \right) \right] \tag{D.2}$$

$$\frac{\partial f_{i_\alpha}}{\partial i_\beta} = T_s \frac{\partial \gamma_{11}}{\partial i_\beta}[u_\alpha - Ri_\alpha - \omega_{me}(b_{11} i_\alpha + b_{12} i\beta + c_1)] + \\ + T_s \frac{\partial \gamma_{12}}{\partial i_\beta}[u_\beta - Ri_\beta - \omega_{me}(b_{21} i_\alpha + b_{22} i\beta + c_2)] + \\ + T_s \gamma_{11} \left[-\omega_{me} \left(\frac{\partial b_{11}}{\partial i_\beta} i_\alpha + \frac{\partial b_{12}}{\partial i_\beta} i_\beta + b_{12} + \frac{\partial c_1}{\partial i_\beta} \right) \right] + \\ + T_s \gamma_{12} \left[-R - \omega_{me} \left(\frac{\partial b_{21}}{\partial i_\beta} i_\alpha + \frac{\partial b_{22}}{\partial i_\beta} i_\beta + b_{22} + \frac{\partial c_2}{\partial i_\beta} \right) \right] \tag{D.3}$$

$$\frac{\partial f_{i_\alpha}}{\partial \omega_{me}} = T_s \gamma_{11}[-(b_{11} i_\alpha + c_1 + b_{12} i_\beta)] + \\ T_s \gamma_{12}[-(b_{21} i_\alpha + c_2 + b_{22} i_\beta)] \tag{D.4}$$

$$\frac{\partial f_{i_\alpha}}{\partial \vartheta_{me}} = T_s \frac{\partial \gamma_{11}}{\partial \vartheta_{me}}[u_\alpha - Ri_\alpha - \omega_{me}(b_{11} i_\alpha + b_{12} i\beta + c_1)] + \\ + T_s \frac{\partial \gamma_{12}}{\partial \vartheta_{me}}[u_\beta - Ri_\beta - \omega_{me}(b_{21} i_\alpha + b_{22} i\beta + c_2)] + \\ + T_s \gamma_{11} \left[-\omega_{me} \left(\frac{\partial b_{11}}{\partial \vartheta_{me}} i_\alpha + \frac{\partial b_{12}}{\partial \vartheta_{me}} i_\beta + \frac{\partial c_1}{\partial \vartheta_{me}} \right) \right] + \\ + T_s \gamma_{12} \left[-\omega_{me} \left(\frac{\partial b_{21}}{\partial \vartheta_{me}} i_\alpha + \frac{\partial b_{22}}{\partial \vartheta_{me}} i_\beta + \frac{\partial c_2}{\partial \vartheta_{me}} \right) \right] \tag{D.5}$$

$$\frac{\partial f_{i_\beta}}{\partial i_\alpha} = T_s \frac{\partial \gamma_{21}}{\partial i_\alpha}[u_\alpha - Ri_\alpha - \omega_{me}(b_{11} i_\alpha + b_{12} i\beta + c_1)] + \\ + T_s \frac{\partial \gamma_{22}}{\partial i_\alpha}[u_\beta - Ri_\beta - \omega_{me}(b_{21} i_\alpha + b_{22} i\beta + c_2)] + \\ + T_s \gamma_{21} \left[-R - \omega_{me} \left(\frac{\partial b_{11}}{\partial i_\alpha} i_\alpha + b_{11} + \frac{\partial b_{12}}{\partial i_\alpha} i_\beta + \frac{\partial c_1}{\partial i_\alpha} \right) \right] + \\ + T_s \gamma_{22} \left[-\omega_{me} \left(\frac{\partial b_{21}}{\partial i_\alpha} i_\alpha + b_{21} + \frac{\partial b_{22}}{\partial i_\alpha} i_\beta + \frac{\partial c_2}{\partial i_\alpha} \right) \right] \tag{D.6}$$

$$\begin{aligned}\frac{\partial f_{i_\beta}}{\partial i_\beta} &= 1 + T_s\frac{\partial \gamma_{21}}{\partial i_\beta}[u_\alpha - Ri_\alpha - \omega_{me}(b_{11}i_\alpha + b_{12}i\beta + c_1)]+\\ &+ T_s\frac{\partial \gamma_{22}}{\partial i_\beta}[u_\beta - Ri_\beta - \omega_{me}(b_{21}i_\alpha + b_{22}i\beta + c_2)]+\\ &+ T_s\gamma_{21}\left[-\omega_{me}\left(\frac{\partial b_{11}}{\partial i_\beta}i_\alpha + \frac{\partial b_{12}}{\partial i_\beta}i_\beta + b_{12} + \frac{\partial c_1}{\partial i_\beta}\right)\right] +\\ &+ T_s\gamma_{22}\left[-R - \omega_{me}\left(\frac{\partial b_{21}}{\partial i_\beta}i_\alpha + \frac{\partial b_{22}}{\partial i_\beta}i_\beta + b_{22} + \frac{\partial c_2}{\partial i_\beta}\right)\right]\end{aligned} \tag{D.7}$$

$$\begin{aligned}\frac{\partial f_{i_\beta}}{\partial \omega_{me}} &= T_s\gamma_{21}[-(b_{11}i_\alpha + c_1 + b_{12}i_\beta)]+\\ &T_s\gamma_{22}[-(b_{21}i_\alpha + c_2 + b_{22}i_\beta)]\end{aligned} \tag{D.8}$$

$$\begin{aligned}\frac{\partial f_{i_\beta}}{\partial \vartheta_{me}} &= T_s\frac{\partial \gamma_{21}}{\partial \vartheta_{me}}[u_\alpha - Ri_\alpha - \omega_{me}(b_{11}i_\alpha + b_{12}i\beta + c_1)]+\\ &+ T_s\frac{\partial \gamma_{22}}{\partial \vartheta_{me}}[u_\beta - Ri_\beta - \omega_{me}(b_{21}i_\alpha + b_{22}i\beta + c_2)]+\\ &+ T_s\gamma_{21}\left[-\omega_{me}\left(\frac{\partial b_{11}}{\partial \vartheta_{me}}i_\alpha + \frac{\partial b_{12}}{\partial \vartheta_{me}}i_\beta + \frac{\partial c_1}{\partial \vartheta_{me}}\right)\right] +\\ &+ T_s\gamma_{22}\left[-\omega_{me}\left(\frac{\partial b_{21}}{\partial \vartheta_{me}}i_\alpha + \frac{\partial b_{22}}{\partial \vartheta_{me}}i_\beta + \frac{\partial c_2}{\partial \vartheta_{me}}\right)\right]\end{aligned} \tag{D.9}$$

$$\begin{aligned}&\frac{\partial f_{\omega_{me}}}{\partial i_\alpha} = 0, \quad \frac{\partial f_{\omega_{me}}}{\partial i_\beta} = 0, \quad \frac{\partial f_{\omega_{me}}}{\partial i_{\omega_{me}}} = 1, \quad \frac{\partial f_{\omega_{me}}}{\partial i_{\vartheta_{me}}} = 0\\ &\frac{\partial f_{\vartheta_{me}}}{\partial i_\alpha} = 0, \quad \frac{\partial f_{\vartheta_{me}}}{\partial i_\beta} = 0, \quad \frac{\partial f_{\vartheta_{me}}}{\partial i_{\omega_{me}}} = T_s, \quad \frac{\partial f_{\vartheta_{me}}}{\partial i_{\vartheta_{me}}} = 1\end{aligned} \tag{D.10}$$

Of these Jacobians the following components have to make explicit.

$$\frac{\partial \gamma_{11}}{\partial i_\alpha} = \frac{\partial(1/\det\mathbf{A})}{\partial i_\alpha}\gamma_{11} + \frac{1}{\det\mathbf{A}}\left(\frac{\partial L_\Sigma}{\partial i_\alpha} - \frac{L_\Delta}{\partial i_\alpha}\cos(2\vartheta_{me}) + \frac{\partial L_{dq}}{\partial i_\alpha}\sin(2\vartheta_{me})\right) \tag{D.11}$$

$$\frac{\partial \gamma_{12}}{\partial i_\alpha} = \frac{\partial \gamma_{21}}{\partial i_\alpha} = \frac{\partial(1/\det\mathbf{A})}{\partial i_\alpha}\gamma_{12} + \frac{1}{\det\mathbf{A}}\left(-\frac{L_\Delta}{\partial i_\alpha}\sin(2\vartheta_{me}) - \frac{\partial L_{dq}}{\partial i_\alpha}\cos(2\vartheta_{me})\right) \tag{D.12}$$

$$\frac{\partial \gamma_{22}}{\partial i_\alpha} = \frac{\partial(1/\det\mathbf{A})}{\partial i_\alpha}\gamma_{22} + \frac{1}{\det\mathbf{A}}\left(\frac{\partial L_\Sigma}{\partial i_\alpha} + \frac{L_\Delta}{\partial i_\alpha}\cos(2\vartheta_{me}) - \frac{\partial L_{dq}}{\partial i_\alpha}\sin(2\vartheta_{me})\right) \tag{D.13}$$

$$\frac{\partial \gamma_{11}}{\partial i_\beta} = \frac{\partial(1/\det\mathbf{A})}{\partial i_\beta}\gamma_{11} + \frac{1}{\det\mathbf{A}}\left(\frac{\partial L_\Sigma}{\partial i_\beta} - \frac{L_\Delta}{\partial i_\beta}\cos(2\vartheta_{me}) + \frac{\partial L_{dq}}{\partial i_\beta}\sin(2\vartheta_{me})\right) \tag{D.14}$$

$$\frac{\partial \gamma_{12}}{\partial i_\beta} = \frac{\partial \gamma_{21}}{\partial i_\beta} = \frac{\partial(1/\det\mathbf{A})}{\partial i_\beta}\gamma_{12} + \frac{1}{\det\mathbf{A}}\left(-\frac{L_\Delta}{\partial i_\beta}\sin(2\vartheta_{me}) - \frac{\partial L_{dq}}{\partial i_\beta}\cos(2\vartheta_{me})\right) \tag{D.15}$$

$$\frac{\partial \gamma_{22}}{\partial i_\beta} = \frac{\partial(1/\det\mathbf{A})}{\partial i_b}\gamma_{22} + \frac{1}{\det\mathbf{A}}\left(\frac{\partial L_\Sigma}{\partial i_\beta} + \frac{L_\Delta}{\partial i_\beta}\cos(2\vartheta_{me}) - \frac{\partial L_{dq}}{\partial i_\beta}\sin(2\vartheta_{me})\right) \tag{D.16}$$

$$\begin{aligned}\frac{\partial \gamma_{11}}{\partial \vartheta_{me}} = \frac{\partial(1/\det\mathbf{A})}{\partial \vartheta_{me}}\gamma_{11} + \frac{1}{\det\mathbf{A}}\Bigg(&\frac{\partial L_\Sigma}{\partial \vartheta_{me}} - \frac{L_\Delta}{\partial \vartheta_{me}}\cos(2\vartheta_{me}) + \frac{\partial L_{dq}}{\partial \vartheta_{me}}\sin(2\vartheta_{me}) - \\ &- L_\Delta\sin(2\vartheta_{me}) + L_{dq}\cos(2\vartheta_{me})\Bigg)\end{aligned} \tag{D.17}$$

$$\begin{aligned}\frac{\partial \gamma_{12}}{\partial \vartheta_{me}} = \frac{\partial \gamma_{21}}{\partial \vartheta_{me}} = \frac{\partial(1/\det\mathbf{A})}{\partial \vartheta_{me}}\gamma_{12} + \frac{1}{\det\mathbf{A}}\Bigg(&- \frac{L_\Delta}{\partial \vartheta_{me}}\sin(2\vartheta_{me}) - \frac{\partial L_{dq}}{\partial \vartheta_{me}}\cos(2\vartheta_{me}) - \\ &- L_\Delta\cos(2\vartheta_{me}) + L_{dq}\sin(2\vartheta_{me})\Bigg)\end{aligned} \tag{D.18}$$

$$\begin{aligned}\frac{\partial \gamma_{22}}{\partial \vartheta_{me}} = \frac{\partial(1/\det\mathbf{A})}{\partial \vartheta_{me}}\gamma_{22} + \frac{1}{\det\mathbf{A}}\Bigg(&\frac{\partial L_\Sigma}{\partial \vartheta_{me}} + \frac{L_\Delta}{\partial \vartheta_{me}}\cos(2\vartheta_{me}) - \frac{\partial L_{dq}}{\partial \vartheta_{me}}\sin(2\vartheta_{me}) + \\ &+ L_\Sigma - L_\Delta\sin(2\vartheta_{me}) - L_{dq}\cos(2\vartheta_{me})\Bigg)\end{aligned} \tag{D.19}$$

in which:

$$\frac{\partial(1/\det\mathbf{A})}{\partial i_\alpha} = -\frac{\dfrac{\partial L_d}{\partial i_\alpha}L_q + \dfrac{\partial L_q}{\partial i_\alpha}L_d + 2L_{dq}\dfrac{\partial L_{dq}}{\partial i_\alpha}}{(L_dL_q - L_{dq}^2)^2} \tag{D.20}$$

$$\frac{\partial(1/\det\mathbf{A})}{\partial i_\beta} = -\frac{\dfrac{\partial L_d}{\partial i_\beta}L_q + \dfrac{\partial L_q}{\partial i_\beta}L_d + 2L_{dq}\dfrac{\partial L_{dq}}{\partial i_\beta}}{(L_dL_q - L_{dq}^2)^2} \tag{D.21}$$

$$\frac{\partial(1/\det\mathbf{A})}{\partial \vartheta_{me}} = -\frac{\dfrac{\partial L_d}{\partial \vartheta_{me}}L_q + \dfrac{\partial L_q}{\partial \vartheta_{me}}L_d + 2L_{dq}\dfrac{\partial L_{dq}}{\partial \vartheta_{me}}}{(L_dL_q - L_{dq}^2)^2} \tag{D.22}$$

and finally:

$$\frac{\partial b_{11}}{\partial i_\alpha} = -\frac{\partial L_\Delta}{\partial i_\alpha}\sin(2\vartheta_{me}) - \frac{\partial L_{dq}}{\partial i_\alpha}\cos(2\vartheta_{me}) \tag{D.23}$$

$$\frac{\partial b_{12}}{\partial i_\alpha} = \frac{\partial L_\Sigma}{\partial i_\alpha} + \frac{\partial L_\Delta}{\partial i_\alpha}\cos(2\vartheta_{me}) - \frac{\partial L_{dq}}{\partial i_\alpha}\sin(2\vartheta_{me}) \tag{D.24}$$

$$\frac{\partial b_{21}}{\partial i_\alpha} = -\frac{\partial L_\Sigma}{\partial i_\alpha} + \frac{\partial L_\Delta}{\partial i_\alpha}\cos(2\vartheta_{me}) - \frac{\partial L_{dq}}{\partial i_\alpha}\sin(2\vartheta_{me}) \tag{D.25}$$

$$\frac{\partial b_{22}}{\partial i_\alpha} = \frac{\partial L_\Delta}{\partial i_\alpha}\sin(2\vartheta_{me}) + \frac{\partial L_{dq}}{\partial i_\alpha}\cos(2\vartheta_{me}) \tag{D.26}$$

$$\frac{\partial b_{11}}{\partial i_\beta} = -\frac{\partial L_\Delta}{\partial i_\beta}\sin(2\vartheta_{me}) - \frac{\partial L_{dq}}{\partial i_\beta}\cos(2\vartheta_{me}) \tag{D.27}$$

$$\frac{\partial b_{12}}{\partial i_\beta} = \frac{\partial L_\Sigma}{\partial i_\beta} + \frac{\partial L_\Delta}{\partial i_\beta}\cos(2\vartheta_{me}) - \frac{\partial L_{dq}}{\partial i_\beta}\sin(2\vartheta_{me}) \tag{D.28}$$

$$\frac{\partial b_{21}}{\partial i_\beta} = -\frac{\partial L_\Sigma}{\partial i_\beta} + \frac{\partial L_\Delta}{\partial i_\beta}\cos(2\vartheta_{me}) - \frac{\partial L_{dq}}{\partial i_\beta}\sin(2\vartheta_{me}) \tag{D.29}$$

$$\frac{\partial b_{22}}{\partial i_\beta} = \frac{\partial L_\Delta}{\partial i_\beta}\sin(2\vartheta_{me}) + \frac{\partial L_{dq}}{\partial i_\beta}\cos(2\vartheta_{me}) \tag{D.30}$$

$$\begin{aligned}\frac{\partial b_{11}}{\partial \vartheta_{me}} = &-\frac{\partial L_\Delta}{\partial \vartheta_{me}}\sin(2\vartheta_{me}) - \frac{\partial L_{dq}}{\partial \vartheta_{me}}\cos(2\vartheta_{me}) - \\ &- 2L_\Delta\cos(2\vartheta_{me}) + 2L_{dq}\sin(2\vartheta_{me})\end{aligned} \tag{D.31}$$

$$\begin{aligned}\frac{\partial b_{12}}{\partial \vartheta_{me}} = &\frac{\partial L_\Sigma}{\partial \vartheta_{me}} + \frac{\partial L_\Delta}{\partial \vartheta_{me}}\cos(2\vartheta_{me}) - \frac{\partial L_{dq}}{\partial \vartheta_{me}}\sin(2\vartheta_{me}) - \\ &- 2L_\Delta\sin(2\vartheta_{me}) + 2L_{dq}\cos(2\vartheta_{me})\end{aligned} \tag{D.32}$$

$$\begin{aligned}\frac{\partial b_{21}}{\partial \vartheta_{me}} = &-\frac{\partial L_\Sigma}{\partial \vartheta_{me}} + \frac{\partial L_\Delta}{\partial \vartheta_{me}}\cos(2\vartheta_{me}) - \frac{\partial L_{dq}}{\partial \vartheta_{me}}\sin(2\vartheta_{me}) - \\ &- 2L_\Delta\sin(2\vartheta_{me}) - 2L_{dq}\cos(2\vartheta_{me})\end{aligned} \tag{D.33}$$

$$\frac{\partial b_{22}}{\partial \vartheta_{me}} = -\frac{\partial L_\Delta}{\partial \vartheta_{me}} \sin(2\vartheta_{me}) - \frac{\partial L_{dq}}{\partial \vartheta_{me}} \cos(2\vartheta_{me}) + \\ + 2L_\Delta \cos(2\vartheta_{me}) - 2L_{dq} \sin(2\vartheta_{me}) \tag{D.34}$$

$$\frac{\partial c_1}{\partial i_\alpha} = -\frac{\partial \lambda_d}{\partial i_\alpha} \sin(2\vartheta_{me}) - \frac{\partial \lambda_q}{\partial i_\alpha} \cos(2\vartheta_{me}) \tag{D.35}$$

$$\frac{\partial c_1}{\partial i_\beta} = -\frac{\partial \lambda_d}{\partial i_\beta} \sin(2\vartheta_{me}) - \frac{\partial \lambda_q}{\partial i_\beta} \cos(2\vartheta_{me}) \tag{D.36}$$

$$\frac{\partial c_1}{\partial \vartheta_{me}} = -\frac{\partial \lambda_d}{\partial \vartheta_{me}} \sin(\vartheta_{me}) - \frac{\partial \lambda_q}{\partial \vartheta_{me}} \cos(\vartheta_{me}) - \lambda_d \cos(\vartheta_{me}) + \lambda_q \sin(\vartheta_{me}) \tag{D.37}$$

$$\frac{\partial c_2}{\partial i_\alpha} = \frac{\partial \lambda_d}{\partial i_\alpha} \sin(2\vartheta_{me}) - \frac{\partial \lambda_q}{\partial i_\alpha} \cos(2\vartheta_{me}) \tag{D.38}$$

$$\frac{\partial c_2}{\partial i_\beta} = \frac{\partial \lambda_d}{\partial i_\beta} \sin(2\vartheta_{me}) - \frac{\partial \lambda_q}{\partial i_\beta} \cos(2\vartheta_{me}) \tag{D.39}$$

$$\frac{\partial c_2}{\partial \vartheta_{me}} = \frac{\partial \lambda_d}{\partial \vartheta_{me}} \cos(\vartheta_{me}) - \frac{\partial \lambda_q}{\partial \vartheta_{me}} \sin(\vartheta_{me}) - \lambda_d \sin(\vartheta_{me}) - \lambda_q \cos(\vartheta_{me}) \tag{D.40}$$

The equations above are necessary for the implementation of the EKF in the $\alpha\beta$ reference frame taking into account of SynRM model non linearities. They are valid whatever function is used to interpolate the fluxes and differential inductances at varying of i_α, i_β and ϑ_{me}. Tailoring the analysis to the usage of an ANN model as that described in equations (6.10) and (6.11) in chapter 6 the following mathematical steps can be performed.

$$\begin{aligned} \frac{\partial \lambda_d}{\partial i_\alpha} &= \sum_{k=0}^{K} w_k^d \frac{\partial a_k}{\partial i_\alpha}, & \frac{\partial \lambda_q}{\partial i_\alpha} &= \sum_{k=0}^{K} w_k^q \frac{\partial a_k}{\partial i_\alpha} \\ \frac{\partial \lambda_d}{\partial i_\beta} &= \sum_{k=0}^{K} w_k^d \frac{\partial a_k}{\partial i_\beta}, & \frac{\partial \lambda_q}{\partial i_\beta} &= \sum_{k=0}^{K} w_k^q \frac{\partial a_k}{\partial i_\beta} \\ \frac{\partial \lambda_d}{\partial \vartheta_{me}} &= \sum_{k=0}^{K} w_k^d \frac{\partial a_k}{\partial \vartheta_{me}}, & \frac{\partial \lambda_q}{\partial \vartheta_{me}} &= \sum_{k=0}^{K} w_k^q \frac{\partial a_k}{\partial \vartheta_{me}} \end{aligned} \tag{D.41}$$

and

$$\frac{\partial L_d}{\partial i_\alpha} = \sum_{k=0}^{K} -2w_k^d b_k^2 [a_k \cos(\vartheta_{me}) + (i_\alpha \cos(\vartheta_{me}) + i_\beta \sin(\vartheta_{me}) - x_k^d)\frac{\partial a_k}{\partial i_\alpha}] \tag{D.42}$$

$$\frac{\partial L_d}{\partial i_\beta} = \sum_{k=0}^{K} -2w_k^d b_k^2 [a_k \sin(\vartheta_{me}) + (i_\alpha \cos(\vartheta_{me}) + i_\beta \sin(\vartheta_{me}) - x_k^d)\frac{\partial a_k}{\partial i_\beta}] \tag{D.43}$$

$$\frac{\partial L_d}{\partial \vartheta_{me}} = \sum_{k=0}^{K} -2w_k^d b_k^2 [a_k(-i_\alpha \sin(\vartheta_{me}) + i_\beta \cos(\vartheta_{me}))+ \tag{D.44}$$

$$+ (i_\alpha \cos(\vartheta_{me}) + i_\beta \sin(\vartheta_{me}) - x_k^d)\frac{\partial a_k}{\partial \vartheta_{me}}] \tag{D.45}$$

$$\frac{\partial L_q}{\partial i_\alpha} = \sum_{k=0}^{K} -2w_k^q b_k^2 [-a_k \sin(\vartheta_{me}) + (-i_\alpha \sin(\vartheta_{me}) + i_\beta \cos(\vartheta_{me}) - x_k^q)\frac{\partial a_k}{\partial i_\alpha}] \tag{D.46}$$

$$\frac{\partial L_q}{\partial i_\beta} = \sum_{k=0}^{K} -2w_k^q b_k^2 [a_k \cos(\vartheta_{me}) + (-i_\alpha \sin(\vartheta_{me}) + i_\beta \cos(\vartheta_{me}) - x_k^q)\frac{\partial a_k}{\partial i_\beta}] \tag{D.47}$$

$$\frac{\partial L_q}{\partial \vartheta_{me}} = \sum_{k=0}^{K} -2w_k^q b_k^2 [a_k(-i_\alpha \cos(\vartheta_{me}) - i_\beta \sin(\vartheta_{me}))+ \tag{D.48}$$

$$+ (-i_\alpha \sin(\vartheta_{me}) + i_\beta \cos(\vartheta_{me}) - x_k^q)\frac{\partial a_k}{\partial \vartheta_{me}}] \tag{D.49}$$

$$\frac{\partial L_{dq}}{\partial i_\alpha} = \sum_{k=0}^{K} -2w_k^d b_k^2 [-a_k \sin(\vartheta_{me}) + (-i_\alpha \sin(\vartheta_{me}) + i_\beta \cos(\vartheta_{me}) - x_k^q)\frac{\partial a_k}{\partial i_\alpha}] \tag{D.50}$$

$$\frac{\partial L_{dq}}{\partial i_\beta} = \sum_{k=0}^{K} -2w_k^d b_k^2 [a_k \cos(\vartheta_{me}) + (-i_\alpha \sin(\vartheta_{me}) + i_\beta \cos(\vartheta_{me}) - x_k^q)\frac{\partial a_k}{\partial i_\beta}] \tag{D.51}$$

$$\frac{\partial L_{dq}}{\partial \vartheta_{me}} = \sum_{k=0}^{K} -2w_k^d b_k^2 [a_k(-i_\alpha \cos(\vartheta_{me}) - i_\beta \sin(\vartheta_{me}))+ \tag{D.52}$$

$$+ (-i_\alpha \sin(\vartheta_{me}) + i_\beta \cos(\vartheta_{me}) - x_k^q)\frac{\partial a_k}{\partial \vartheta_{me}}] \tag{D.53}$$

in which

$$\frac{\partial a_k}{\partial i_\alpha} = -2b_k^2 a_k[i_\alpha \cos(\vartheta_{me}) + i_\beta \sin(\vartheta_{me}) - x_k^d - \\ - i_\alpha \sin(\vartheta_{me}) + i_\beta \cos(\vartheta_{me}) - x_k^q)][\cos(\vartheta_{me}) - \sin(\vartheta_{me})] \tag{D.54}$$

$$\frac{\partial a_k}{\partial i_\beta} = -2b_k^2 a_k[i_\alpha \cos(\vartheta_{me}) + i_\beta \sin(\vartheta_{me}) - x_k^d - \\ - i_\alpha \sin(\vartheta_{me}) + i_\beta \cos(\vartheta_{me}) - x_k^q)][\sin(\vartheta_{me}) + \cos(\vartheta_{me})] \tag{D.55}$$

$$\frac{\partial a_k}{\partial \vartheta_{me}} = -2b_k^2 a_k[i_\alpha \cos(\vartheta_{me}) + i_\beta \sin(\vartheta_{me}) - x_k^d - \\ - i_\alpha \sin(\vartheta_{me}) + i_\beta \cos(\vartheta_{me}) - x_k^q)][-i_\alpha \sin(\vartheta_{me}) + i_\beta \cos(\vartheta_{me}) - \\ - i_\alpha \cos(\vartheta_{me}) + i_\beta \sin(\vartheta_{me})] \tag{D.56}$$

BIBLIOGRAPHY

[1] Sorin-Cristian Agarliţă, M. Fătu, L. N. Tutelea, F. Blaabjerg, and I. Boldea. "I-f starting and active flux based sensorless vector control of reluctance synchronous motors, with experiments". In: *2010 12th International Conference on Optimization of Electrical and Electronic Equipment*. May 2010, pp. 337–342. DOI: 10.1109/OPTIM.2010.5510564.

[2] International Energy Agency. *World Energy Outlook 2016*. https://www.iea.org/reports/world-energy-outlook-2016. Nov. 2016.

[3] S. Albawi, T. A. Mohammed, and S. Al-Zawi. "Understanding of a convolutional neural network". In: *2017 International Conference on Engineering and Technology (ICET)*. IEEE, 2017, pp. 1–6.

[4] L. Alberti, N. Bianchi, and S. Bolognani. "Variable-Speed Induction Machine Performance Computed Using Finite-Element". In: *IEEE Transactions on Industry Applications* 47.2 (2011), pp. 789–797.

[5] Strategy Analytics. *The Second Dawn of Electrification: An Electrified Future for Personal Transportation*. https://armkeil.blob.core.windows.net/developer/Files/pdf/report/the-second-dawn-of-electrification.pdf. 2020.

[6] R. Antonello, L. Peretti F. Tinazzi, and M. Zigliotto. "Self-commissioning calculation of dynamic models for synchronous machines with magnetic saturation using flux as state variable". In: *9th IET International Conference on Power Electronics, Machines and Drives (PEMD 2018)*. 2018, pp. 3609–3613.

[7] Riccardo Antonello, Ludovico Ortombina, Fabio Tinazzi, and Mauro Zigliotto. "Advanced current control of synchronous reluctance motors". In: *2017 IEEE 12th International Conference on Power Electronics and Drive Systems (PEDS)*. 2017, pp. 1, 037–1, 042. DOI: 10.1109/PEDS.2017.8289150.

[8] J. Antonino-Daviu, H. Razik, A. Quijano-Lopez, and V. Climente-Alarcon. "Detection of rotor faults via transient analysis of the external magnetic field". In: *IECON 2017 - 43rd Annual Conference of the IEEE Industrial Electronics Society*. 2017, pp. 3815–3821. DOI: 10.1109/IECON.2017.8216651.

[9] Jochen Antons and Tobias Rösmann. "Self-sensing control of a synchronous reluctance machine using an extended Kalman filter". In: *2015 IEEE International Conference on Industrial Technology (ICIT)*. 2015, pp. 831–839. DOI: 10.1109/ICIT.2015.7125201.

[10] Akm Arafat, Seungdeog Choi, and Jeihoon Baek. "Open-Phase Fault Detection of a Five-Phase Permanent Magnet Assisted Synchronous Reluctance Motor Based on Symmetrical Components Theory". In: *IEEE Transactions on Industrial Electronics* 64.8 (2017), pp. 6465–6474. DOI: 10.1109/TIE.2017.2682016.

[11] Eric Armando, Radu Iustin Bojoi, Paolo Guglielmi, Gianmario Pellegrino, and Michele Pastorelli. "Experimental Identification of the Magnetic Model of Synchronous Machines". In: *IEEE Transactions on Industry Applications* 49.5 (2013), pp. 2116–2125. DOI: 10.1109/TIA.2013.2258876.

[12] UNFCCC Authors. *United Nations Climate Change Annual Report 2019*. https://unfccc.int/sites/default/files/resource/unfccc_annual_report_2019.pdf. Aug. 2020.

[13] M. H. Beale and H. B. Demuth M. T. Hagan. *Deep Learning Toolbox;[user's Guide]*. MathWorks, 2021.

[14] A. Bellini, C. Concari, G. Franceschini, C. Tassoni, and A. Toscani. "Vibrations, currents and stray flux signals to asses induction motors rotor conditions". In: *IECON 2006 - 32nd Annual Conference on IEEE Industrial Electronics*. 2006, pp. 4963–4968. DOI: 10.1109/IECON.2006.347365.

[15] A. Bellini, F. Filippetti, C. Tassoni, and G. Capolino. "Advances in Diagnostic Techniques for Induction Machines". In: *IEEE Transactions on Industrial Electronics* 55.12 (2008), pp. 4109–4126.

[16] N. Bianchi. *Electrical Machine Analysis Using Finite Elements*. Power Electronics And Applications. CRC, 2005. ISBN: 9780849333996. URL: https://books.google.it/books?id=vvD2CSJGWY0C.

[17] S. Bolognani, L. Tubiana, and M. Zigliotto. "Extended Kalman filter tuning in sensorless PMSM drives". In: *IEEE Transactions on Industry Applications* 39.6 (2003), pp. 1741–1747. DOI: 10.1109/TIA.2003.818991.

[18] S. Bolognani, M. Zigliotto, and M. Zordan. "Extended-range PMSM sensorless speed drive based on stochastic filtering". In: *IEEE Transactions on Power Electronics* 16.1 (Jan. 2001), pp. 110–117. ISSN: 1941-0107. DOI: 10.1109/63.903995.

[19] Martha Bugsch and Bernhard Piepenbreier. "High-Bandwidth Sensorless Control of Synchronous Reluctance Machines in the Low- and Zero-Speed Range". In: *IEEE Transactions on Industry Applications* 56.3 (May 2020), pp. 2663–2672. ISSN: 1939-9367. DOI: 10.1109/TIA.2020.2969123.

[20] Roberto Caro, César A. Silva, Ricardo Pérez, and Juan I. Yuz. "Sensorless control of a SynRM for the whole speed range based on a nonlinear observability analysis". In: *2017 IEEE International Conference on Industrial Technology (ICIT)*. 2017, pp. 336–341. DOI: 10.1109/ICIT.2017.7913253.

[21] E. Carraro, N. Bianchi, S. Zhang, and et.al. "Design and Performance Comparison of Fractional Slot Concentrated Winding Spoke Type Synchronous Motors With Different Slot-Pole Combinations". In: *IEEE Transactions on Industrial Applications* 54.3 (2018), pp. 2276–2284.

[22] A. Ceban, R. Pusca, and R. Romary. "Study of Rotor Faults in Induction Motors Using External Magnetic Field Analysis". In: *IEEE Transactions on Industrial Electronics* 59.5 (2012), pp. 2082–2093. DOI: 10.1109/TIE.2011.2163285.

[23] M.-Y. Chow, R.N. Sharpe, and J.C. Hung. "On the application and design of artificial neural networks for motor fault detection - Part I". In: *IEEE Transactions on Industrial Electronics* 40.2 (1993), pp. 181–188.

[24] Intergovernmental Panel on Climate Change. *Global Warming of 1.5 °C*. https://www.ipcc.ch/site/assets/uploads/sites/2/2019/06/SR15_Full_Report_High_Res.pdf. Mar. 2020.

[25] J. Corral-Hernandez and J. Antonino-Daviu. "Startup-based rotor fault detection in soft-started induction motors for different soft-starter topologies". In: *IECON 2016 - 42nd Annual Conference of the IEEE Industrial Electronics Society*. 2016, pp. 6977–6982. DOI: 10.1109/IECON.2016.7793448.

[26] J. A. Corral-Hernandez, J. Antonino-Daviu, V. Climente-Alarcon, J. Pons-Llinares, and V. Frances-Galiana. "Transient-based rotor cage assessment in induction motors operating with soft-starters". In: *2014 International Conference on Optimization of Electrical and Electronic Equipment (OPTIM)*. 2014, pp. 342–346. DOI: 10.1109/OPTIM.2014.6850926.

[27] J. Faiz and E. Mazaheri-Tehrani. "Demagnetization Modeling and Fault Diagnosing Techniques in Permanent Magnet Machines Under Stationary and Nonstationary Conditions: An Overview". In: *IEEE Transactions on Industry Applications* 53.3 (2017), pp. 2772–2785.

[28] J. Faiz and H. Nejadi-Koti. "Demagnetization Fault Indexes in Permanent Magnet Synchronous Motors—An Overview". In: *IEEE Transactions on Magnetics* 52.4 (2016), pp. 1–11.

[29] S. M. J. R. Fatemi, H. Henao, and G. A. Capolino. "Gearbox monitoring by using the stray flux in an induction machine based electromechanical system". In: *MELECON 2008 - The 14th IEEE Mediterranean Electrotechnical Conference*. 2008, pp. 484–489. DOI: 10.1109/MELCON.2008.4618482.

[30] A. Fawzi, H. Samulowitz, D. Turaga, and P. Frossard. "Adaptive data augmentation for image classification". In: *2016 IEEE International Conference on Image Processing (ICIP)*. IEEE, 2016, pp. 3688–3692.

[31] L. Frosini, A. Albini, and F. Beccarisi. "Detection of torque oscillations in induction motor drives by linear discriminant analysis". In: *2017 IEEE 11th International Symposium on Diagnostics for Electrical Machines, Power Electronics and Drives (SDEMPED)*. 2017, pp. 510–516. DOI: 10.1109/DEMPED.2017.8062403.

[32] Z. Gao, C. Cecati, and S.X. Ding. "A Survey of Fault Diagnosis and Fault-Tolerant Techniques—Part I: Fault Diagnosis With Model-Based and Signal-Based Approaches". In: *IEEE Transactions on Industrial Electronics* 62.6 (2015), pp. 3757–3767.

[33] H. Gavin. "The Levenberg-Marquardt method for nonlinear least squares curve-fitting problems c ©". In: 2013.

[34] Ahmad Ghaderi and Tsuyoshi Hanamoto. "Wide-Speed-Range Sensorless Vector Control of Synchronous Reluctance Motors Based on Extended Programmable Cascaded Low-Pass Filters". In: *IEEE Transactions on Industrial Electronics* 58.6 (June 2011), pp. 2322–2333. ISSN: 1557-9948. DOI: 10.1109/TIE.2010.2066537.

[35] I. Gogul and V.S. Kumar. "Flower species recognition system using convolution neural networks and transfer learning". In: *2017 4th International Conference on Signal Processing, Communications and Networking (ICSCN -2017)*. IEEE, Mar. 2017, pp. 1–6.

[36] I. Goodfellow, Y. Bengio, and A. Courville. *Deep Learning*. The MIT Press, 2016.

[37] Karlheinz Gröchenig. *Foundations of time-frequency analysis*. Springer Science & Business Media, 2001.

[38] K. N. Gyftakis et al. "Comparative Experimental Investigation of Broken Bar Fault Detectability in Induction Motors". In: *IEEE Transactions on Industry Applications* 52.2 (2016), pp. 1452–1459.

[39] M.T. Hagan, H.B. Demuth, M.H. Beale, and O. De Jesús. *Neural Network Design*. Martin Hagan, 2014. ISBN: 9780971732117. URL: https://books.google.it/books?id=4EW9oQEACAAJ.

[40] Jun Hang et al. "Detection of Interturn Short-Circuit Fault for PMSM With Simple Fault Indicator". In: *IEEE Transactions on Energy Conversion* 31.4 (2016), pp. 1697–1699. DOI: 10.1109/TEC.2016.2583780.

[41] Simon S. Haykin. *Neural networks and learning machines*. Third. Upper Saddle River, NJ: Pearson Education, 2009.

[42] H. Henao, G. A. Capolino, and C. Martis. "On the stray flux analysis for the detection of the three-phase induction machine faults". In: *38th IAS Annual Meeting on Conference Record of the Industry Applications Conference, 2003.* Vol. 2. 2003, pp. 1368–1373. DOI: 10.1109/IAS.2003.1257729.

[43] Marko Hinkkanen, Seppo E. Saarakkala, Hafiz Asad Ali Awan, Eemeli Mölsä, and Toni Tuovinen. "Observers for Sensorless Synchronous Motor Drives: Framework for Design and Analysis". In: *IEEE Transactions on Industry Applications* 54.6 (2018), pp. 6090–6100. DOI: 10.1109/TIA.2018.2858753.

[44] Matthias Hofer, Mario Nikowitz, and Manfred Schroedl. "Sensorless control of a reluctance synchronous machine in the whole speed range without voltage pulse injections". In: *2017 IEEE 3rd International Future Energy Electronics Conference and ECCE Asia (IFEEC 2017 - ECCE Asia)*. June 2017, pp. 1194–1198. DOI: 10.1109/IFEEC.2017.7992211.

[45] Jiangang Hu, Lixiang Wei, Jeffrey McGuire, and Zhijun Liu. "Ground fault location self-diagnosis in high resistance grounding drive systems". In: *2014 IEEE Energy Conversion Congress and Exposition (ECCE)*. 2014, pp. 3179–3185. DOI: 10.1109/ECCE.2014.6953832.

[46] T. Hu, T. Tang, and M. Chen. "Data Simulation by Resampling—A Practical Data Augmentation Algorithm for Periodical Signal Analysis-Based Fault Diagnosis". In: *IEEE Access* 7 (2019), pp. 125133–125145.

[47] D. H. Hubel and T. N. Wiesel. "Receptive fields and functional architecture of monkey striate cortex". In: *The journal of Physiology* 195.1 (1968), pp. 215–243.

[48] S. Ichikawa, M. Tomita, S. Doki, and S. Okuma. "Sensorless Control of Synchronous Reluctance Motors Based on Extended EMF Models Considering Magnetic Saturation With Online Parameter Identification". In: *IEEE Transactions on Industry Applications* 42.5 (Sept. 2006), pp. 1264–1274. ISSN: 1939-9367.

[49] T. Ince, S. Kiranyaz, L. Eren, and et. al. "Real-Time Motor Fault Detection by 1-D Convolutional Neural Networks". In: *IEEE Transactions on Industrial Electronics* 63.11 (2016), pp. 7067–7075.

[50] World Resources Institute. *Climate Watch Historical GHG Emissions*. https://www.climatewatchdata.org/ghg-emissions. Aug. 2021.

[51] Ivana Isakov, Vladimir Popović, Ivan Todorović, Stevan Grabić, and Darko Marčetić. "Application of Phase-Locked Loop in Sensorless SynRM Drives". In: *2018 International Symposium on Industrial Electronics (INDEL)*. 2018, pp. 1–4. DOI: 10.1109/INDEL.2018.8637641.

[52] I. Ishkova and O. Vitek. "Detection and classification of faults in induction motor by means of motor current signature analysis and stray flux monitoring". In: *Przeglad Elektrotechniczny* 1 (2016), pp. 168–172.

[53] C. Jiang, S. Li, and T. G. Habetler. "A review of condition monitoring of induction motors based on stray flux". In: *2017 IEEE Energy Conversion Congress and Exposition (ECCE)*. 2017, pp. 5424–5430. DOI: 10.1109/ECCE.2017.8096907.

[54] X. Jiang and Z. Ge. "Data Augmentation Classifier for Imbalanced Fault Classification". In: *IEEE Transactions on Automation Science and Engineering* (2020), pp. 1–12.

[55] R. Jigyasu, A. Sharma, L. Mathew, and S. Chatterji. "A Review of Condition Monitoring and Fault Diagnosis Methods for Induction Motor". In: *2018 Second International Conference on Intelligent Computing and Control Systems (ICICCS)*. IEEE, 2018, pp. 1713–1721.

[56] Simon J. Julier and Jeffrey K. Uhlmann. "New extension of the Kalman filter to nonlinear systems". In: *Signal Processing, Sensor Fusion, and Target Recognition VI*. Ed. by Ivan Kadar. Vol. 3068. International Society for Optics and Photonics. SPIE, 1997, pp. 182–193. URL: https://doi.org/10.1117/12.280797.

[57] I. Kao, W. Wang, Y. Lai, and et. al. "Analysis of Permanent Magnet Synchronous Motor Fault Diagnosis Based on Learning". In: *IEEE Transactions on Instrumentation and Measurement* 68.2 (2019), pp. 310–324.

[58] Kosuke Kato, Mutuwo Tomita, Shinji Doki, and Shigeru Okuma. "Position estimation for sensorless control of synchronous reluctance motor at low speed using disturbance observer". In: *2010 International Conference on Electrical Machines and Systems*. 2010, pp. 716–720.

[59] Nasser Kehtarnavaz. "CHAPTER 7 - Frequency Domain Processing". In: *Digital Signal Processing System Design (Second Edition)*. Ed. by Nasser Kehtarnavaz. Second Edition. Burlington: Academic Press, 2008, pp. 175–196. ISBN: 978-0-12-374490-6. DOI: https://doi.org/10.1016/B978-0-12-374490-6.00007-6. URL: https://www.sciencedirect.com/science/article/pii/B9780123744906000076.

[60] K. Ki-Chan, L. Seung-Bin, K. Dae-Hyun, and et. al. "The Shape Design of Permanent Magnet for Permanent Magnet Synchronous Motor Considering Partial Demagnetization". In: *IEEE Transactions on Magnetics* 42.10 (2006), pp. 3485–3487.

[61] S. Kumar et al. "A Comprehensive Review of Condition Based Prognostic Maintenance (CBPM) for Induction Motor". In: *IEEE Access* 7 (2019), pp. 90690–90704.

[62] B. Li, M. Chow, Y. Tipsuwan, and et. al. "Neural-Network-Based Motor Rolling Bearing Fault Diagnosis". In: *IEEE Transactions on Industrial Electronics* 47.5 (2000), pp. 1060–1069.

[63] Chengrui Li, Gaolin Wang, Guoqiang Zhang, Nannan Zhao, and Dianguo Xu. "Adaptive Pseudorandom High-Frequency Square-Wave Voltage Injection Based Sensorless Control for SynRM Drives". In: *IEEE Transactions on Power Electronics* 36.3 (2021), pp. 3200–3210. DOI: 10.1109/TPEL.2020.3015704.

[64] Chengrui Li, Gaolin Wang, Guoqiang Zhang, Nannan Zhao, and Dianguo Xu. "Review of parameter identification and sensorless control methods for synchronous reluctance machines". In: *Chinese Journal of Electrical Engineering* 6.2 (2020), pp. 7–18. DOI: 10.23919/CJEE.2020.000007.

[65] Haomin Li and Zheng Wang. "Sensorless Control for PMSM Drives Using the Cubature Kalman Filter based Speed and Flux Observer". In: *2018 IEEE International Conference on Electrical Systems for Aircraft, Railway, Ship Propulsion and Road Vehicles International Transportation Electrification Conference (ESARS-ITEC)*. 2018, pp. 1–6. DOI: 10.1109/ESARS-ITEC.2018.8607509.

[66] J. M. Lilly and S. C. Olhede. "Generalized Morse Wavelets as a Superfamily of Analytic Wavelets". In: *IEEE Transactions on Signal Processing* 60.11 (2012), pp. 6036–6041.

[67] I. Livieris and P. Pintelas. *A survey on algorithms for training artificial neural networks*. Tech. rep. University of Patras, Sept. 2008.

[68] D. Lopez-Perez and J. Antonino-Daviu. "Application of infrared thermography to fault detection in industrial induction motors: Case stories". In: *2016 XXII International Conference on Electrical Machines (ICEM)*. 2016, pp. 2172–2177. DOI: 10.1109/ICELMACH.2016.7732823.

[69] Toshiya Mabuchi et al. "Position sensorless control of synchronous reluctance motors at very low speeds region using high-frequency current control system". In: *2017 20th International Conference on Electrical Machines and Systems (ICEMS)*. 2017, pp. 1–6. DOI: 10.1109/ICEMS.2017.8055979.

[70] Stéphane Mallat. *A Wavelet Tour of Signal Processing, Third Edition: The Sparse Way*. 3rd. USA: Academic Press, Inc., 2008. ISBN: 0123743702.

[71] Virginia Manzolini and Silverio Bolognani. "On the Rotor Position Self-Sensing Capability of Reluctance and IPM Synchronous Motors". In: *IEEE Transactions on Industry Applications* 56.4 (July 2020), pp. 3755–3766. ISSN: 1939-9367. DOI: 10.1109/TIA.2020.2984406.

[72] D. Masters and C. Luschi. "Revisiting Small Batch Training for Deep Neural Networks". In: *CoRR* (2018). arXiv: 1804.07612 [cs.LG].

[73] Z. Meng, X. Guo, Z. Pan, D. Sun, and S. Liu. "Data Segmentation and Augmentation Methods Based on Raw Data Using Deep Neural Networks Approach for Rotating Machinery Fault Diagnosis". In: *IEEE Access* 7 (2019), pp. 79510–79522.

[74] A. Mikołajczyk and M. Grochowski. "Data augmentation for improving deep learning in image classification problem". In: *2018 International Interdisciplinary PhD Workshop (IIPhDW)*. IEEE, 2018, pp. 117–122.

[75] G. Mirzaeva and K. I. Saad. "Advanced Diagnosis of Rotor Faults and Eccentricity in Induction Motors Based on Internal Flux Measurement". In: *IEEE Transactions on Industry Applications* 54.3 (2018), pp. 2981–2991. DOI: 10.1109/TIA.2018.2805730.

[76] J J More. "Levenberg–Marquardt algorithm: implementation and theory". In: 1977. URL: https://www.osti.gov/biblio/7256021.

[77] R. Mukhopadhyay, P. S. Panigrahy, G Misra, and et. al. "Quasi 1D CNN-based Fault Diagnosis of Induction Motor Drives". In: *2018 5th International Conference on Electric Power and Energy Conversion Systems (EPECS)*. IEEE, 2018, pp. 1–5.

[78] Arrate Munoz, Raphael Ertle, and Michael Unser. "Continuous wavelet transform with arbitrary scales and O(N) complexity". In: *Signal Processing* 82.5 (2002), pp. 749–757.

[79] Zbynek Mynar, Pavel Vaclavek, and Petr Blaha. "Synchronous Reluctance Motor Parameter and State Estimation Using Extended Kalman Filter and Current Derivative Measurement". In: *IEEE Transactions on Industrial Electronics* 68.3 (2021), pp. 1972–1981. DOI: 10.1109/TIE.2020.2973897.

[80] S. Nandi and H. A. Toliyat. "Condition monitoring and fault diagnosis of electrical machines-a review". In: *Conference Record of the 1999 IEEE Industry Applications Conference. Thirty-Forth IAS Annual Meeting (Cat. No.99CH36370)*. 1999, pp. 197–204.

[81] S. Nandi, H.A. Toliyat, and X. Li. "Condition Monitoring and Fault Diagnosis of Electrical Motors—A Review". In: *IEEE Transactions on Energy Conversion* 20.4 (2005), pp. 719–729.

[82] Duc-Quan Nguyen, Luc Loron, and Kada Dakhouche. "High-speed sensorless control of a synchronous reluctance motor based on an Extended Kalman Filter". In: *2015 17th European Conference on Power Electronics and Applications (EPE'15 ECCE-Europe)*. 2015, pp. 1–10. DOI: 10.1109/EPE.2015.7309339.

[83] Saki Nohara, Mutuwo Tomita, Masaru Hasegawa, Shinji Doki, and Shinji Kato. "A new design method of full-order extended electromotive force observer for position sensorless control of IPMSM". In: *IECON 2013 - 39th Annual Conference of the IEEE Industrial Electronics Society*. 2013, pp. 2512–2517. DOI: 10.1109/IECON.2013.6699526.

[84] Ludovico Ortombina, Fabio Tinazzi, and Mauro Zigliotto. "Magnetic Modeling of Synchronous Reluctance and Internal Permanent Magnet Motors Using Radial Basis Function Networks". In: *IEEE Transactions on Industrial Electronics* 65.2 (2018), pp. 1140–1148. DOI: 10.1109/TIE.2017.2733502.

[85] P. A. Panagiotou, I. Arvanitakis, N. Lophitis, J. A. Antonino-Daviu, and K. N. Gyftakis. "Analysis of Stray Flux Spectral Components in Induction Machines under Rotor Bar Breakages at Various Locations". In: *2018 XIII International Conference on Electrical Machines (ICEM)*. 2018, pp. 2345–2351. DOI: 10.1109/ICELMACH.2018.8506929.

[86] J. Pando-Acedo, A. Rassõlkin, A. Lehikoinen, and et. al. "Hybrid FEA-Simulink Modelling of Permanent Magnet Assisted Synchronous Reluctance Motor with Unbalanced Magnet Flux". In: *2019 IEEE 12th International Symposium on Diagnostics for Electrical Machines, Power Electronics and Drives (SDEMPED)*. IEEE, 2019, pp. 174–180.

[87] D. Pasqualotto, A. Navarro Navarro, M. Zigliotto, and J. A. Antonino-Daviu. "Automatic Detection of Rotor Faults in Induction Motors by Convolutional Neural Networks applied to Stray Flux Signals". In: *2021 22nd IEEE International Conference on Industrial Technology (ICIT)*. Vol. 1. 2021, pp. 148–153. DOI: 10.1109/ICIT46573.2021.9453624.

[88] D. Pasqualotto, A. Navarro Navarro, M. Zigliotto, J.A Antonino-Daviu, and V. Biot-Monterde. "Fault Detection in Soft-started Induction Motors using Convolutional Neural Network Enhanced by Data Augmentation Techniques". In: *IECON 2021 The 47th Annual Conference of the IEEE Industrial Electronics Society*. IEEE, 2021, in Press.

[89] D. Pasqualotto and M. Zigliotto. "A comprehensive approach to convolutional neural networks-based condition monitoring of permanent magnet synchronous motor drives". In: *IET Electric Power Applications* 15.7 (2021), pp. 1–16.

[90] D. Pasqualotto and M. Zigliotto. "Increasing Feasibility of Neural Network Based Early Fault Detection in Induction Motor Drives". In: *IEEE Journal of Emerging and Selected Topics in Power Electronics* (2021, in Press).

[91] J. Pons-Llinares et al. "Advanced Induction Motor Rotor Fault Diagnosis Via Continuous and Discrete Time-Frequency Tools". In: *IEEE Transactions on Industrial Electronics* 62.3 (2015), pp. 1791–1802.

[92] Alexander Rakhlin, Ohad Shamir, and Karthik Sridharan. "Making Gradient Descent Optimal for Strongly Convex Stochastic Optimization". In: *Proceedings of the 29th International Conference on Machine Learning*. 2012, pp. 1571–1578.

[93] J. A. Ramirez-Nunez et al. "Evaluation of the Detectability of Electromechanical Faults in Induction Motors Via Transient Analysis of the Stray Flux". In: *IEEE Transactions on Industry Applications* 54.5 (2018), pp. 4324–4332. DOI: 10.1109/TIA.2018.2843371.

[94] R. Romary, R. Pusca, J. P. Lecointe, and J. F. Brudny. "Electrical machines fault diagnosis by stray flux analysis". In: *2013 IEEE Workshop on Electrical Machines Design, Control and Diagnosis (WEMDCD)*. 2013, pp. 247–256. DOI: 10.1109/WEMDCD.2013.6525184.

[95] J. A. Rosero, J. Cusido, A. Garcia, J. A. Ortega, and L. Romeral. "Broken Bearings and Eccentricity Fault Detection for a Permanent Magnet Synchronous Motor". In: *IECON 2006 - 32nd Annual Conference on IEEE Industrial Electronics*. IEEE, 2006, pp. 964–969.

[96] M.S.N. Said, M.E.H. Benbouzid, and A. Benchaib. "Detection of broken bars in induction motors using an extended Kalman filter for rotor resistance sensorless estimation". In: *IEEE Transactions on Energy Conversion* 15.1 (2000), pp. 66–70.

[97] S. B. Salem, M. Salah, W. Touti, K. Bacha, and A. Chaari. "Stray Flux analysis for monitoring eccentricity faults in induction motors: Experimental study". In: *2017 International Conference on Control, Automation and Diagnosis (ICCAD)*. 2017, pp. 292–297. DOI: 10.1109/CADIAG.2017.8075673.

[98] T. Senjyu, K. Kinjo, N. Urasaki, and K. Uezato. "High efficiency control of synchronous reluctance motors using extended Kalman filter". In: *IEEE Transactions on Industrial Electronics* 50.4 (Aug. 2003), pp. 726–732. ISSN: 1557-9948. DOI: 10.1109/TIE.2003.814998.

[99] C. Shorten and T. M. Khoshgoftaar. "A survey on Image Data Augmentation for Deep Learning". In: *Journal of Big Data* 6 (July 2019).

[100] A. Siddique, G. S. Yadava, and B. Singh. "A review of stator fault monitoring techniques of induction motors". In: *IEEE Transactions on Energy Conversion* 20.1 (2005), pp. 106–114.

[101] V. Simon-Sempere, M. Burgos-Payan, and J. Cerquides-Bueno. "Spatial Filtering: A Tool for Selective Harmonics Elimination in the Design of Permanent-Magnet Synchronous Motors". In: *IEEE Transactions on Magnetics* 48.6 (2012), pp. 2056–2067.

[102] Nitish Srivastava, Geoffrey Hinton, Alex Krizhevsky, Ilya Sutskever, and Ruslan Salakhutdinov. "Dropout: A Simple Way to Prevent Neural Networks from Overfitting". In: *Journal of Machine Learning Research* 15.56 (2014), pp. 1929–1958. URL: http://jmlr.org/papers/v15/srivastava14a.html.

[103] C.M. Thompson and L. Shure. *Image Processing Toolbox: For Use with MATLAB;[user's Guide]*. MathWorks, 1995.

[104] W. T. Thomson and I. Culbert. *Current Signature Analysis for Condition Monitoring of Cage Induction Motors: Industrial Application and Case Histories*. Wiley-IEEE Press, 2017. ISBN: 9781119175476.

[105] V. Tipsuwanporn, W. Piyarat, and C. Tarasantisuk. "Identification and control of brushless DC motors using on-line trained artificial neural networks". In: *Proceedings of the Power Conversion Conference-Osaka 2002 (Cat. No.02TH8579)*. Vol. 3. 2002, 1290–1294 vol.3. DOI: 10.1109/PCC.2002.998159.

[106] Pavel Vaclavek, Petr Blaha, and Ivo Herman. "AC Drive Observability Analysis". In: *IEEE Transactions on Industrial Electronics* 60.8 (2013), pp. 3047–3059. DOI: 10.1109/TIE.2012.2203775.

[107] Anantaram Varatharajan, Paolo Pescetto, and Gianmario Pellegrino. "Sensorless Synchronous Reluctance Motor Drives: A Full-Speed Scheme Using Finite-Control-Set MPC in a Projection Vector Framework". In: *IEEE Transactions on Industry Applications* 56.4 (July 2020), pp. 3809–3818. ISSN: 1939-9367. DOI: 10.1109/TIA.2020.2990834.

[108] B. Vaseghi, B. Nahid-Mobarakeh, N. Takorabet, and et. al. "Modeling of Non-Salient PM Synchronous Machines under Stator Winding Inter-turn Fault Condition: Dynamic Model - FEM Model". In: *2007 IEEE Vehicle Power and Propulsion Conference*. IEEE, 2007, pp. 635–640.

[109] Gaolin Wang, Maria Valla, and Jorge Solsona. "Position Sensorless Permanent Magnet Synchronous Machine Drives—A Review". In: *IEEE Transactions on Industrial Electronics* 67.7 (2020), pp. 5830–5842. DOI: 10.1109/TIE.2019.2955409.

[110] Z. Wang, J. Yang, H.Ye, and et.al. "A review of Permanent Magnet Synchronous Motor fault diagnosis". In: *2014 IEEE Conference and Expo Transportation Electrification Asia-Pacific (ITEC Asia-Pacific)*. IEEE, 2014, pp. 1–5.

[111] L. Wen, X. Li, L. Gao, and et. al. "A New Convolutional Neural Network-Based Data-Driven Fault Diagnosis Method". In: *IEEE Transactions on Industrial Electronics* 65.7 (2018), pp. 5990–5998.

[112] Q. Wen et al. "Time Series Data Augmentation for Deep Learning: A Survey". In: *ArXiv* abs/2002.12478 (Feb. 2020).

[113] M. Wlas, Z. Krzeminski, J. Guzinski, H. Abu-Rub, and H.A. Toliyat. "Artificial-neural-network-based sensorless nonlinear control of induction motors". In: *IEEE Transactions on Energy Conversion* 20.3 (2005), pp. 520–528. DOI: 10.1109/TEC.2005.847984.

[114] Dianguo Xu, Bo Wang, Guoqiang Zhang, Gaolin Wang, and Yong Yu. "A review of sensorless control methods for AC motor drives". In: *CES Transactions on Electrical Machines and Systems* 2.1 (2018), pp. 104–115. DOI: 10.23919/TEMS.2018.8326456.

[115] D. L. K. Yamins and J. J. DiCarlo. "Using goal-driven deep learning models to understand sensory cortex". In: *Nature Neuroscience* 19.3 (2016), pp. 356–365.

[116] I. Zamudio-Ramirez, J. A. Antonino-Daviu, R. A. Osornio-Rios, R. de J. Romero-Troncoso, and H. Razik. "Detection of Winding Asymmetries in Wound-Rotor Induction Motors via Transient Analysis of the External Magnetic Field". In: *IEEE Transactions on Industrial Electronics* 67.6 (2020), pp. 5050–5059. DOI: 10.1109/TIE.2019.2931274.

[117] Jafar Zarei, Elham Kowsari, and Roozbeh Razavi-Far. "Induction Motors Fault Detection Using Square-Root Transformed Cubature Quadrature Kalman Filter". In: *IEEE Transactions on Energy Conversion* 34.2 (2019), pp. 870–877.

[118] P. Zhang, Y. Du, T. G. Habetler, and B. Lu. "A Survey of Condition Monitoring and Protection Methods for Medium-Voltage Induction Motors". In: *IEEE Transactions on Industry Applications* 47.1 (2011), pp. 34–46.

[119] Tanja Zwerger and Paolo Mercorelli. "A Dual Kalman Filter to Identify Parameters of a Permanent Magnet Synchronous Motor". In: *2020 24th International Conference on System Theory, Control and Computing (ICSTCC)*. 2020, pp. 619–623. DOI: 10.1109/ICSTCC50638.2020.9259686.